

DIRECT INTEGRATION OF DIELECTROPHORESIS, PNEUMATIC PUMPING, AND REVERSIBLY  
BONDED POLYMER MOULDS FOR MEMS BASED LAB-ON-CHIP APPLICATIONS

by

Hunter King

Submitted in partial fulfilment of the requirements  
for the degree of Master of Applied Science

at

Dalhousie University  
Halifax, Nova Scotia  
April 2016

© Copyright by Hunter King, 2016

# TABLE OF CONTENTS

LIST OF TABLES.....	v
LIST OF FIGURES.....	vi
ABSTRACT.....	x
ACKNOWLEDGMENT.....	xi
CHAPTER 1: INTRODUCTION.....	1
1.1. PROBLEM.....	1
1.2. BACKGROUND .....	2
1.3. SCOPE .....	3
1.4. CONTRIBUTIONS.....	4
CHAPTER 2: MEMS FOR CELL TESTING .....	6
2.1. MEMS SURFACE MICROMACHINING .....	6
2.2. MEMS MOTORS/ACTUATORS .....	7
2.3. BIOMEMS BACKGROUND.....	9
2.4. CELL SQUEEZER .....	10
2.5. OPTICAL MEASUREMENTS .....	13
2.6. PROBLEM BACKGROUND .....	18
CHAPTER 3: DEP .....	23
3.1. INTRODUCTION .....	23

3.2.	DEP ELECTRODE GEOMETRY .....	26
3.3.	DEP SIMULATION .....	31
3.3.1.	PROBLEM DEFINITION AND BOUNDARY CONDITIONS .....	31
3.3.2.	SOLUTION.....	34
3.4.	DEP PROBLEMS .....	43
CHAPTER 4: MOULDS.....		44
4.1.	MOULD INTRODUCTION .....	44
4.2.	MOULD BACKGROUND.....	45
4.3.	PRODUCTION.....	47
CHAPTER 5: MOULD INTEGRATION .....		59
5.1.	PRE-PLACEMENT STEPS.....	59
5.2.	PLACEMENT METHOD .....	59
5.3.	FILLING AND REMOVAL.....	65
5.4.	MOULD REDESIGN.....	70
CHAPTER 6: RESULTS.....		75
6.1.	CHEVRON ACTUATORS IN MOULDS.....	75
6.1.1.	OPEN (AIR/WATER) .....	75
6.1.2.	CLOSED (AIR/WATER).....	76
6.2.	DEP RESULTS .....	79

6.2.1. OPEN.....	79
6.2.2. CLOSED.....	81
6.3. PNEUMATIC PUMPING/SPHERE PLACEMENT.....	85
CHAPTER 7: CONCLUSIONS.....	89
7.1. CONTRIBUTION .....	89
7.2. FUTURE WORK .....	90
APPENDIX.....	100
1. MATLAB SIMULATION .....	100

## LIST OF TABLES

Table 1: Mould placement accuracy results .....	63
---	----

# LIST OF FIGURES

Figure 1: PolyMUMPS layers.....	6
Figure 2: Chevron thermal actuator: current running through the bent arms left to right causes the center to buckle downwards. ....	8
Figure 3: Mechanical spring with periodic optical comb structures in the center.....	11
Figure 4: Example of MEMS cell stiffness testing device: chevron at top, gap, spring at bottom .....	12
Figure 5: Periodic structure for displacement measurement with optical regions of interest (ROI) shown in red.....	14
Figure 6: Y-averaged pixel intensity of region of interest from Figure 5.....	15
Figure 7: FFT of y-averaged pixel intensity for Yamahata method, fundamental spatial frequency shown with arrow.....	15
Figure 8: Experimental setup for FFT optical displacement measurements.....	17
Figure 9: 3 DOF Micromanipulator setup .....	18
Figure 10: 3DOF system with pipette installed.....	19
Figure 11: Micromanipulator pump system .....	19
Figure 12: PolyMUMPs chip submerged in distilled water for cell testing .....	20
Figure 13: Pipette grabbing yeast cell (cell is 6.5 $\mu\text{m}$ ) .....	21
Figure 14: Picture of pipette placing a cell into a squeezing device.....	21
Figure 15: Diagram of DEP force on spherical particle .....	24
Figure 16: Side profile of 2-phase electrode geometry .....	27

Figure 17: 200 $\mu$ m wide 2-phase DEP array on MM1 .....	28
Figure 18: Close up of 2 phase electrode array with phases labelled .....	29
Figure 19: DEP track reduction & cell squeezer (MM1) wide section = 200 $\mu$ m width, narrow = 20 $\mu$ m width.....	30
Figure 20: Electrode geometry with boundary conditions shown .....	34
Figure 21: Simulation of electrical potential around arrays (Top real, bottom imaginary components).....	36
Figure 22: Clausius-Mossotti Factor vs Frequency for ethanol .....	38
Figure 23: Clausius-Mossotti factor for 0.1M sorbitol at high frequencies.....	39
Figure 24: Simulation of TOP: dielectric ( $F_y$ ) & BOTTOM: travelling wave ( $F_x$ ) dielectric force vectors .....	41
Figure 25: Close up of $F_x$ travelling wave dielectrophoretic forces from electrode edge	42
Figure 26: Simulated DEP particle velocity vs applied voltage .....	43
Figure 27: PolyMUMPs chip covered in adhered dried cells .....	45
Figure 28: Image of Kraton beads melting on 2" silicon wafer .....	48
Figure 29: Melted Kraton beads pressed.....	48
Figure 30: Kraton puck smooth from compression .....	49
Figure 31: Kraton puck re-melting .....	50
Figure 32: Kraton puck with negative .....	51
Figure 33: Kraton puck with negative being pressed .....	51
Figure 34: Mould separated from the negative note 0.5 mm diameter ports.....	52
Figure 35: Mould cut from puck with channel holes punched.....	53

Figure 36: Close up of microfluidic channel in mould compared to design, circular ports are 1 mm diameter .....	54
Figure 37: Close up of actuator and backspring area compared to design .....	55
Figure 38: SEM image of mould degradation .....	57
Figure 39: Close up of mould degradation .....	58
Figure 40: Mould placement system .....	60
Figure 41: Mould with cruciform placement markers shown .....	61
Figure 42: MM1 chip with placement marker labelled .....	62
Figure 43: Properly aligned placement markers.....	62
Figure 44: SEM stub covered in Teflon (stub is 13 mm diameter) .....	63
Figure 45: Placed mould top: pre-pressing bottom: post-pressing.....	64
Figure 46: Close up of pumping setup .....	65
Figure 47: Close up of microfluidic channel filling (5x5 mm die).....	66
Figure 48: Process of microfluidic channel filling – suction on the left, note the meniscus moving from right to left .....	67
Figure 49: Pneumatic pumping setup with GenieTouch™ syringe pump.....	68
Figure 50: Mould leaking (working fluid ethanol) .....	69
Figure 51: Ethanol placed on mould to remove from suction tip .....	70
Figure 52: Old Mould Design (Top), New Mould Design (Bottom).....	72
Figure 53: Mould redesign: 1) original design, 2) new design, 3) new design with ports in actuator and back spring area .....	73
Figure 54: Displacement of chevron thermal actuator in air - no mould.....	75

Figure 55: Displacement of chevron thermal actuator in water - no mould.....	76
Figure 56: Displacement vs Voltage thermal actuator in air – under mould .....	77
Figure 57: Displacement vs Voltage thermal actuator in water – under mould .....	77
Figure 58: Displacement vs Voltage <sup>2</sup> for chevron actuator in air/water open & closed..	78
Figure 59: DEP velocity vs voltage for wide section of track on MM1 – no mould.....	80
Figure 60: Open DEP velocities - experimental vs simulated .....	80
Figure 61: DEP velocity vs voltage for wide section of track on MM1 (closed) .....	81
Figure 62: Comparison of 6 µm polystyrene sphere DEP velocities no mould vs mould.	82
Figure 63: Diagram of sphere motion in open MM1 track.....	83
Figure 64: 6 µm particles trapped using DEP.....	84
Figure 65: Superimposition of 4 images of 6 µm spheres being moved towards the actuator gripper. Moving from right to left, spheres circled for clarity .....	86
Figure 66: Image enhancement of time steps of 6 µm polystyrene sphere pneumatically placed into actuator jaws. Moving from right to left, spheres circled for clarity. ....	87
Figure 67: Close up of jaw placed sphere a1 = 10.6 µm, a2 = 3.4 µm .....	88

## ABSTRACT

Cell testing based on lab-on-chip technology using MEMS devices is a new area of interest for biomedical research, however currently the testing is limited in the sample size which is due to low throughput methods applied for manipulating cell cultures. Here a novel approach is presented to form a contained microfluidic environment on a PolyMUMPs technology based MEMS chip. Within the microfluidic environment, pneumatic and dielectrophoretic pumping technologies are used to manipulate particles for use in the subsequent cell testing applications. These cell testing/squeezing devices would test the mechanical properties of cells for use in biomedical diagnostics. Kraton polymer moulds are placed onto MEMS chips with a placement accuracy of  $\pm 4.0 \mu\text{m}$ . A working fluid (Sorbitol) is then pumped into the microfluidic channels in the mould by use of a Lucca Technologies GenieTouch™ Syringe Pump. Polystyrene beads are then used to test pneumatic and dielectrophoretic pumping. A controlled pneumatic pumping with velocities up to  $30 \mu\text{m/s}$  was achieved. Using travelling wave dielectrophoresis, bi-directional particle manipulation was achieved with velocities up to  $19 \mu\text{m/s}$  in the wide channels of the mould, however the particle motion was limited to the wide channels only. The  $6 \mu\text{m}$  polystyrene beads were accurately manipulated into the jaws of a mechanical cell squeezing device using pneumatic pumping within the mould channels showing future potential for increasing throughput of lab-on-chip MEMS cell testing devices.

## ACKNOWLEDGMENT

I would like to express my sincere gratitude to my supervisor Dr. Ted Hubbard for his advice, support, and expertise throughout the course of the work. Especially in regards to his aid and advice in writing and presentation. In addition to Dr. Hubbard I would also like to thank the other members of my thesis committee; Dr. Marek Kujath, and Dr. Serguei Iakovlev. Their advice and support on the direction of this work was greatly appreciated.

Secondly a very special thanks to Dr. Stephan Warnat. His advice and guidance throughout the course of this work was instrumental to its success. Without his daily support and direction this work would not be where it is today.

Thirdly I would like to thank my family and friends for their support throughout this work. A special thanks to my fiancé Laura for her support especially during the writing of this thesis.

Finally I would like to recognize that this work would not have been possible without the financial support from NSERC, the technical support from CMC Microsystems, and the administrative support from Dalhousie University, and more specifically the Mechanical Engineering Department and the Faculty of Graduate Studies.

# CHAPTER 1: INTRODUCTION

This thesis investigated the use of reversibly bonded polymer moulds, dielectrophoresis, and PolyMUMPS based thermal actuators for lab-on-chip MEMS. Specifically, the implementation of dielectrophoretic and pneumatic pumping for high throughput microparticle manipulation in microfluidic channels which were produced by the polymer moulds. An accurate placement of microparticles within microfluidic channels by the use of pneumatic pumping is also explored.

## 1.1. PROBLEM

The Dalhousie MEMS lab has been invested in the mechanical testing of yeast cells for the past few years. The mechanical properties of cells are important characteristics in cell health measurement in addition to potential application to disease diagnostics [1]. Lam et al. [2] showed that the stiffness of leukemia cells increased by nearly a factor of two when exposed to typical chemotherapy treatments. Suresh et al. [3] showed that the shear modulus of red blood cells increased by a factor of  $\sim 10$  during the developmental stages of the malaria parasite. Schwartz et al. have shown that PolyMUMPs based MEMS thermal actuators are a suitable technology for testing the stiffness of cells [4]. One limit of this technique however is the small throughput of the method. Schwartz et al. used a micropipette that was manipulated via a 3-DOF Zaber micromanipulator. This placement process, used at the Dalhousie MEMS lab, starts with a drop of cultured cells being placed onto the chip in question. This cell culture is then

allowed to partially dry such that the cells adhere to the substrate. Once the cells have partially adhered to the substrate the entire chip is flooded with the working fluid of the cells. Next, a micropipette is placed onto the chip and moved into position next to a cell of interest. This cell is then carefully aspirated onto the tip of the pipette. Once the cell is firmly attached to the pipette, it is moved to the testing devices. The cell is then released from the pipette via a small amount of positive pressure, and the pipette is then removed from the medium for the duration of the cell stiffness trial. Once the trial is complete the user returns the pipette to the medium, aspirates the cell from the testing device and then repeats the process of grabbing and releasing another cell for testing. This process is tedious, and the success rate is not only dependent on the skill of the individual operating the setup, but also on the properties of the cells in question as some are much easier to manipulate than others. The method described by Schwartz et al. also requires that the entire surface of the PolyMUMPs chip be submerged in the working fluid (typically distilled water). This can cause damage, or interfere with other structures on the chip. In addition cross-contamination can occur when testing biological samples on a chip.

## 1.2. BACKGROUND

Microelectromechanical Systems (MEMS) are used in many industries, and have many uses. They also have advantages over macro scale devices as they can be inexpensive to produce [5], typically require little power and have fast response times due to their size. Some example of MEMS devices are: accelerometers [6], gyroscopes [7], pressure

sensors [8], flow sensors [9], temperature sensors [10], micro-actuators [11], and recently micro-squeezing devices for use in biomedical applications [4] [12].

MEMS based dielectrophoretic cell separation and manipulation has also been an area of interest. For example Gascoyne et al. [13] showed that cancer cells can be reliably separated from blood. Wang et al. [14] also showed the possibility of linear motion, levitation, and circulation of cells using a form of dielectrophoresis known as travelling-wave dielectrophoresis. Travelling wave dielectrophoresis is discussed in detail in chapter 3. The integration of this technology with existing mechanical cell testing devices could be of use as it allows for particle separation in addition to controlled movement to the testing devices.

In addition to the use of dielectrophoresis, microfluidic environments are of interest in the field of lab-on-chip MEMS technology. Currently the standard practice for producing moulded microfluidic environments in a laboratory setting is to use a thermoplastic elastomer: PDMS (polydimethylsiloxane) [15]. Wasay et al. [15] have designed a new method for producing microfluidic environments suitable for use with PolyMUMPs based MEMS chips. The use of these microfluidic environments is of interest as it allows for the segregation of wet and dry sections of microfluidics, in addition to the potential for microfluidic pumping.

### 1.3. SCOPE

This paper presents the use of reversibly bonded polymer gecko adhesives in conjunction with pneumatic and dielectrophoretic pumping for MEMS lab-on-chip

applications. The method of adhesive mould production is discussed, along with challenges associated with production and design. Pneumatic pumping as a method of mould channel filling, controlled particle pumping, and controlled particle placement is explored. Dielectrophoresis as a method of controlled bi-directional particle manipulation is also quantified in Sorbitol, and other working fluids are also discussed.

Mould material selection is not explored, nor is the design of the gecko features used for adhesion in the moulds. Wasay et al. [15] describe the gecko gaskets and production in detail. AC-electroosmosis [16] as a method of microparticle manipulation using MEMS electrode arrays will not be explored, and pneumatic pumping is limited to pumping via syringe pump.

## 1.4. CONTRIBUTIONS

This work combines both novel and well researched topics into a single goal of increasing the throughput of lab-on-chip style MEMS cell testing. Gecko inspired reversible bonded adhesive moulds were developed by Dr. Sameoto and Abdul Wasay at the University of Alberta [15], however the implementation with PolyMUMPs based MEMS devices is a novel application. Although the pneumatic pumping of fluids using PDMS based microfluidic channels has been recently tested [17], the use of pneumatic pumping with the gecko inspired reversibly bonded polymer moulds has not been previously explored. Dielectrophoresis as a method for particle separation, movement, and trapping [18] has been explored. However the use of dielectrophoresis for particle manipulation in polymer microchannels on MEMS devices has not been researched

prior. Therefore this paper provides novel research relating to the advancement of high-throughput MEMS based lab-on-chip cell testing technology.

## CHAPTER 2: MEMS FOR CELL TESTING

### 2.1. MEMS SURFACE MICROMACHINING

There are many different technologies for producing MEMS. Some common methods of producing MEMS devices are: bulk micromachining, surface micromachining, and high aspect ratio (HAR) silicon micromachining [19]. One such method of surface micromachining is known as PolyMUMPs [20]. PolyMUMPs uses 8 mask levels consisting of a base layer of silicon, a nitride substrate, 3 polysilicon layers, 2 oxide layers, and 1 metal layer (Figure 1). PolyMUMPs is advantageous due to being inexpensive, and having a high resolution.

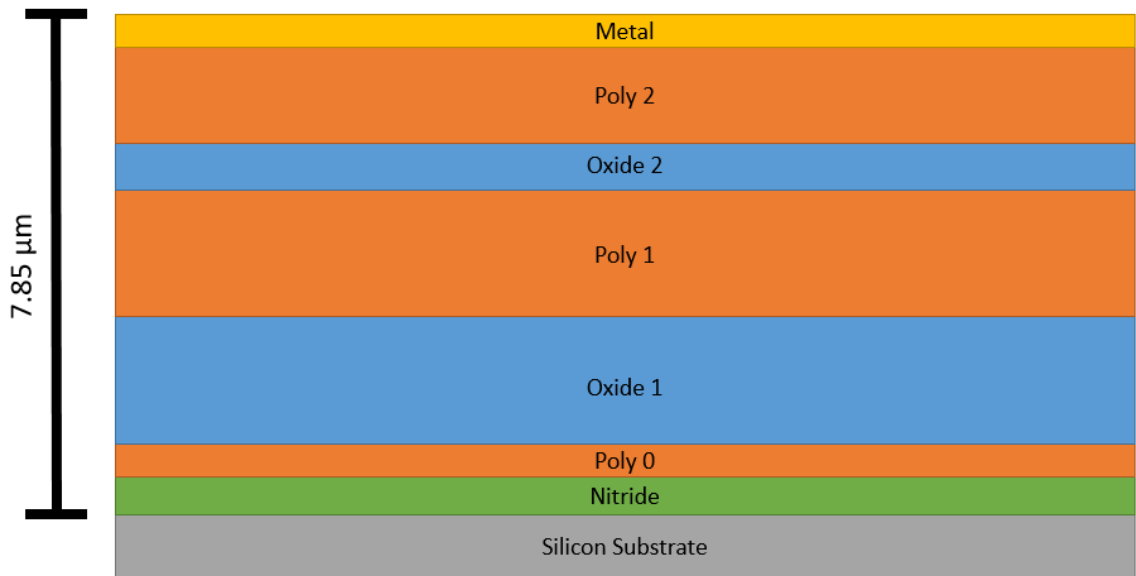


Figure 1: PolyMUMPS layers

PolyMUMPs devices however have some limitations due to the nature of their fabrication. PolyMUMPs devices have a minimum feature size of 2 μm [20]. The

PolyMUMPs fabrication process also does not allow for enclosed open spaces such as dome style components, or long channels (even if the ends of the channel are open). This is due to the nature of the fabrication process. As layers are patterned with a photo-resist and then etched, the under-etching process cannot be completed in a completely enclosed feature. In addition the under-etch design rules state that etch holes must be placed in any covered area that is 30  $\mu\text{m}$  or more away from another open space [20]. This limits any possible microfluidic channels to a maximum length of 30  $\mu\text{m}$ : furthermore any such short channels would be shallow ( $< 3 \mu\text{m}$ , which is smaller than many cells).

## 2.2. MEMS MOTORS/ACTUATORS

PolyMUMPs is a suitable fabrication technology for MEMS motors and actuators. There are multiple common forms of MEMS motors and actuators. One of the most common forms is the Chevron thermal actuator [11] (Figure 2). It has been thoroughly studied for its reliability and performance in both air and aqueous media [21]. The Chevron thermal actuator (like other MEMS thermal actuators) works on the property of Joule heating and the thermal expansion of materials, specifically Polysilicon. As the arms of the chevron actuator heat up they expand laterally. Due to the angle of the beams the transverse expansion is magnified  $\sim 10$  times. The magnitude of the expansion is proportional to the energy applied to the system ( $\alpha V^2$ ). The expansion is also proportional to the thermal conductance of the medium in which the actuator is placed [21]. Barazani et al. [22] showed that the performance of a thermal actuator when in

water was ~7% of the displacement of the same actuator in air. Barazani showed that the relative

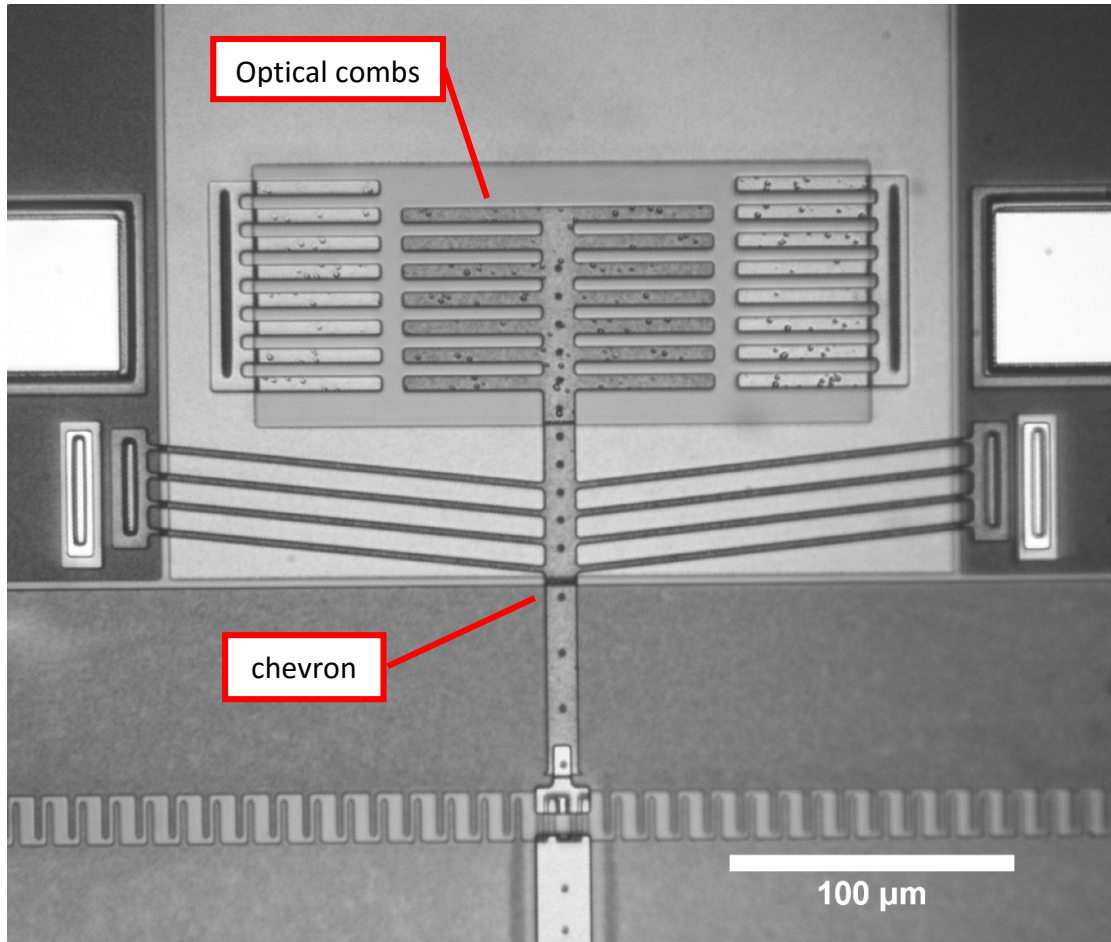


Figure 2: Chevron thermal actuator: current running through the bent arms left to right causes the center to buckle downwards.

conductance of air vs water was 5%, and that the conductivity of the medium has the largest effect on the performance of the actuator. Barazani also showed that the temperature of a chevron thermal actuator is unlikely to affect any biological cell when used as a device for the mechanical testing of cell properties. He showed that the temperature increase at the point which makes contact with the cell to be less than

0.5°C higher than ambient water temperature when 6 Vpp is applied to the actuator [22].

### 2.3. BIOMEMS BACKGROUND

Although MEMS devices are commonly used in areas such as the automotive sensing industry and consumer accelerometers/gyroscopes, MEMS devices have recently become an area of interest in regards to biological and biomedical uses. BioMEMS devices have many potential uses, some of these are in diagnostics [23] [24] [25] [26], therapy and treatment of disease [27] [28], and cell biology studies [4] [29]. MEMS devices pose a major benefit in these fields due to their size which allows for sensitive measurement.

Biomedical diagnostic devices present a new method for detecting many different pathogens, chemicals, and genetic conditions such as: Hepatitis B, HIV, Alzheimer's, glucose and cholesterol measurement, and gastrointestinal disease [30]. These devices measure changes using multiple methods. Ferreira et al. [26] designed a chip sized MEMS testing device which uses spectroscopic techniques to measure changes in gastrointestinal tissue properties. Similar technology is utilized by products such as Given Imagings PillCam® which provides a miniaturized camera in pill form for colon imaging. Zhang et al. [31] developed an electrochemical biosensor which utilized the covalent immobilization of the 21-mer single-stranded DNA which is related to the HBV gene by use of a modified glassy carbon electrode.

Another potential use for BioMEMS devices is in the closely related field of disease treatment and therapy. Cong et al. [27] developed an implantable blood pressure monitoring device into a laboratory rat for real time measurement. Tsai et al. [28] designed a device which consists of a smart MEMS based drug release valve connected to a moulded PDMS drug reservoir for potential future in vivo smart drug deployment. The smart drug delivery device measures glucose levels in the surrounding medium and can then deliver up to 100  $\mu\text{L}$  of electroactive insulin.

In addition to in vivo technologies, in vitro technologies for the BioMEMS industry are also being developed. Suresh et al. [3] showed that the stiffness of red blood cells increases by a factor of  $\sim 10\text{x}$  when infected with the malaria parasite. Warnat et al. [32] showed that PolyMUMPs based MEMS actuators provide a reliable method for testing cells in aqueous media. This paper focuses on increasing the throughput of the MEMS based chevron thermal actuator as a method of mechanical cell testing, which has been used extensively by the Dalhousie MEMS lab over the past years [22] [32] [33] [34].

## 2.4. CELL SQUEEZER

The cell squeezing device developed at Dalhousie is composed of 2 parts. The first part is a chevron thermal actuator with a periodic comb structure attached to the back (see Figure 2), as well as a periodic comb structure attached to the substrate (these comb structures are used for displacement measurement and will be covered in detail in the following section). The second part is a mechanical spring whose stiffness is based on simple cantilever beam theory and is known. This spring (Figure 3) also has a periodic

structure similar to that found on the actuator device. The two devices are then placed such that there is a gap between the tip of the actuator tip (called the gripper from this point forward) and the back spring (Figure 4). This gap is usually slightly larger than that of the cells to be tested. The gripping device used in this thesis has a gap of  $10\ \mu\text{m}$  between the actuator and the back spring.

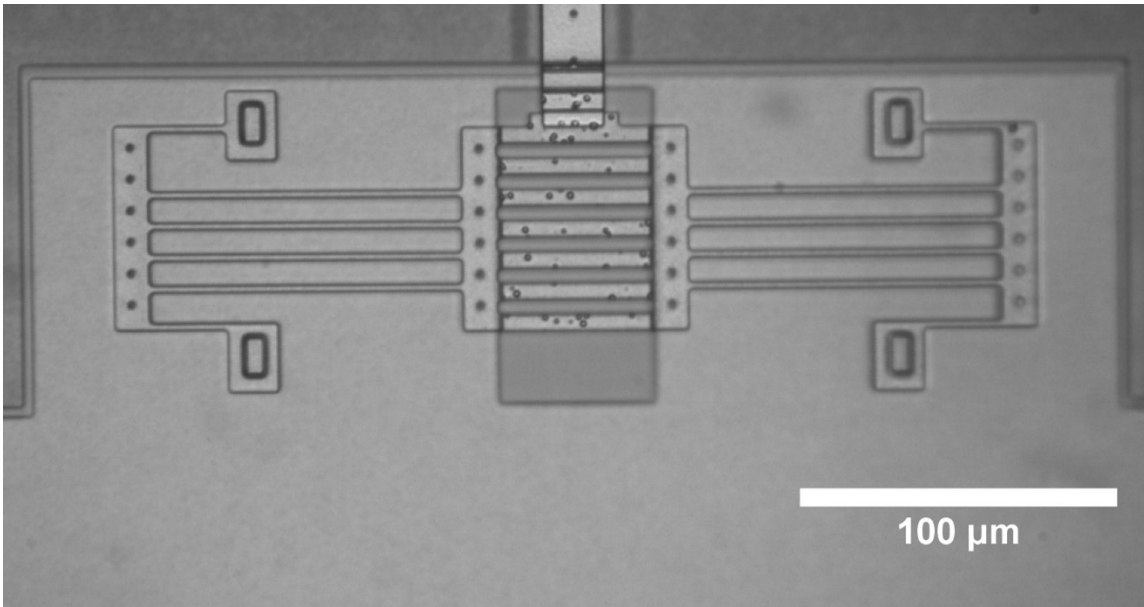


Figure 3: Mechanical spring with periodic optical comb structures in the center.

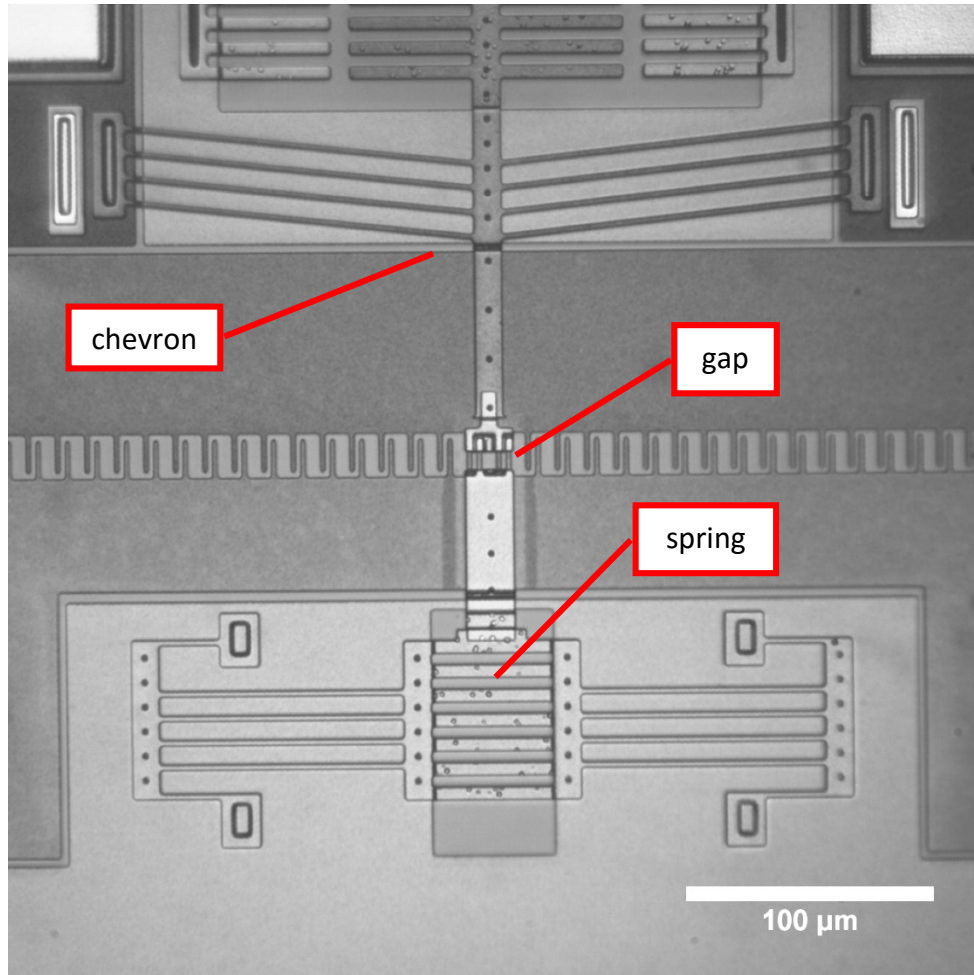


Figure 4: Example of MEMS cell stiffness testing device: chevron at top, gap, spring at bottom

By measuring the difference between the input displacement from the actuator and the output displacement (displacement of the back spring of known stiffness) the stiffness of the cell can be calculated. However, the stiffness of the back spring must be similar to that of the cell, otherwise errors are introduced. Cell stiffness measurement error can also be observed from issues with displacement measurement resolution and accuracy.

In order to accurately measure the displacement of both the input and output structures an optical method known as the Yamahata [35] method is used.

## 2.5. OPTICAL MEASUREMENTS

The Yamahata method uses periodic structures that are purposefully placed on the actuator, back spring, and substrate. From here a series of images (depicting the displacement of the actuator at different applied voltages) are cropped to a region-of-interest (ROI) (see Figure 5). The 2D-ROI is column averaged to produce a 1-D pixel intensity profile (see Figure 6) which is then analyzed using a Fast-Fourier-Transform (FFT) (see Figure 7).

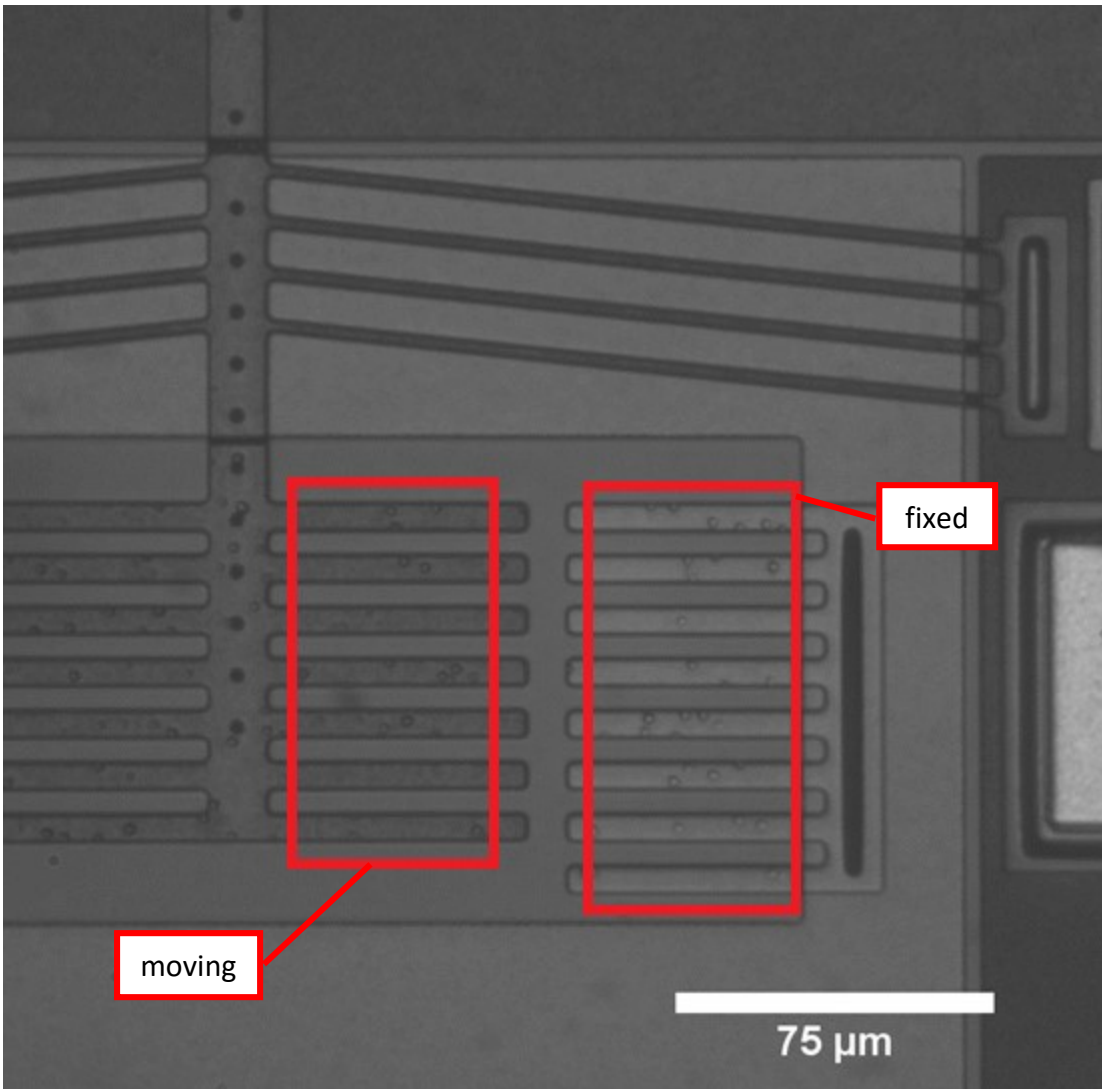


Figure 5: Periodic structure for displacement measurement with optical regions of interest (ROI) shown in red

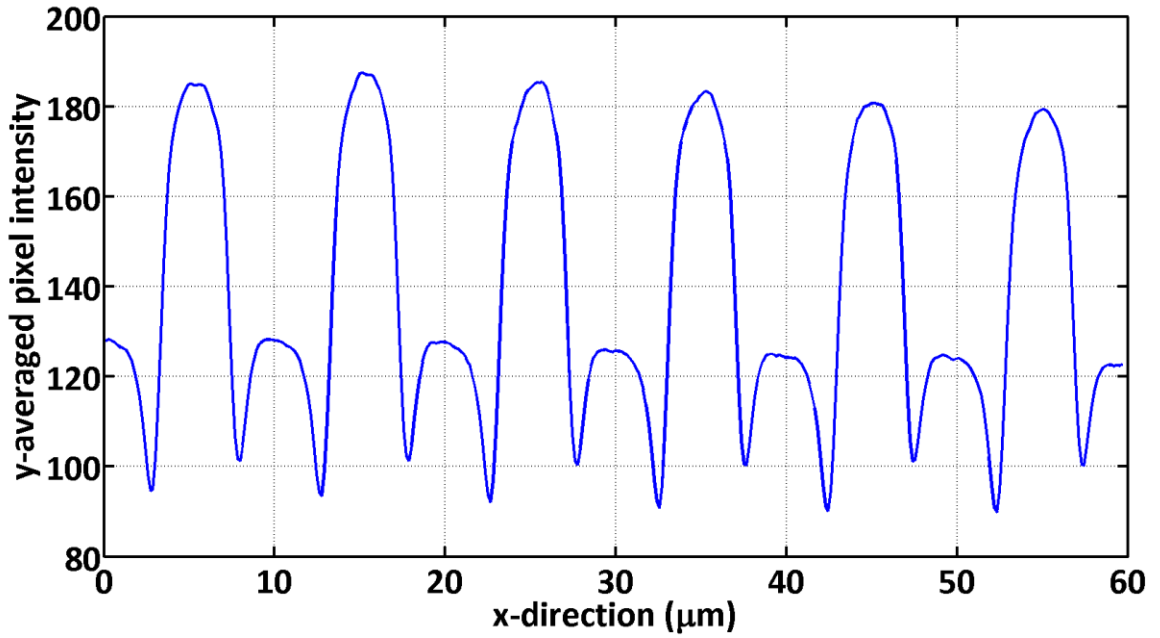


Figure 6: Y-averaged pixel intensity of region of interest from Figure 5

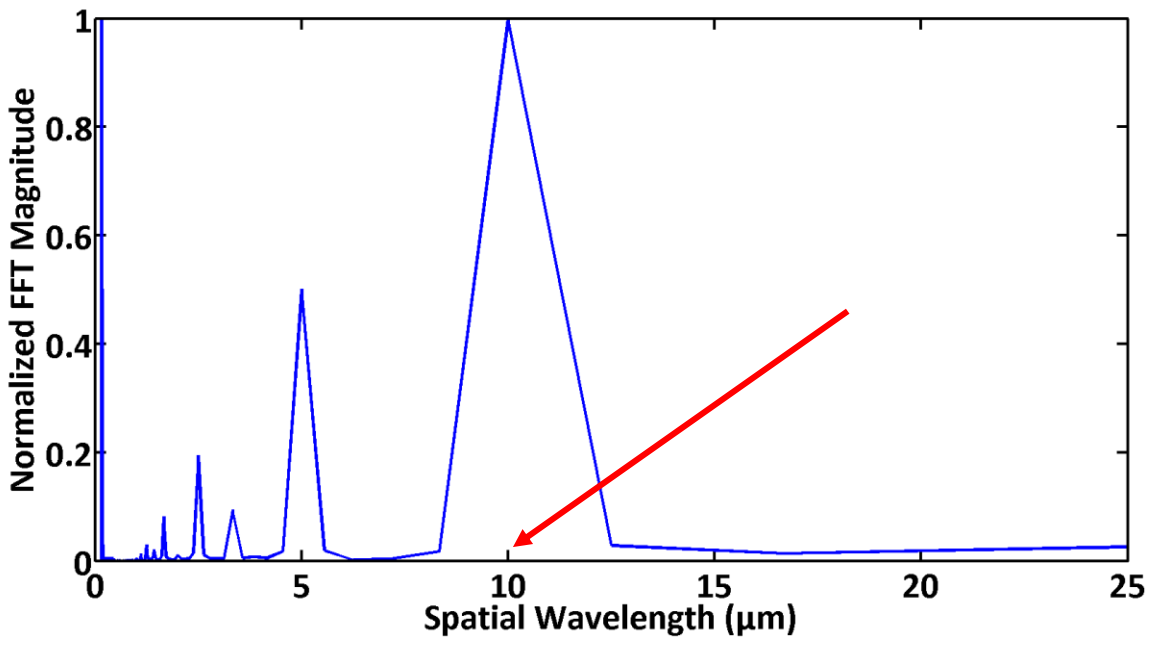


Figure 7: FFT of y-averaged pixel intensity for Yamahata method, fundamental spatial frequency shown with arrow

The fundamental frequency (as labeled in Figure 7) corresponds to the spatial periodic frequency of the periodic structures mentioned on page **Error! Bookmark not defined.**

The periodic structures consist of a beam of Polysilicon which is 5  $\mu\text{m}$  in width followed by a gap of 5  $\mu\text{m}$  for a wavelength of 10  $\mu\text{m}$ . These structures are repeated to form a precise spatially periodic structure. This structure is important as it is the basis of the method of displacement measurement. The phase of the fundamental frequency is then measured from image to image. This phase shift between images is then converted back to the spatial domain to measure the displacement of the actuator, as well as the displacement of the back spring. In order to reduce measurement noise; a fixed reference structure attached to the substrate is used. The displacement of the reference structure is subtracted from the displacement of the actuator and back spring in order to isolate motion measurement from most environmental noise. Figure 8 shows the experimental setup for the FFT optical displacement measurement technique. Warnat et al [33] showed methods of improving the resolution of the Yamahata [35] method by using color image processing. The results showed a displacement measurement resolution of  $\pm 10$  nm in water. The motion of chevron thermal actuators follows a curve where displacement is proportional to the square of the applied voltage to the actuator. However the performance of chevron thermal actuators is affected significantly by the medium in which they are run.

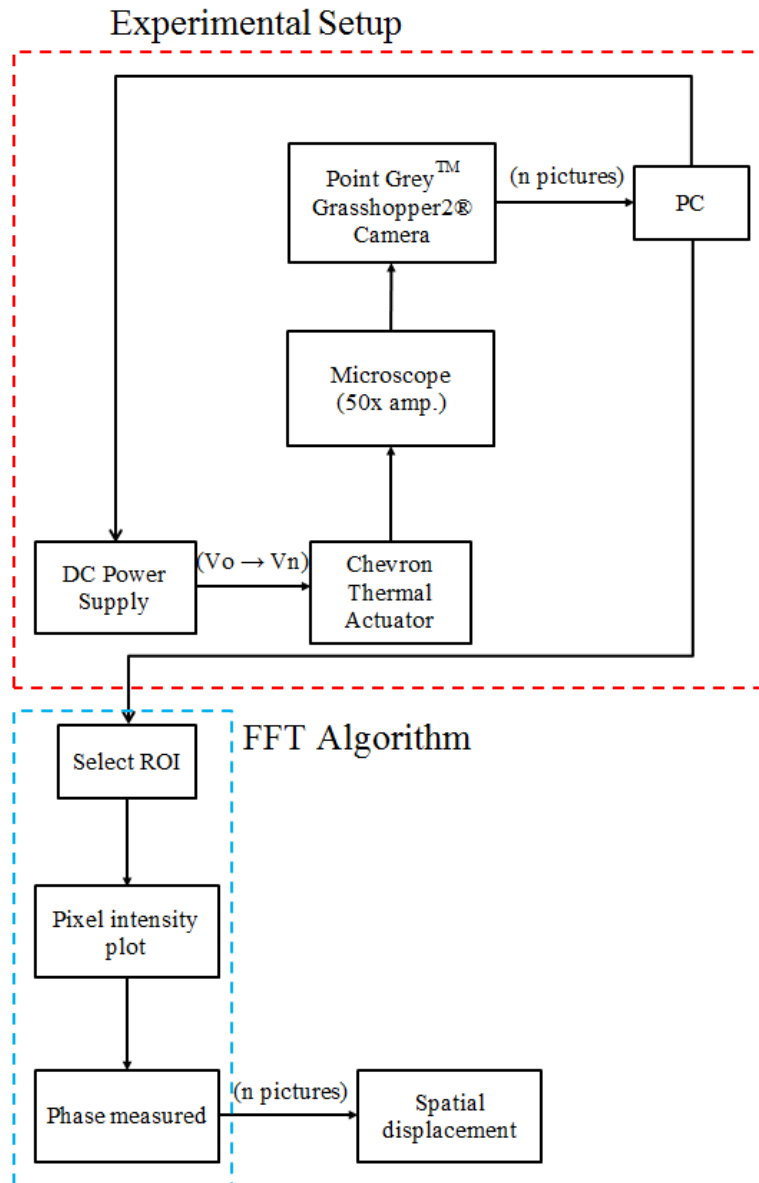


Figure 8: Experimental setup for FFT optical displacement measurements

## 2.6. PROBLEM BACKGROUND

Currently the method being used by the MEMS lab at Dalhousie for controlled movement and placement of cells is a manual method of placement using a micropipette and a 3 degree of freedom micromanipulator (Figure 9 – 11 show the physical setup).



Figure 9: 3 DOF Micromanipulator setup

The controller first places a micropipette into the hydraulic system, then primes the system by pushing a small amount of water through the micropipette. Next a drop of cells is placed onto the dry chip. The drop of cells is then allowed to partially dry so as to allow the cells to partially adhere to the substrate. From here the entire chip is

submerged in the working fluid (typically distilled water), shown in Figure 12.



Figure 10: 3DOF system with pipette installed

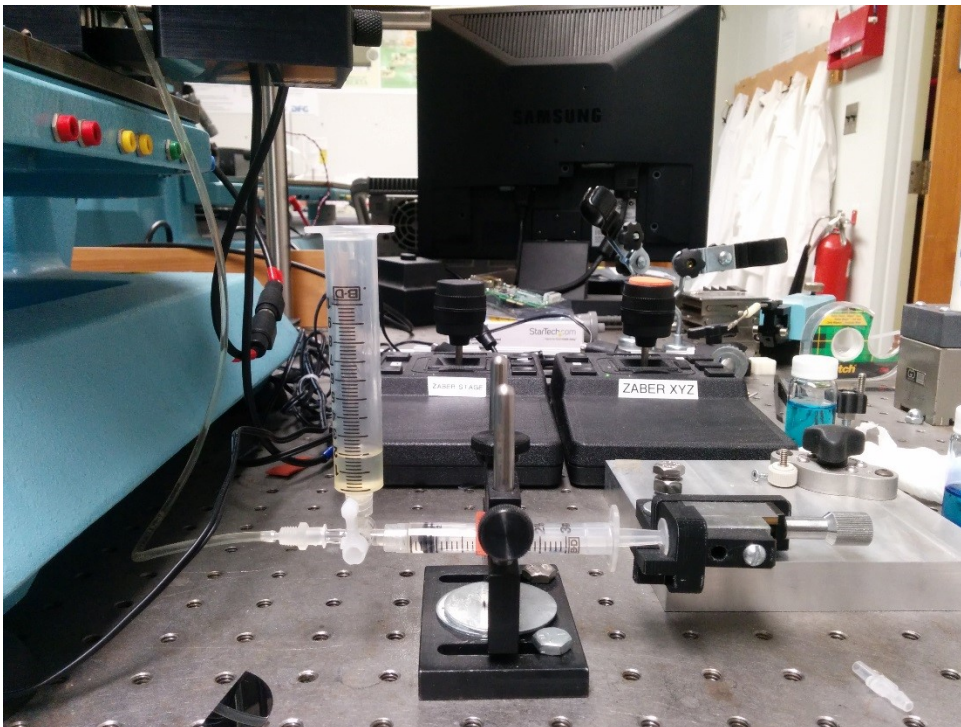


Figure 11: Micromanipulator pump system

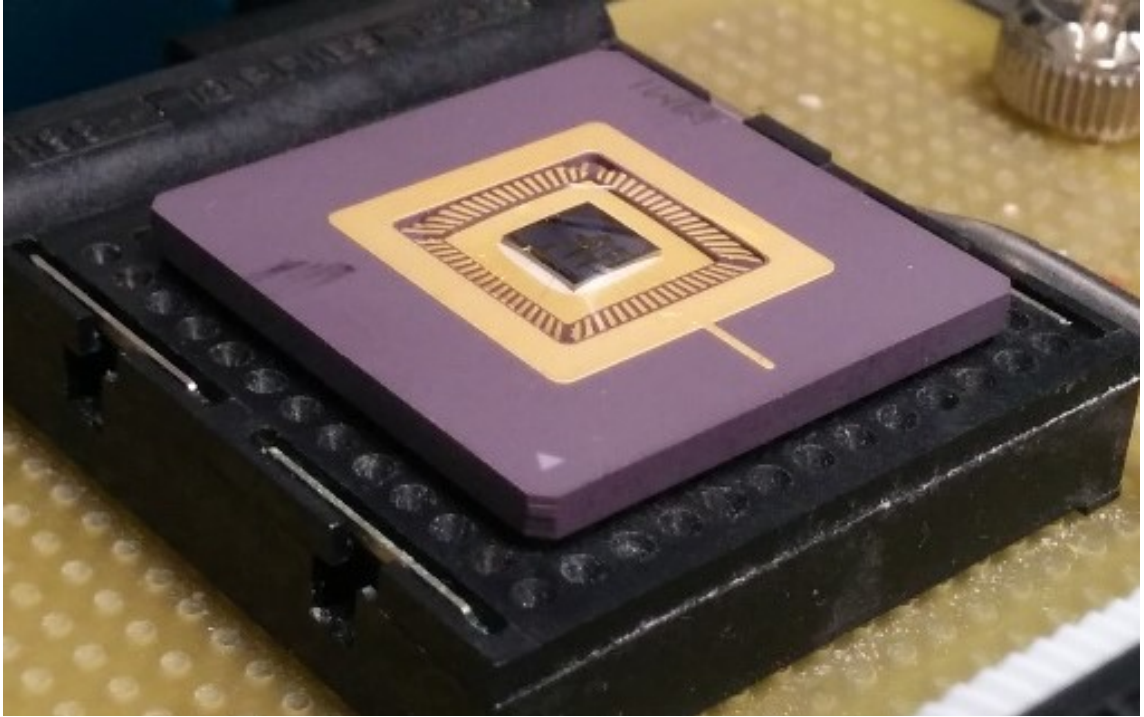


Figure 12: 5x5 mm PolyMUMPs chip submerged in distilled water for cell testing

Once the chip is fully submerged the micropipette is then lowered into the working fluid and moved in place next to the cells to be tested. The operator then applies a small amount of negative pressure to the pipette to draw the cell onto the pipette tip (Figure 13). From here the operator then carefully moves the pipette into position in the jaws of the cell squeezing device. The operator then has to carefully try to release the cell from the pipette by using a combination of small positive pressure at the pipette tip in addition to using the squeezing jaws to provide friction to hold the cell in place (Figure 14). This method takes significant operator training, and even under ideal conditions can be inconsistent.

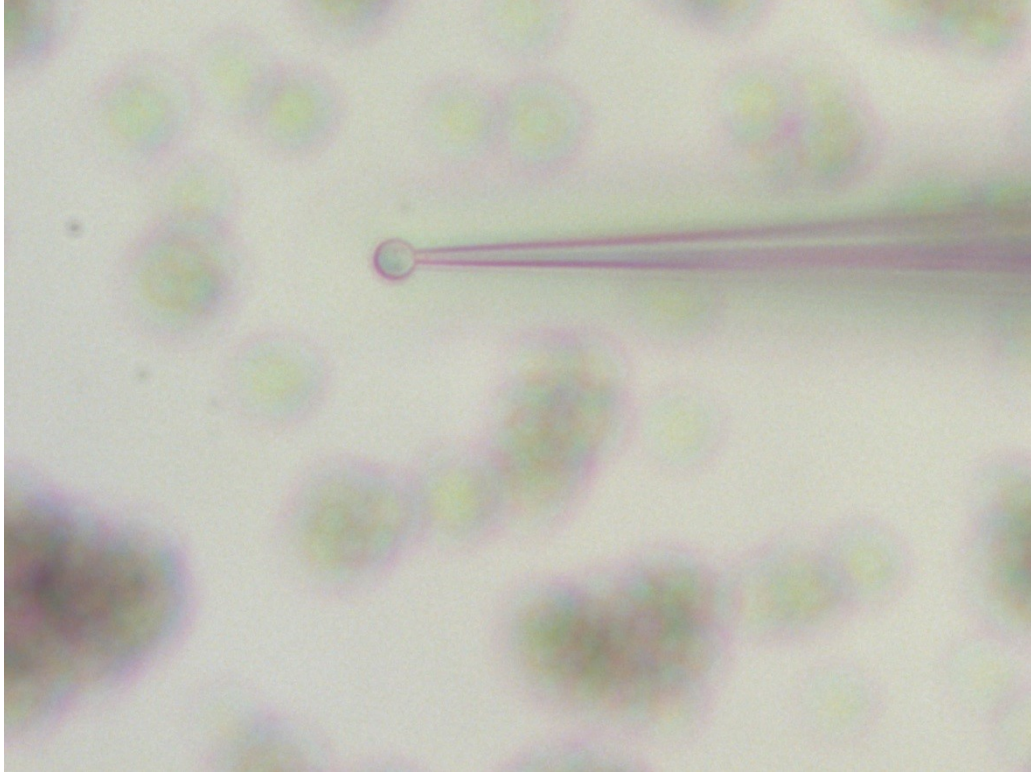


Figure 13: Pipette grabbing yeast cell (cell is 6.5  $\mu\text{m}$ )

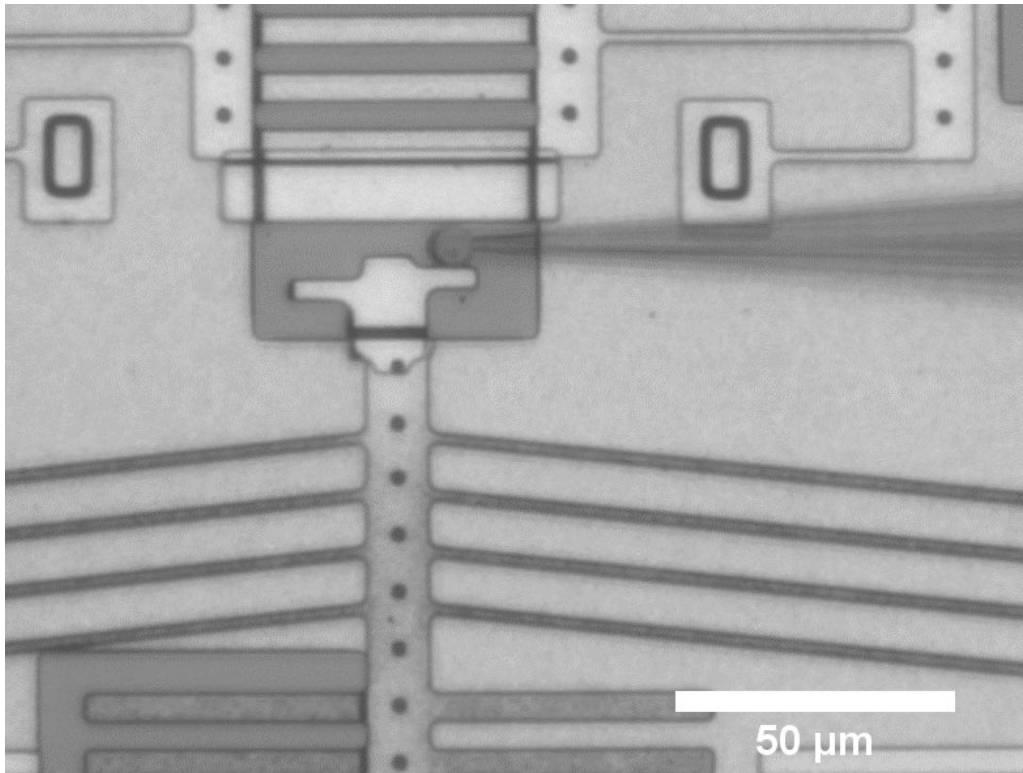


Figure 14: Picture of pipette placing a cell into a squeezing device

After the cell has been placed a series of trials are run to calculate the stiffness of the cell. Post trials the cell must be removed again using the same technique used to initially grab the cell. The removal of the cell post-testing is not only for the purpose of testing another cell, it is also important since if a cell is left in the jaws and allowed to die it may be firmly attached to the point of being un-removable. Due to the amount of operator work required, in addition to the inconsistencies of the placement method has spurred the desire for a new method of cell placement.

## CHAPTER 3: DEP

### 3.1. INTRODUCTION

One potential alternative to manual manipulation is to use dielectrophoretic (DEP) forces to manipulate the cells. Dielectrophoresis is the force on a dielectric particle in a non-uniform electric field. In an electric field a dielectric particle experiences partial charge separation which leads to an induced dipole moment on the particle. When the electrical field is non-uniform there is a net force on the particle. The magnitude and direction of this force is based on the strength of the electric field as well as the dielectric properties of both the particle and the surrounding medium. If the particle is more polarizable than the medium then the particle will move in the direction of the higher electric field (as shown in Figure 15). If the particle is less polarizable than the medium then the particle will move in the direction of the lower electric field.

Dielectrophoresis has been used for many applications such as: particle separation [36], sorting [37] [38], electrical property analysis [39], and controlled particle motion [40] including particle trapping [41].

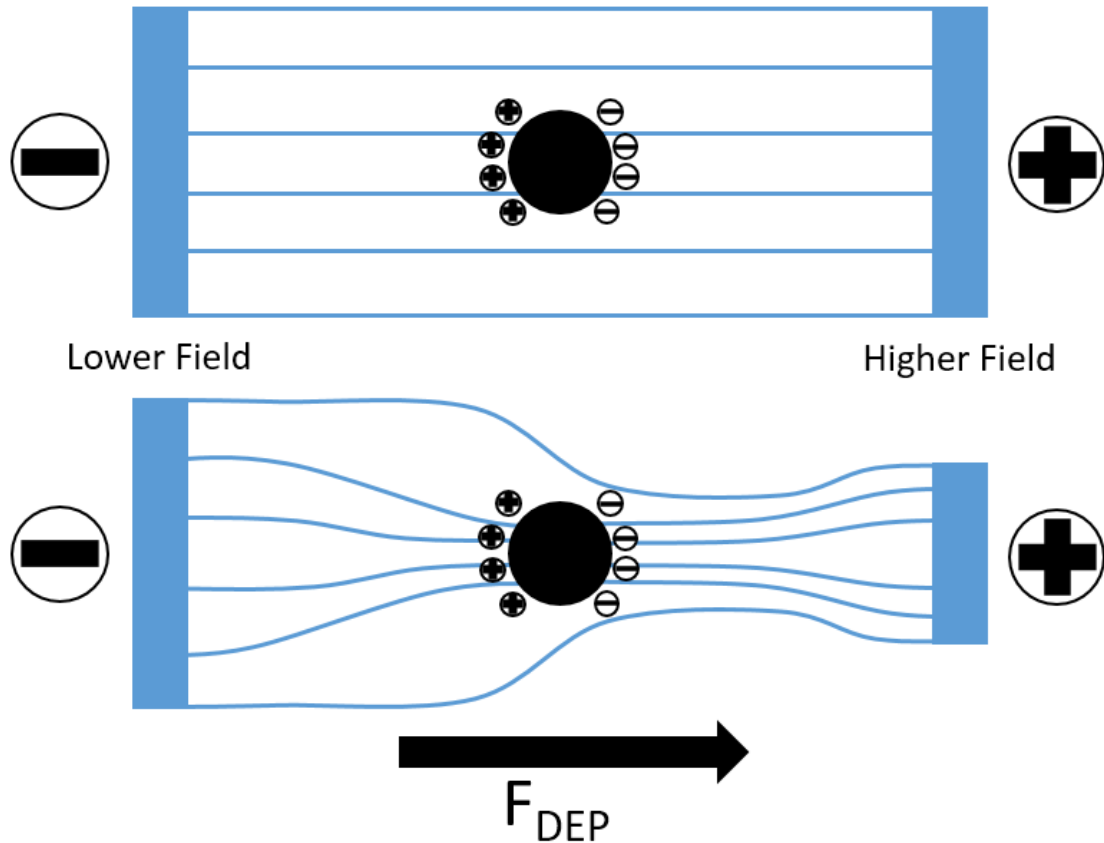


Figure 15: Diagram of DEP force on spherical particle

A material characteristic which partially describes the magnitude of the DEP force is the Clausius-Mossotti factor ( $K$ ). This factor describes the relationship between the conductivity and permittivity of both the particle and the surrounding medium and is described in equation {1}.

$$K(\omega) = \frac{\epsilon_p^* - \epsilon_m^*}{\epsilon_p^* + 2\epsilon_m^*} \quad \{1\}$$

Where  $\epsilon_p^*$  and  $\epsilon_m^*$  are the complex permittivity of the particle and medium respectively.

Equation {2} describes the complex permittivity of either the particle or medium.

$$\epsilon^* = \epsilon - \frac{i\sigma}{\omega} \quad \{2\}$$

Where  $\epsilon$  is the permittivity,  $\sigma$  is the conductivity, and  $\omega$  is the frequency of the applied electrical signal. However the conductivity of the particle is not just a measure of the conductivity of the particle itself, but also a measure of the surface conductivity of the particle. The total conductivity of the particle is shown in equation {3}.

$$\sigma = \sigma_p + \frac{2K_s}{R} \quad \{3\}$$

Where  $\sigma$  is the total conductivity of the particle and surface combined,  $\sigma_p$  is the bulk particle conductivity,  $K_s$  is the surface conductivity which is typically on the order of 1 nS for polystyrene beads [42]. Hughes et al. [42] also showed that the bulk conductivity of the particle is negligible, so the overall conductivity is only a function of the surface conductivity and the radius of the particle.

For the purpose of this DEP work, the x-axis is defined as parallel to the electrode surface, the y-axis is defined as perpendicular to the electrode surface, and the z-axis is defined into the plane of the page (see Figure 16 for a diagram labeling the x-y axis). In dielectrophoresis the real component of the Clausius-Mossotti factor corresponds to the magnitude of the y-directional dielectrophoretic force, whereas the imaginary component corresponds to the magnitude of the x-directional travelling-wave dielectrophoretic force:

$$\langle \vec{F}_{DEP} \rangle = \langle \vec{F}_Y \rangle = \pi \epsilon_m r^3 \text{Re} \left[ \frac{\epsilon_p^* - \epsilon_m^*}{\epsilon_p^* + 2\epsilon_m^*} \right] \nabla |\vec{E}|^2 \quad \{4\}$$

$$\langle \vec{F}_{twDEP} \rangle = \langle \vec{F}_X \rangle = 2\pi \epsilon_m r^3 \text{Im} \left[ \frac{\epsilon_p^* - \epsilon_m^*}{\epsilon_p^* + 2\epsilon_m^*} \right] (\nabla x (\text{Re}[\vec{E}^*] x \text{Im}[\vec{E}^*])) \quad \{5\}$$

### 3.2. DEP ELECTRODE GEOMETRY

Two common array geometries are the 2 and 3 phase electrode arrays. 3 phase electrode arrays employ three different phase shifted electrical signals; typically at 0°, 120°, and 240°. The 3-phase array geometry can be difficult to manufacture due to the requirement for electrical jump overs. Bligh et al [43] showed that an electrode array design that employs only two electrical signals in lieu of three can be used to increase the simplicity of design/production (geometry outlined in Figure 16). 3-phase wiring complexity can be magnified when electrode arrays are not linear, such as in the case of square or circular sorting devices. When using two electrical signals a dual channel waveform generator can be used to ensure the two signals are properly matched, and due to sharing an internal clock the phase of the signals can be easily coupled. If two separate waveform generators are used an external system of frequency and phase coupling is required.

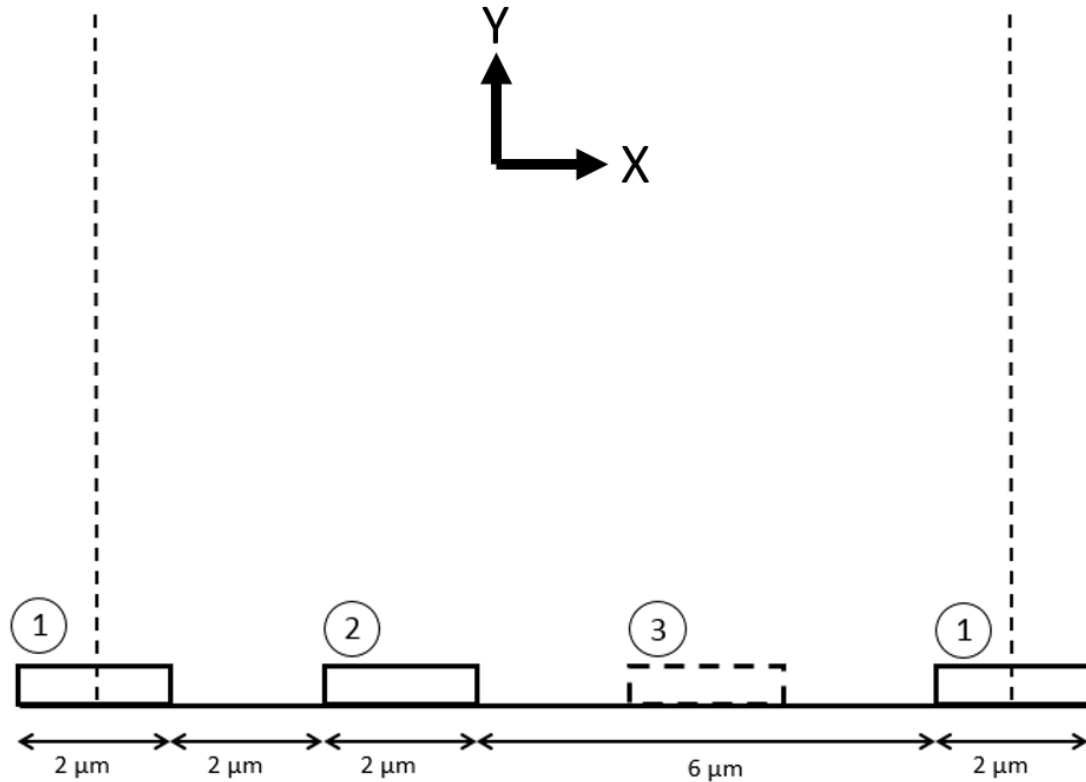


Figure 16: Side profile of 2-phase electrode geometry

For a three phase electrode geometry a more complex waveform generator is required, or an external waveform synchronizer is required. For these reasons a two phase electrode geometry was selected for the design. Figure 17 shows a top view of the two phase electrode array used on the 'MM1' chip which was the chip used in this paper, with the side view shown in Figure 16 for this geometry.

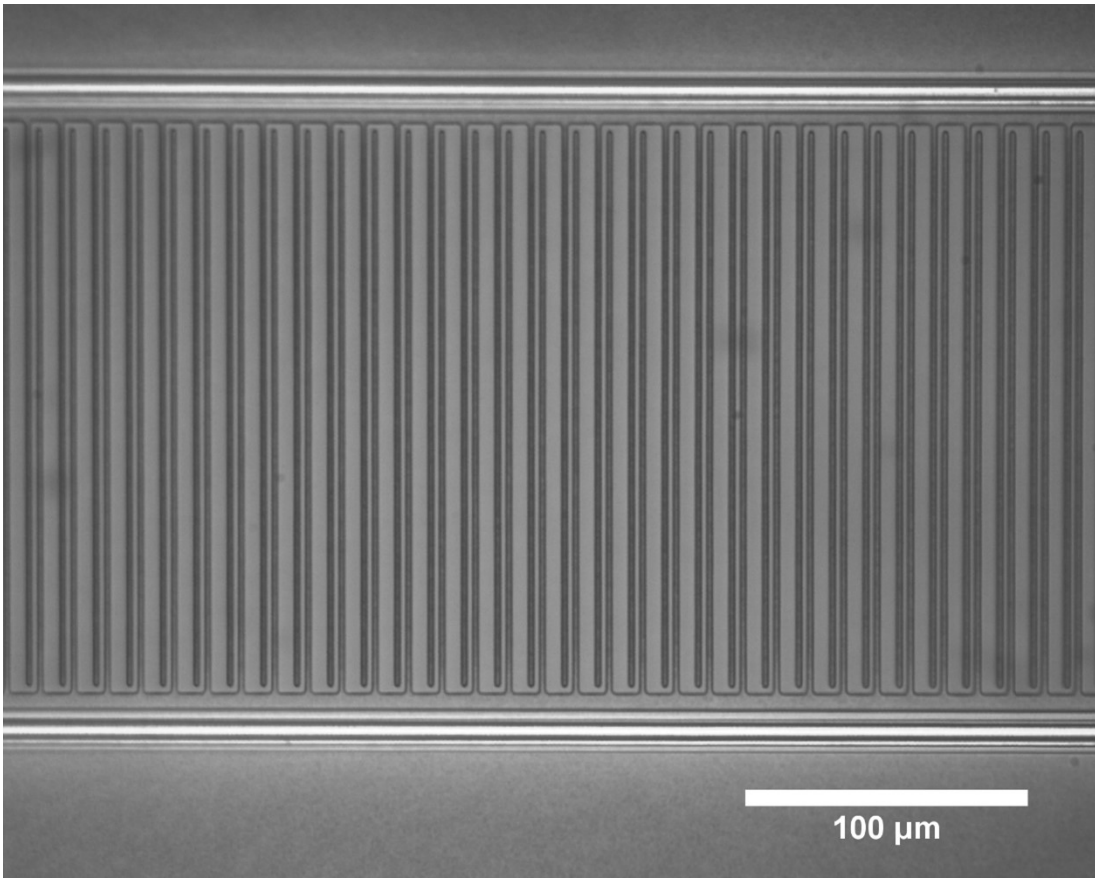


Figure 17: 200µm wide 2-phase DEP array on MM1

Figure 18 shows a close up of the electrode connections. One electrode is connected to the bottom wire with the second connected to the top wire. The relative phase of each of the electrical signals is labeled in the figure.

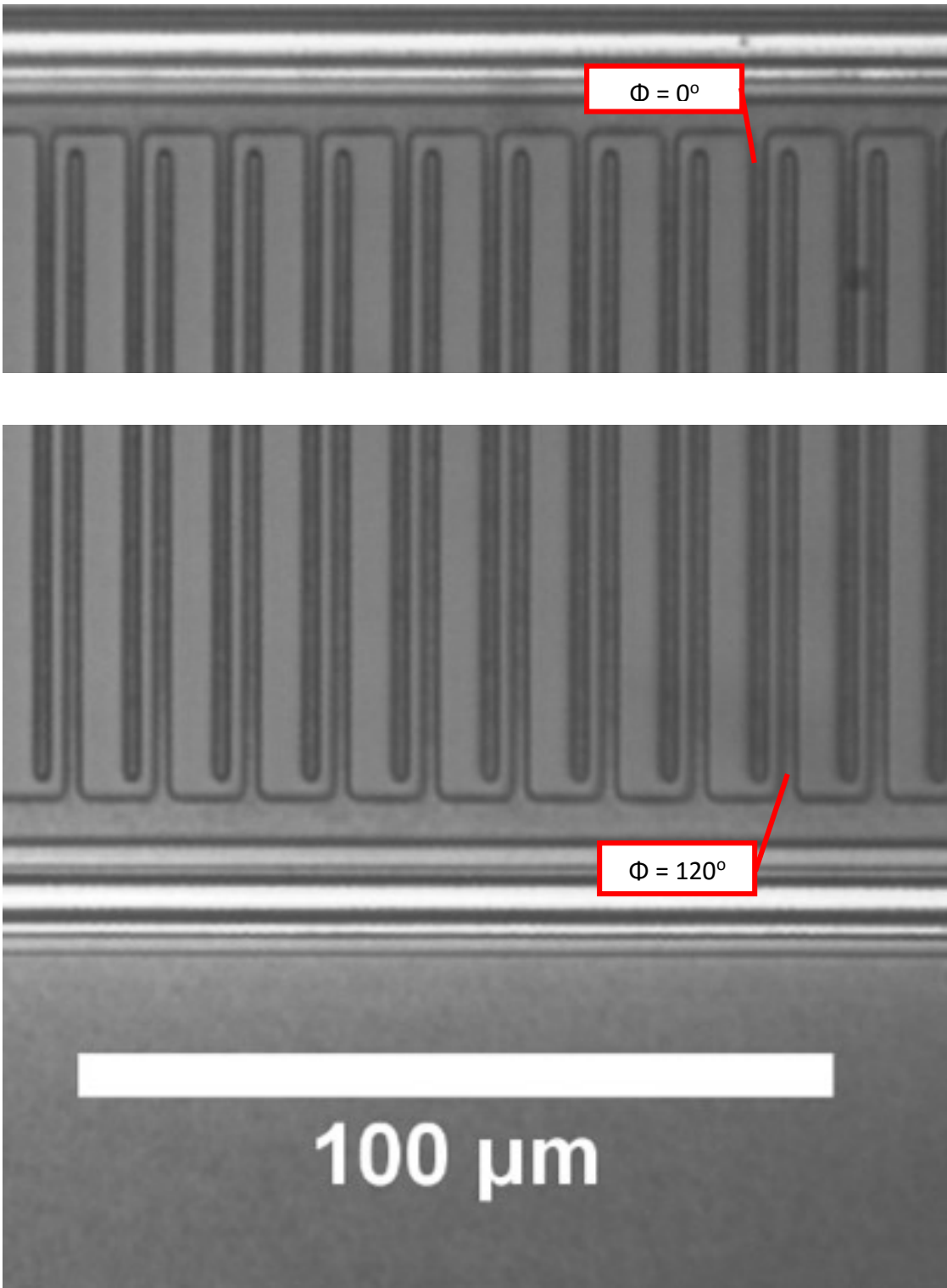


Figure 18: Close up of 2 phase electrode array with phases labeled

The track used for testing also had a reduction in order to attempt to channel the particles into a linear stream directly to the cell squeezing device found on the chip.

Figure 19 shows this reduction in addition to the cell squeezing device. The idea for the chip design was to use the tightening electrode array to funnel a single line of microparticles directly into the jaws of the cell squeezing device.

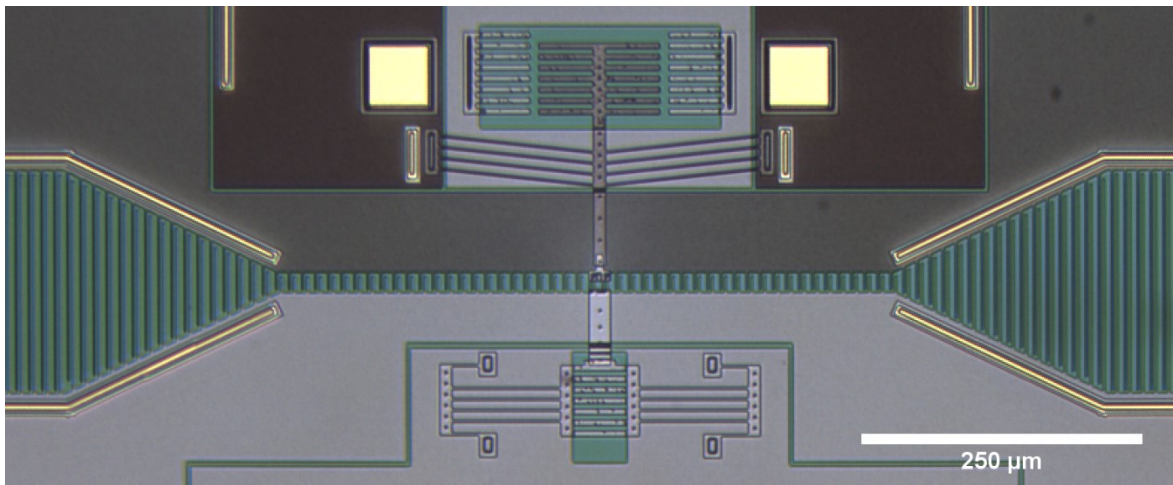


Figure 19: DEP track reduction & cell squeezer (MM1) wide section = 200 μm width, narrow = 20 μm width

### 3.3. DEP SIMULATION

Simulation of the 2 phase electrode array geometry used in the experiments was done using MathWorks-MATLAB® software.

#### 3.3.1. PROBLEM DEFINITION AND BOUNDARY CONDITIONS

Green et al. [44] showed that the time averaged dielectrophoretic force ( $F_{DEP}$ ) and travelling-wave dielectrophoretic force ( $F_{twDEP}$ ) can be calculated from:

$$F_{DEP} = \frac{1}{4} v Re[\alpha] \frac{V_0^2}{d^3} (|\nabla\phi_R|^2 + |\nabla\phi_I|^2) \quad \{6\}$$

$$F_{twDEP} = -\frac{1}{2} v Im[\alpha] \frac{V_0^2}{d^3} (\nabla x (\nabla\phi_R x \nabla\phi_I)) \quad \{7\}$$

Where  $v$  is the volume of the spherical microparticle,  $\alpha$  is the Clausius-Mossotti factor, and  $\phi_R$  and  $\phi_I$  are the real and imaginary components of the electrical potential respectively.

In order to solve for the x-y electrical potential, the electrical potential along the electrode array in the x-direction is first described as the real component of an electrical potential phasor, specifically:

$$\phi(x, t) = Re[\tilde{\phi}(x)e^{i\omega t}] \quad \{8\}$$

$$\phi(x, t) = \text{Re}[\tilde{\phi}(x)e^{i\omega t}] \quad \{9\}$$

Where  $\omega$  is the frequency of the applied waveform,  $x$  is the x-directional position along the lower electrode boundary,  $t$  is time, and  $i$  is the imaginary coefficient ( $i^2 = -1$ ).

$\text{Re}[\dots]$  represents the real component of the electrical potential phasor where:

$$\tilde{\phi} = \phi_R + \phi_I \quad \{10\}$$

The relationship between the x-y electrical potential phasor and the x-y electrical field strength is:

$$E = -\nabla\phi \quad \{11\}$$

Assuming the suspending medium is homogeneous, the equations for the real and imaginary components of the electrical potential phasor can be reduced to Laplace's equation for 2D time averaged space:

$$\nabla^2\phi_R = 0 \quad \{12\}$$

$$\nabla^2\phi_I = 0 \quad \{13\}$$

To solve these series of equations we require boundary conditions for the system. Due to the periodic nature of the system a solution for only one period of the array is required. This periodicity also aids in providing a left and right Neumann boundary condition:

$$\frac{\partial \phi}{\partial x}(0, y) = 0 \quad \{14\}$$

$$\frac{\partial \phi}{\partial x}(12, y) = 0 \quad \{15\}$$

This boundary condition applies to both the real and imaginary solution of  $\phi$  as both must be continuous. The next boundary condition is a Dirichlet boundary condition, which states that as you move away from the electrode surface the electrical potential will eventually go to zero:

$$\phi(x, \infty) = 0 \quad \{16\}$$

Figure 20 shows the boundary conditions applied to the electrode geometry shown in Figure 16. It is presumed that the electrical potential in the lower boundary between the electrode arrays is zero as the area between electrodes is comprised of Silicon Nitride which is used as an electrical insulator. From these conditions the general Laplace equation can be solved for the 2D electrical potential field.

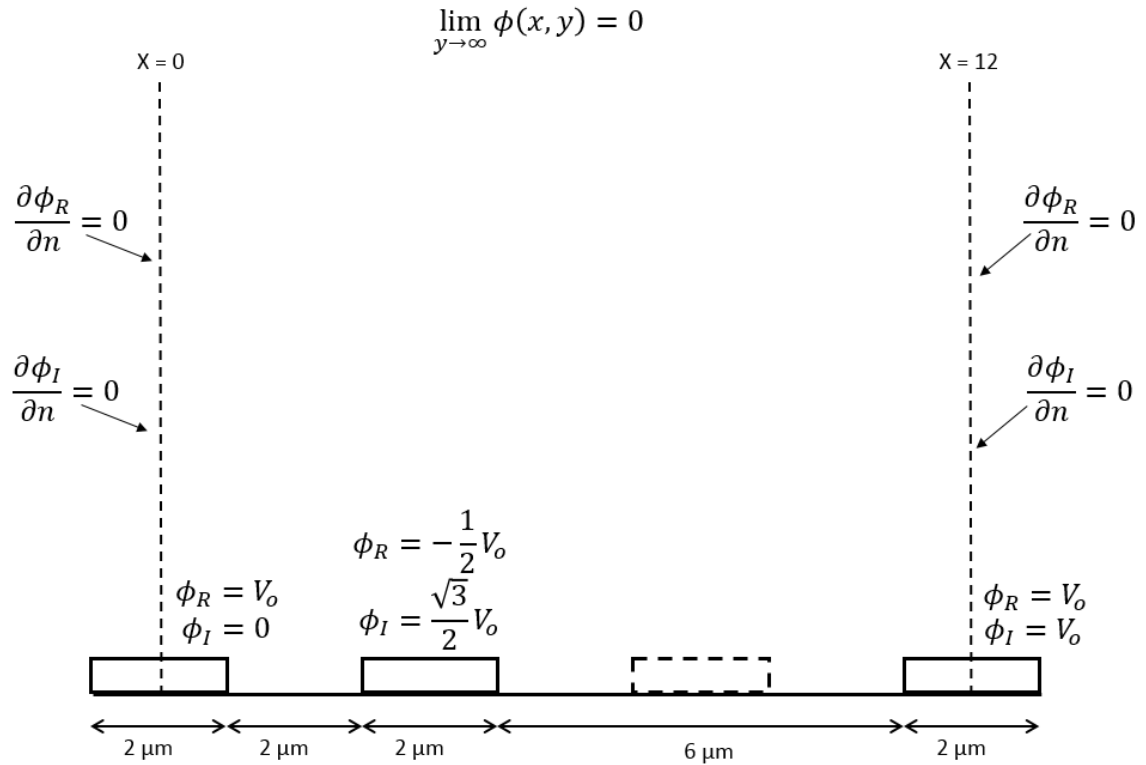


Figure 20: Electrode geometry with boundary conditions shown

### 3.3.2. SOLUTION

In order to solve the general Laplace equation a separation of variables method was used. As the real and imaginary solutions share 3 out of 4 boundary conditions their solution is identical until equation {21}. The general solution of the Laplace equation before boundary conditions are taken into account is:

$$\phi(x, y) = (A \cos \lambda x + B \sin \lambda x)(D e^{\lambda y} + E e^{-\lambda y}) \quad \{17\}$$

Where  $A, B, C, D$ , and  $\lambda$  are all constants which are calculated from the boundary conditions. By taking the Neumann and Dirichlet boundary conditions outlined in equations {14} - {16} into account the solution becomes:

$$\phi(x, y) = \sum_{n=1}^{\infty} \phi_n(x, y) \quad \{18\}$$

$$\phi_n(x, y) = C_n e^{-\lambda_n y} \cos \lambda_n x \quad \{19\}$$

Where:

$$\lambda_n = \frac{n\pi}{12} \quad \{20\}$$

And  $C_n$  is calculated from the final Dirichlet boundary condition (the lower boundary condition on the electrode array) and is different for the real and imaginary solution.

$$C_n = \frac{1}{6} \int_0^{12} f(x) \cos \lambda_n x dx \quad \{21\}$$

Where  $f(x)$  is the piecewise equation describing the lower boundary condition of electrical potential on the electrode surface.

Figure 21 shows the solution of x-y electrical potential (both real and imaginary components).

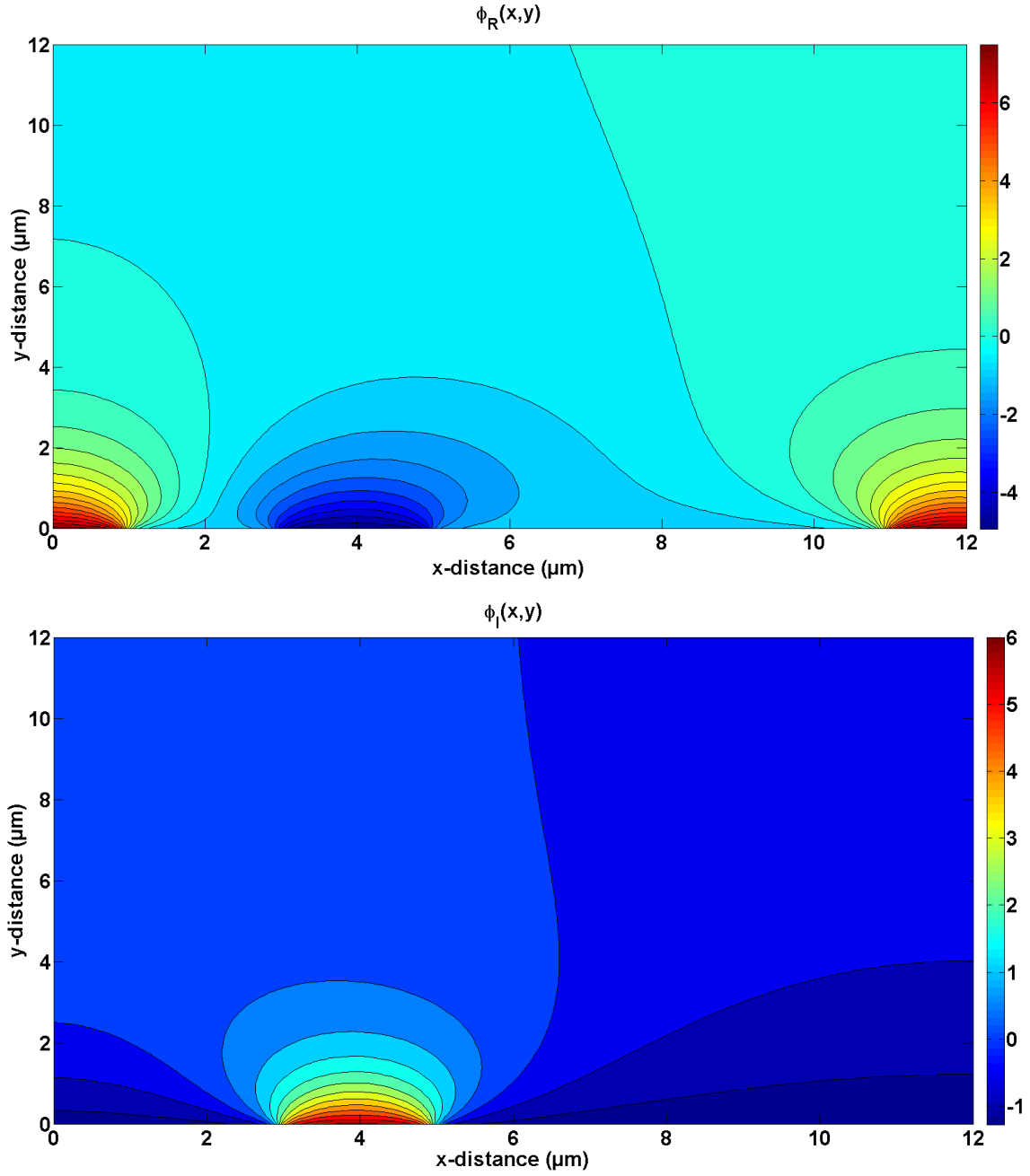


Figure 21: Simulation of electrical potential around arrays (Top: real, bottom: imaginary components)

The solution for the electrical potential was found to converge within  $\sim 100$  iterations (within  $<2\%$  of final values) however for greater accuracy 1000 iterations were used for the final solution in order to further increase accuracy. With 1000 iterations both the real and imaginary solution convergence errors were less than  $10^{-12}$ .

Next the Clausius-Mossotti factor was calculated (with respect to the frequency of the applied electrical signal). The Clausius-Mossotti factor is by definition complex. The real component of the Clausius-Mossotti factor corresponds to the effect (magnitude and direction) of the dielectrophoretic force (Y direction repulsion or attraction from/to the array), while the imaginary component corresponds to the effect of the travelling wave dielectrophoretic force (X direction propulsion along the array). The equations that describe the magnitude and direction of these forces are outlined in equations {6} and {7}. A plot of the real and imaginary components of the Clausius-Mossotti factor for a  $6\ \mu\text{m}$  polystyrene bead in pure ethanol is shown in Figure 22 as an example of the typical frequency dependence of the Clausius-Mossotti factor. Note that it is relatively uniform then drops at a frequency in the range of 100 kHz before reaching a local minimum around 1 MHz (for the imaginary component).

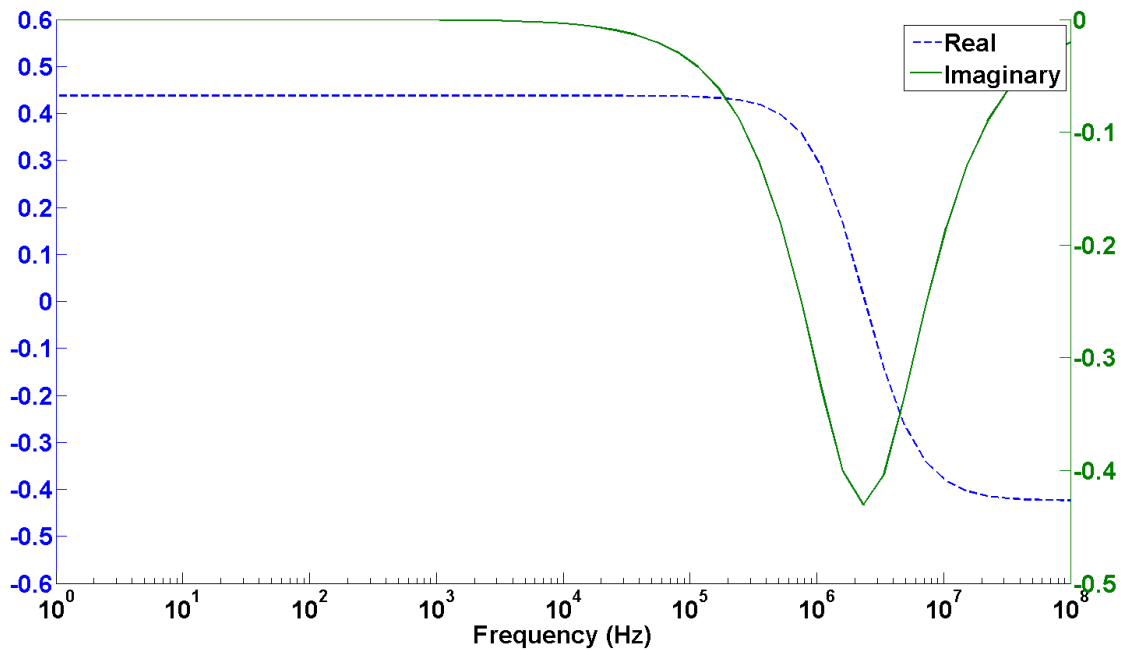


Figure 22: Clausius-Mossotti Factor vs Frequency for ethanol

The Clausius-Mossotti factor for working fluid used in this paper (0.1M Sorbitol, with 6  $\mu\text{m}$  polystyrene beads) is flat over a large range and does not vary greatly up to the working frequency of 1MHz (see Figure 23), though it does peak at much higher frequencies. Figure 23 shows the Clausius-Mossotti factor for 0.1M sorbitol at higher frequencies. The peak for sorbitol is still higher than shown (between 100  $\rightarrow$  1000 MHz).

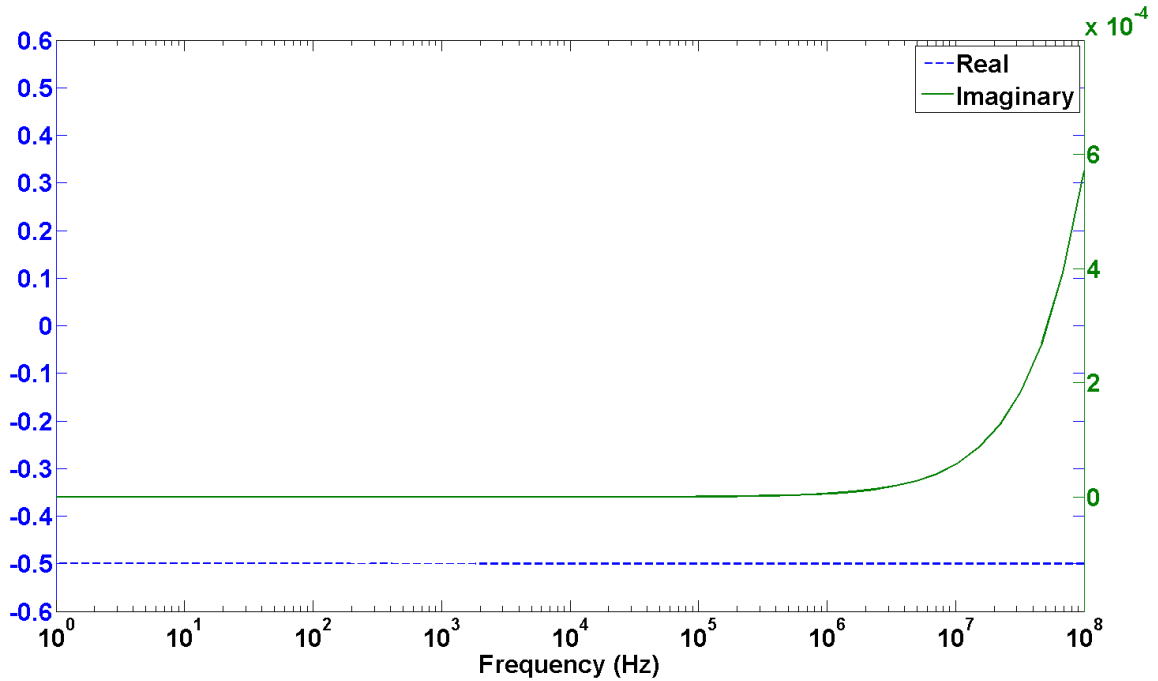


Figure 23: Clausius-Mossotti factor for 0.1M sorbitol at high frequencies

Values for the Clausius-Mossotti factor for the working frequency of 1 MHz were calculated as:

$$Re(K) = -0.499 \quad \{22\}$$

$$Im(K) = 5.736 * 10^{-6} \quad \{23\}$$

In an ideal situation the real component of the Clausius-Mossotti factor will be negative in order to provide a small y-direction repulsive dielectrophoretic force on the particle (away from the electrode surface). However for our case the imaginary component is positive, albeit small. This will cause the particle to be pulled slightly towards the electrode surface, however the x-direction travelling wave force is high enough that the

particle will still move even with the y-directional attractive force. Due to the near-independence of frequency an experimental frequency of 1MHz was chosen as it is high enough to prevent any potential electrolysis at the working voltages and well within the working band of the waveform generator. Using the values for the Clausius-Mossotti factor at this frequency, the electrical potential field (as shown in Figure 21), and equations {6} and {7} the dielectrophoretic and travelling wave dielectrophoretic forces are calculated and shown in Figure 24 and Figure 25. It should be noted that MATLABs gradient function computes the gradient numerically which was causing large errors in the solution due to numerical approximation. For this reason the solution of the gradient was computed analytically by direct differentiation of the series which significantly reduced the error and noise in the final solution.

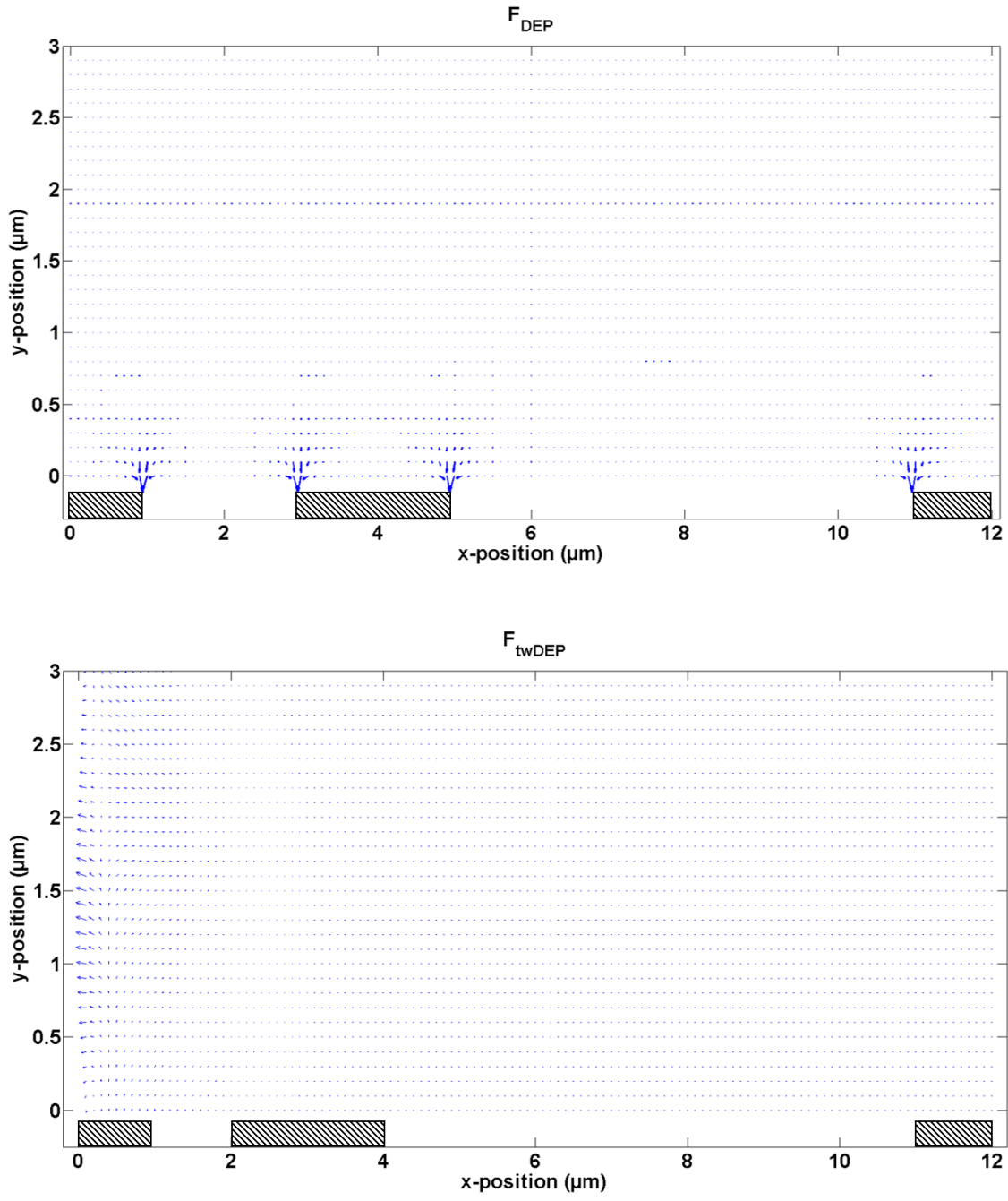


Figure 24: Simulation of TOP: dielectric ( $F_y$ ) & BOTTOM: travelling wave ( $F_x$ ) dielectric force vectors

Figure 25 shows a close up of the  $F_x$  travelling wave dielectrophoresis force vectors from the left-most electrode edge in Figure 24.

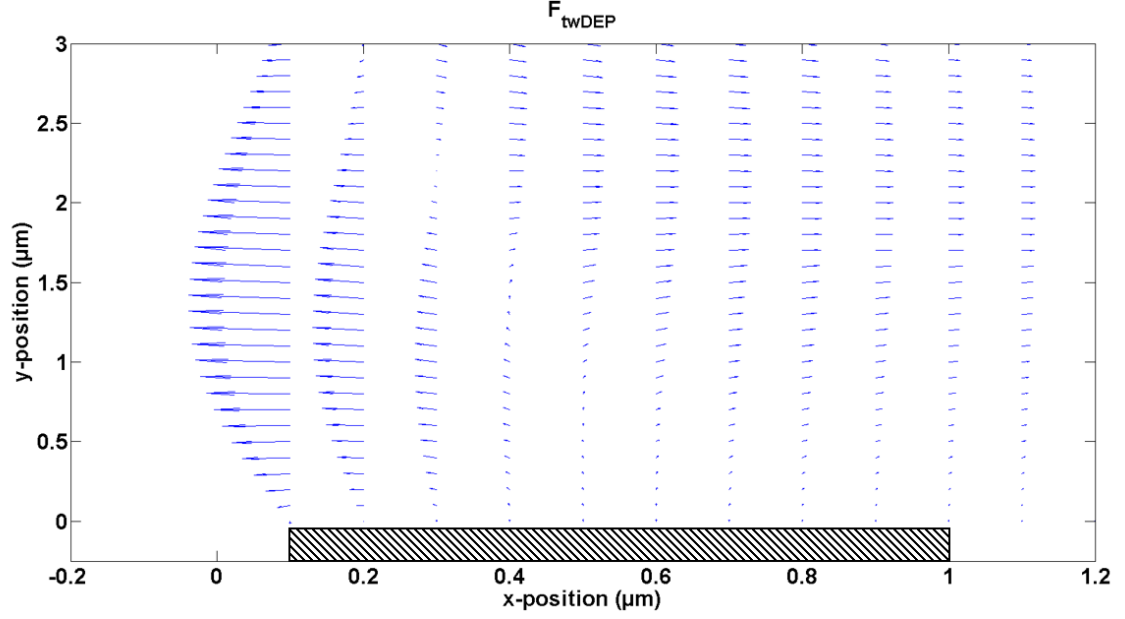


Figure 25: Close up of  $F_x$  travelling wave dielectrophoretic forces from electrode edge

From here we can calculate the steady state x-direction velocity of a particle.

$$m \frac{dv}{dt} = F_{twDEP} - F_{\eta} \quad \{24\}$$

Where  $F_{\eta}$  is the force from Stokes drag. From here when acceleration is zero (steady-state):

$$F_{twDEP} = F_{\eta} = 6\pi\eta r v \quad \{25\}$$

$$v_{particle} = \frac{2\pi\epsilon_m r^3 \text{Im} \left[ \frac{\epsilon_p^* - \epsilon_m^*}{\epsilon_p^* + 2\epsilon_m^*} \right] \frac{V_0^2}{d^3} (\nabla x (\text{Re}[\vec{E}^*] x \text{Im}[\vec{E}^*]))}{6\pi\eta r} \quad \{26\}$$

$$v_{particle} = \frac{\epsilon_m r^2 \text{Im} \left[ \frac{\epsilon_p^* - \epsilon_m^*}{\epsilon_p^* + 2\epsilon_m^*} \right] \frac{V_0^2}{d^3} (\nabla x (\text{Re}[\vec{E}^*] x \text{Im}[\vec{E}^*]))}{3\eta} \quad \{27\}$$

By using these equations and the travelling wave dielectrophoresis force vectors from Figure 24, the theoretical particle velocity of a 6  $\mu\text{m}$  polystyrene bead in 0.1 M sorbitol was calculated and shown in Figure 26.

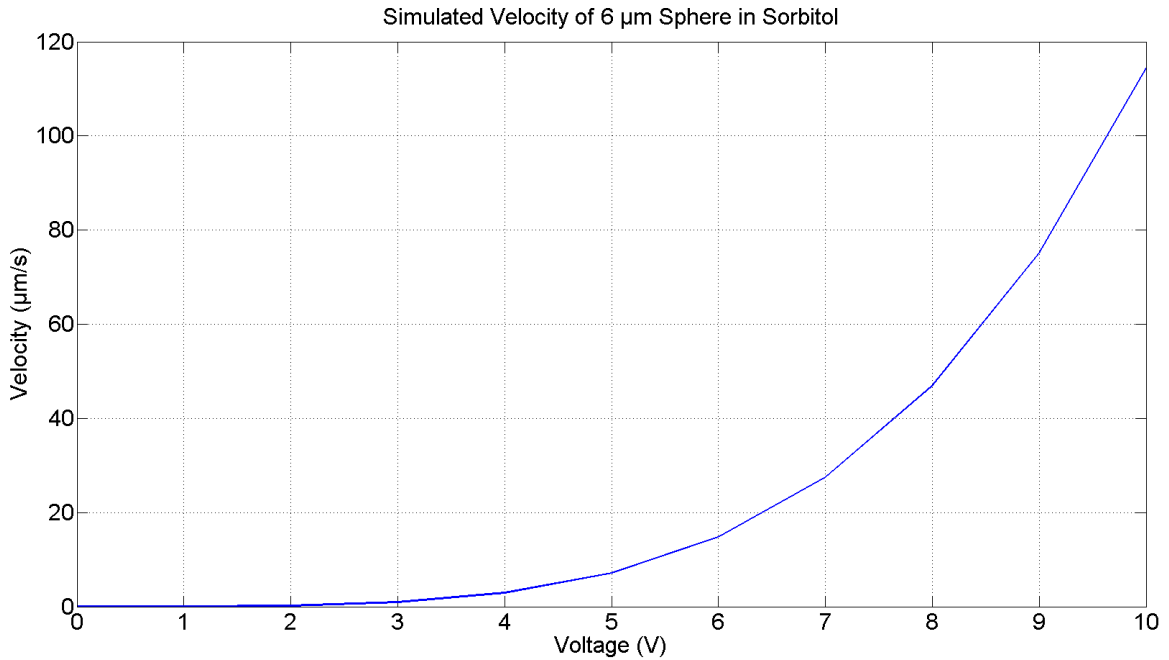


Figure 26: Simulated DEP particle velocity vs applied voltage

These values will be compared with experimental values in chapter 6.

### 3.4. DEP PROBLEMS

Dielectrophoresis may be a partial solution for increasing throughput for cell testing, however it does not answer the problem of requiring the entire chip to be submerged in the working fluid. In order to address this issue polymer moulds were used to provide custom re-useable microfluidic channels to contain the areas with working fluid and separate them from the dry sections of the chip.

## CHAPTER 4: MOULDS

### 4.1. MOULD INTRODUCTION

Kraton reversibly bonded polymer moulds were used as a method to produce reusable microfluidic channels. The term reversibly bonded refers to the ability to easily remove the mould from the device after it has been used without damaging the chip, thus allowing for reuse of the chip. The use of polymer moulds not only allows for microfluidic channels (something which is not typically possible with the general PolyMUMPs production method), but they also allow the compartmentalization of the MEMS chip. This allows for segregation of wet and dry environments, as well as preventing the potential for cross contamination when biological samples are being tested. This can be of significant importance as biological cells can adhere to the substrate of an entire PolyMUMPs chip if allowed to sit for too long. Figure 27 shows contamination of a chip from biological cells.

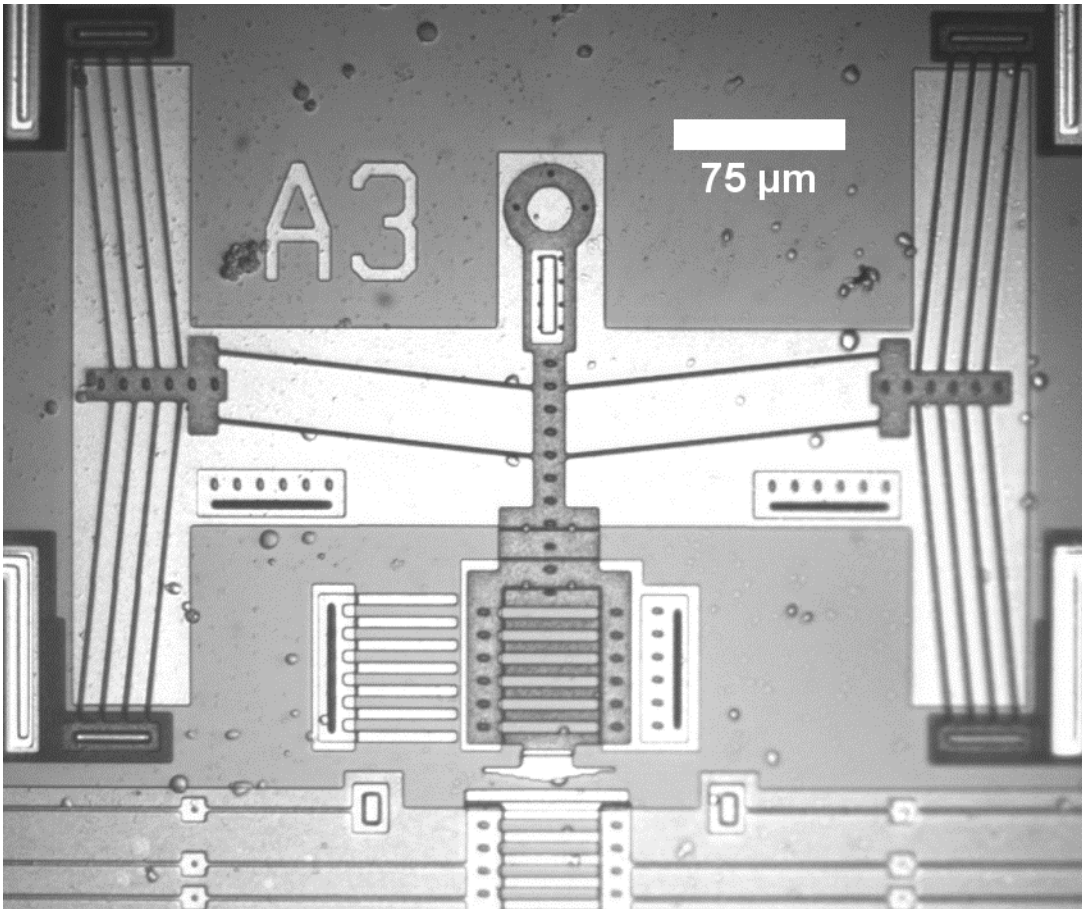


Figure 27: PolyMUMPs chip covered in adhered dried cells

## 4.2. MOULD BACKGROUND

Using moulds is not the only method of producing microfluidic channels for MEMS applications. Multiple methods are available, however all have their limitations. The most basic form of producing microfluidic channels can be done using the PolyMUMPs design process. This method however is limited to a channel length of 30 µm, and a height of 2.75 µm as per the design rules [20]. Therefore this method is not suitable for applications with biological cells as the diameters of the cells can be much larger than the 2.75 µm maximum imposed by the PolyMUMPs design rules. Another limitation of

this method is that the microfluidic channels are opaque as they are made from the structural polysilicon material. This would not allow the user to easily monitor the flow of microparticles (or cells).

Another method used to produce microfluidic channels on MEMS devices is a wafer-to-wafer bonding [45]. A wafer-to-wafer bonding process uses a second polysilicon wafer with a negative pattern. This negative is then placed face-down on the original wafer. It is then bonded in place using methods such as Silicon-to-Silicon anodic bonding [46], Silicon fusion bonding [47], or ultrasonic bonding [48]. This method is used more frequently for producing pressure sensors, and can produce microchannels and cavities with a very high resolution. Again, one of the drawbacks of this technology is that the microfluidic channels are opaque so any optical measurements in channel are not possible. In addition to this the process of wafer-to-wafer bonding is an irreversible process. This can cause issues for reusing the chip in biomedical applications as the working area is not as easily cleaned as if the microchannels could be opened for cleaning. These technologies can also require significant equipment for production, therefore a new method of microfluidic channel production was desired.

The production of microfluidic channels using moulds is not a new idea. Currently the standard for academic microfluidics production is PDMS (Polydimethylsiloxane) [49]. PDMS is inexpensive, optically transparent, produced via a mould technique similar to the Kraton polymer in this thesis, and are biocompatible [49]. PDMS however does have its limitations such as its partial incompatibility with metal adhesion [50]. Kraton styrene-ethylene/butylene-styrene (SEBS) G1657 M used to produce the moulds, has

been shown to have a significantly faster cure time (of only ~30 seconds) with a total production time of under 2 minutes [15]. Wasay et al. [15] also showed the Kraton thermoplastic elastomer mould provided adhesion strengths over 10 times that of a comparable PDMS based reversibly bonded mould. The goal of this work was to integrate the Kraton thermoplastic moulds with a PolyMUMPs based MEMS chip. As described in section **Error! Reference source not found.** the material selection is not reviewed, nor are the mould production method and the design of the gecko structures.

### 4.3. PRODUCTION

Due to the quantity of moulds required for testing; moulds were produced in house at Dalhousie using negatives provided by Dr. Dan Sameoto and Abdul Wasay of the University of Alberta. Dr. Sameoto and Abdul. Our main focus has been the implementation of the mould technologies pioneered by Dr. Sameoto for use with MEMS devices, specifically to create microfluidic channels on PolyMUMPs based devices. However in order to do this the manufacturing process designed by Dr. Sameoto had to be recreated in house.

The following outlines the steps for reliably producing Kraton polymer moulds from a silicone negative.

- 1) Kraton G1657 polymer beads are melted on a silicon wafer which is heated on a hot plate to 200°C (Figure 28)



Figure 28: Image of Kraton beads melting on 2" silicon wafer

2) The melted beads are then pressed and smoothed into a puck shape (Figure 29)

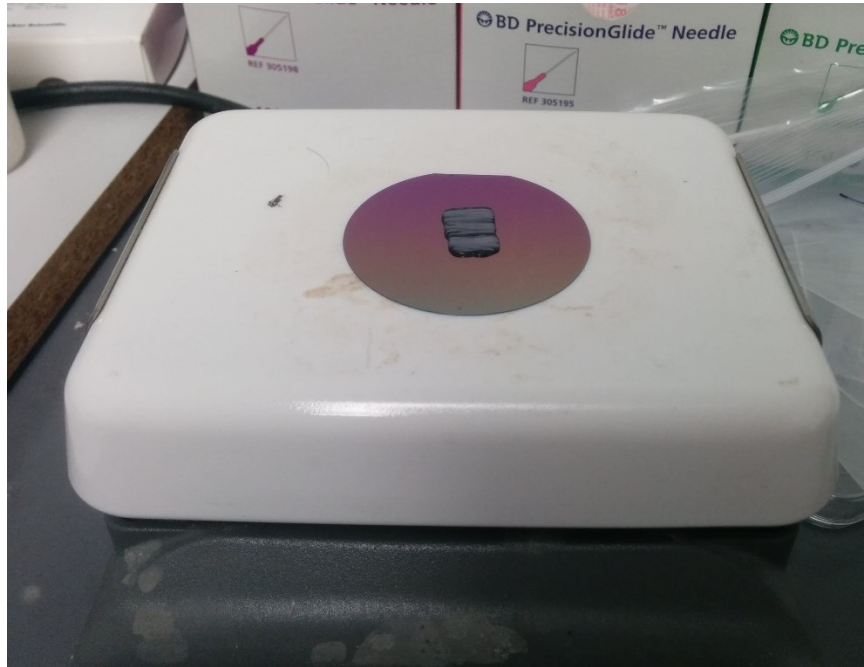


Figure 29: Melted Kraton beads pressed

- 3) The partially pressed Kraton puck is then pressed with another silicon wafer providing a backing and a 960 g weight for 45 seconds to smooth the puck. Figure 30 shows the Kraton puck once the weight and top wafer have been removed.



Figure 30: Kraton puck smooth from compression

- 4) The puck is then left to cool until it reaches room temperature. It is then flipped on the silicon wafer to allow the flattest side to be facing upwards. This puck is then re-melted at 200°C as per step (1) and two 0.5mm glass spacers are placed onto the silicon wafer in order to provide an even final mould (Figure 31).



Figure 31: Kraton puck re-melting

- 5) Next the mould negative is placed face-down onto the melted puck. A Fisherbrand® glass microscope slide is then used to provide a rigid backing for the negative and a 960g weight is then placed onto the backing (Figure 32 & Figure 33).



Figure 32: Kraton puck with negative

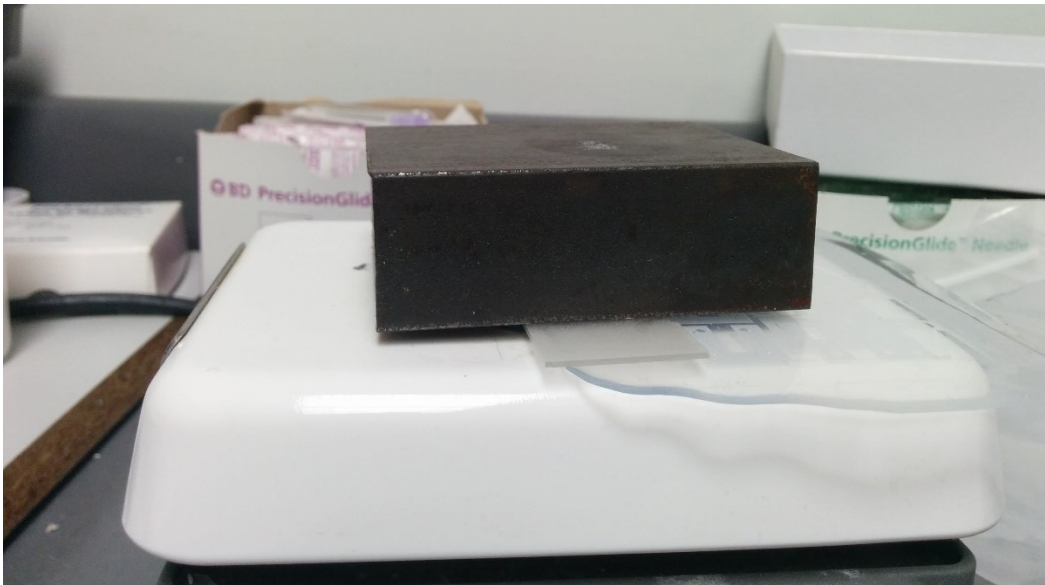


Figure 33: Kraton puck with negative being pressed

- 6) From here the mould with negative is left for 30 seconds before the heat source is turned off and the mould with negative is removed from the hot plate. It is left

until it has cooled to room temperature, then is removed from the negative by hand (Figure 34).

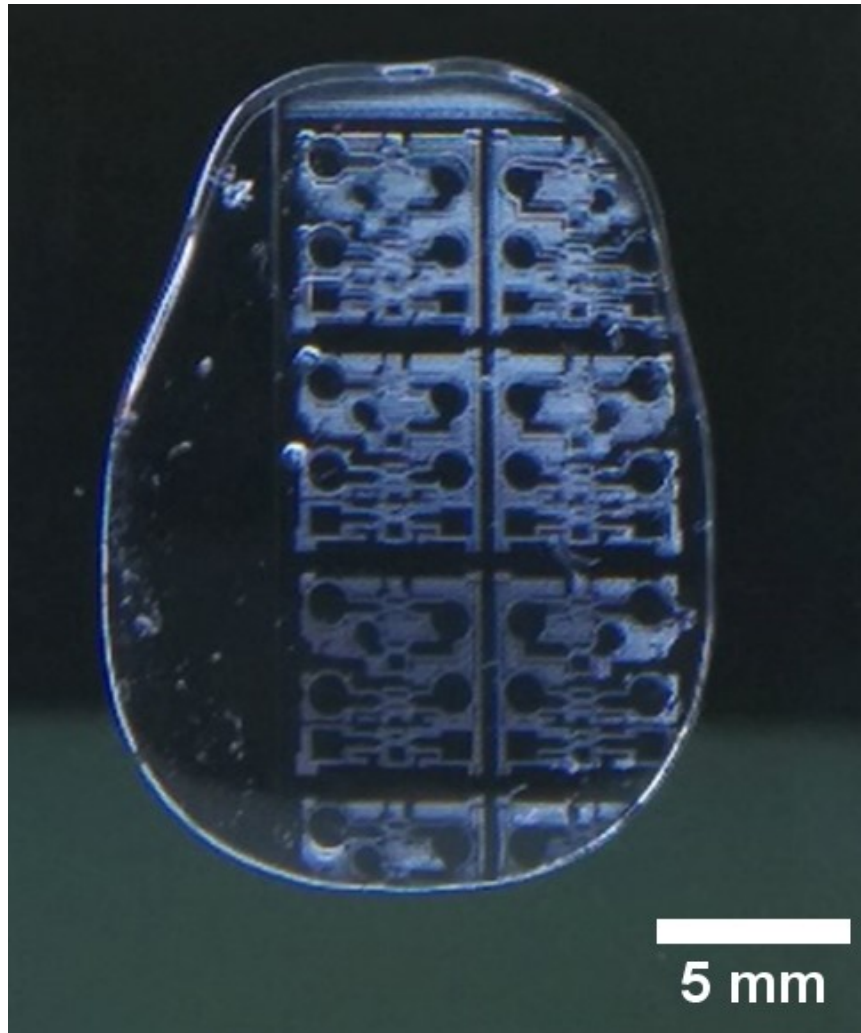


Figure 34: Mould separated from the negative note 0.5 mm diameter ports

- 7) Once the mould has been removed from the negative it is almost ready for use. The last step in the process is to cut the individual mould from the puck using a hobby knife, and punch two input/output ports for the microfluidic channel using a Robbins Instruments 0.5 mm biopsy punch.

Figure 35 shows a mould once all the production steps are finished, with Figure 36 showing a close up of the microfluidic channels. The use of these ports is outlined further in section 5.

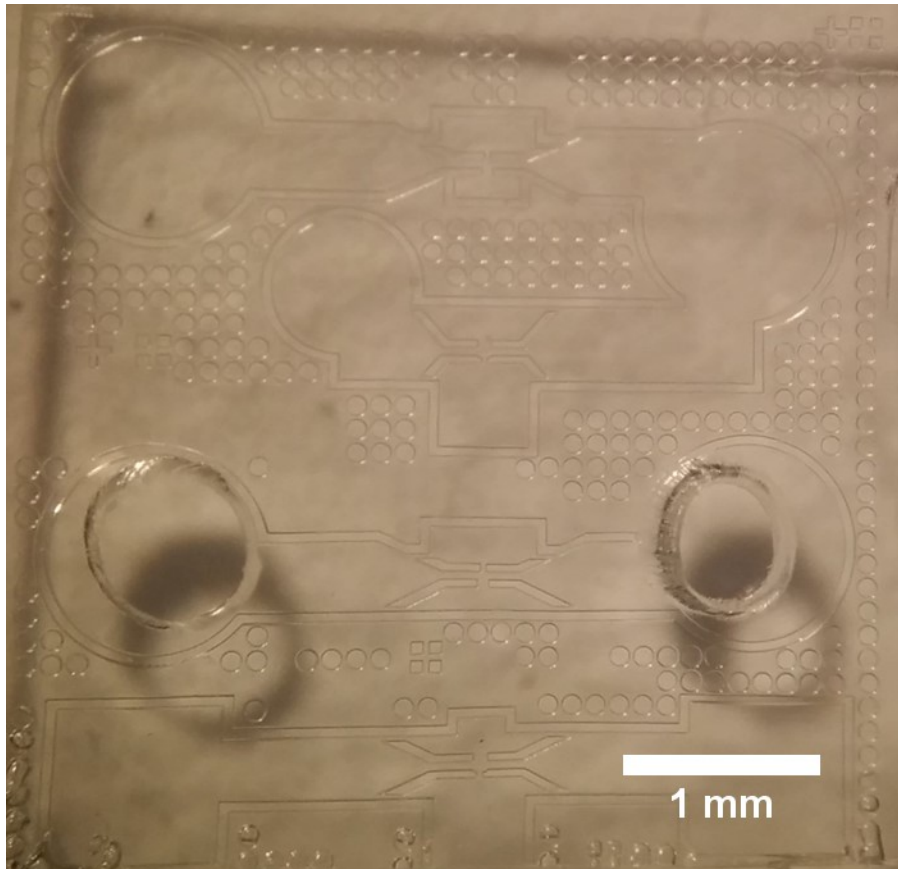


Figure 35: Mould cut from puck with channel holes punched

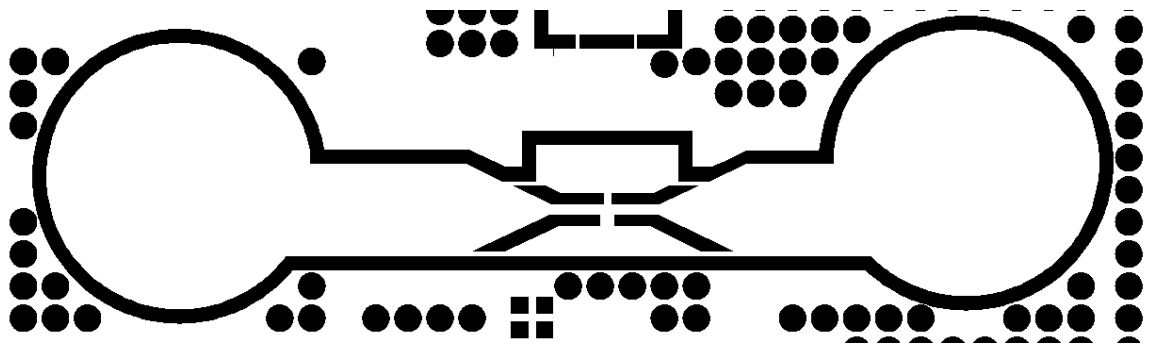
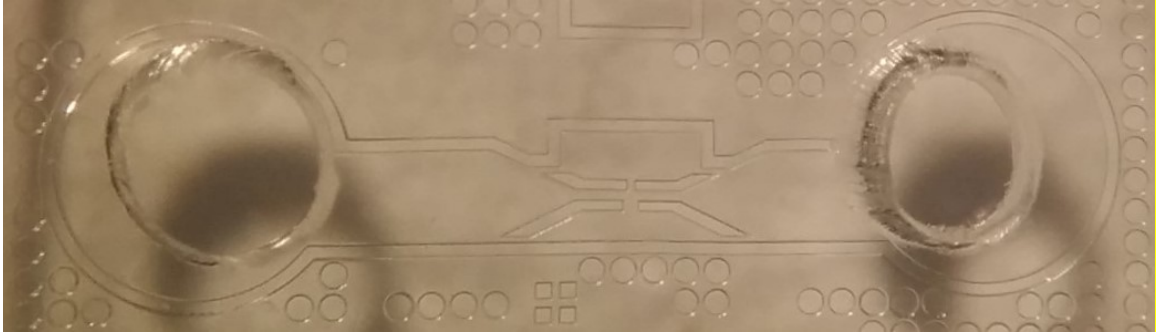


Figure 36: Close up of microfluidic channel in mould compared to design, circular ports are 1 mm diameter

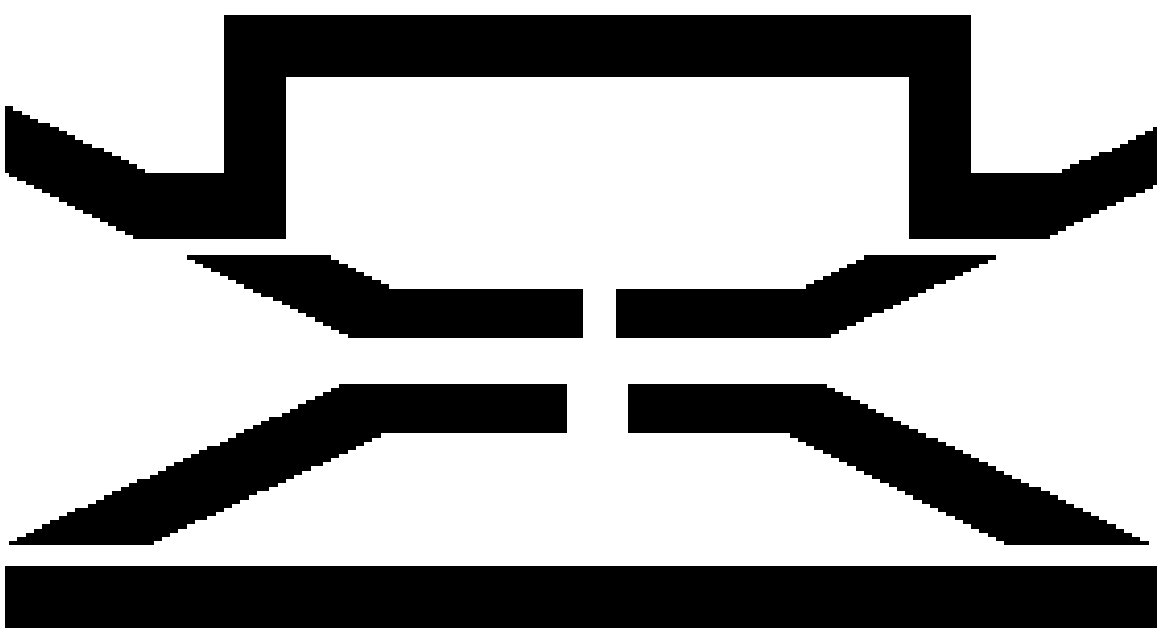
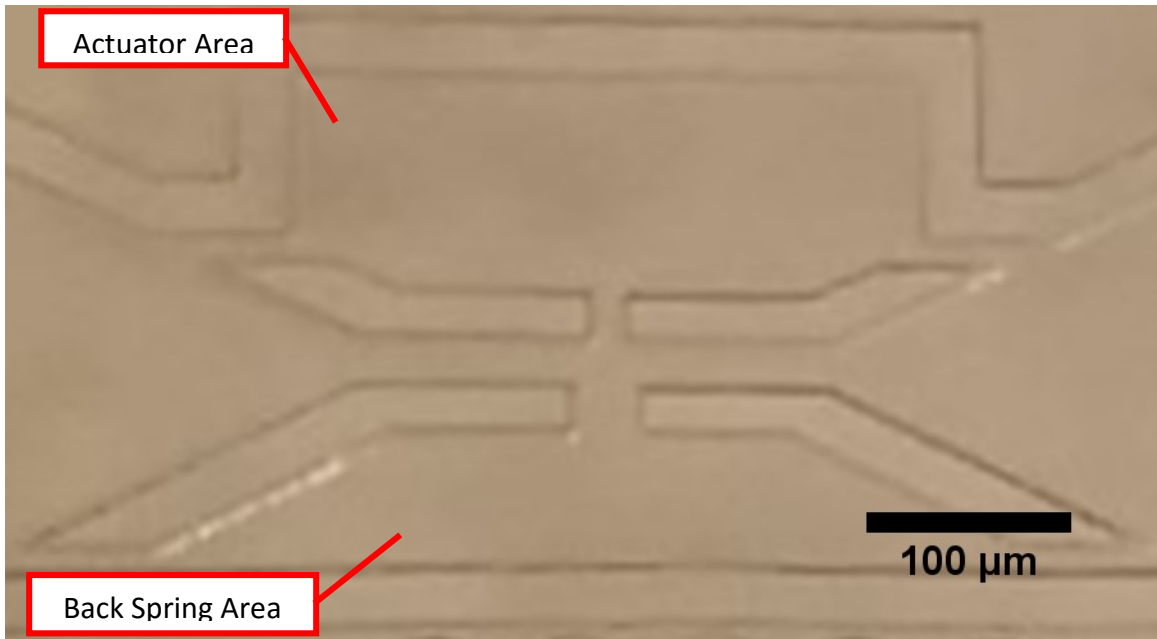


Figure 37: Close up of actuator and backspring area, top: fabricated mould, bottom: mould layout design

Some problems were discovered during the initial production of the moulds. It was found that the mould negative was deteriorating quickly over time. As the negatives were continuously used the mould edges were becoming rough. Figure 38 and Figure 39 show SEM microphotographs outlining this damage. From the images it was clear that material was being etched away from the negative. Figure 39 clearly shows that material was being added to the walls of the mould. It was found that the ethanol used to clean the negative was etching away the mould negative over time. Once this was discovered the cleaning method was changed from an ethanol wipe to a different method. Cleaning procedure of the mould negative now consists of heating a polystyrene petri dish on the mould negative to approximately 200°C until the material begins to melt. Once partially fluidic the petri dish material seeps into the mould negative. Once suitably melted (usually within 2 minutes) the mould negative with molten petri dish is removed from the heat source and allowed to cool. Once cooled the re-solidified petri dish is removed from the negative. During the melting and re-solidifying the molten petri dish material picks up dust and debris that can make its way into the negative.

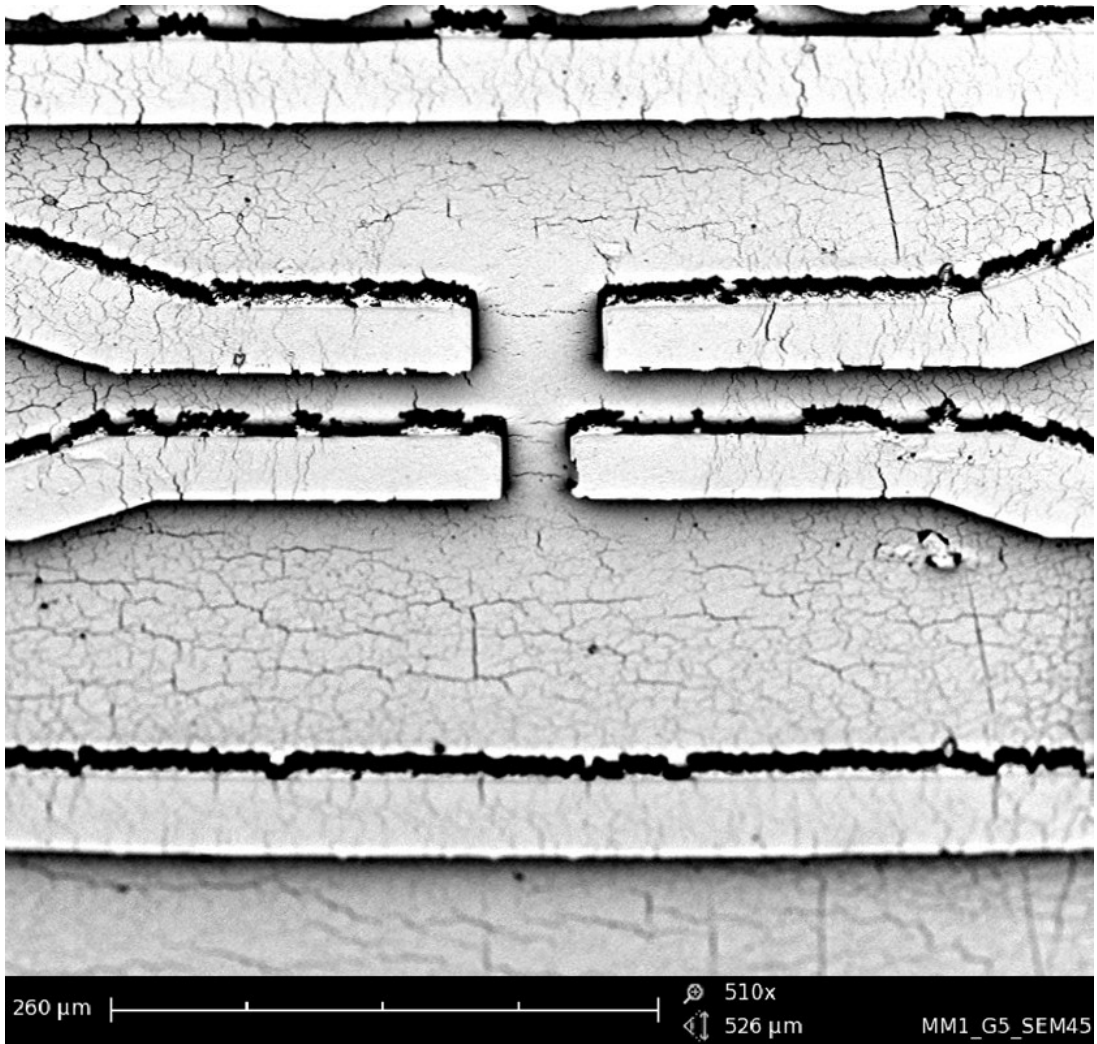


Figure 38: SEM image of mould degradation

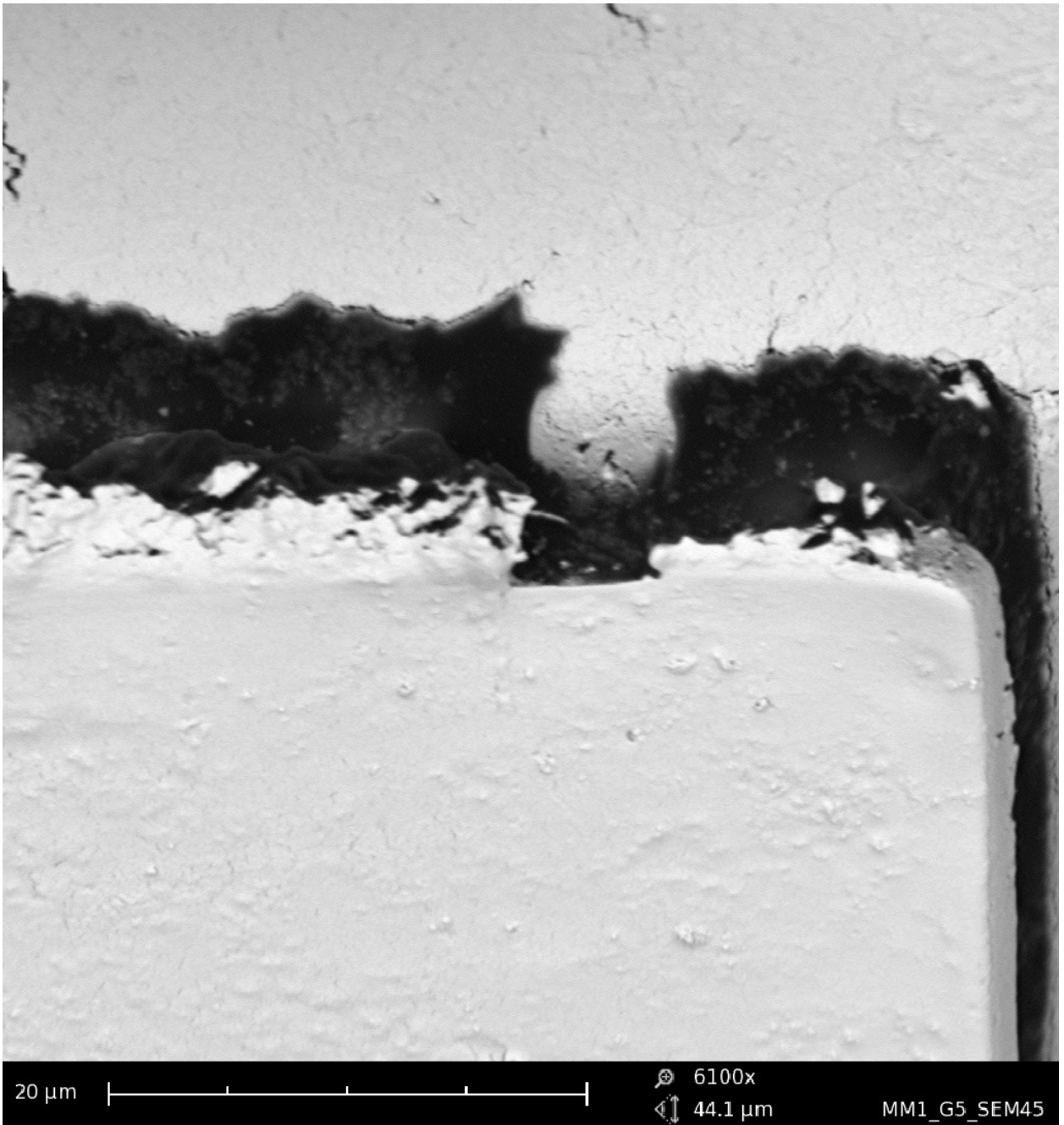


Figure 39: Close up of mould degradation

Now that the moulds have been produced and the microfluidic ports have been punched they are ready to be combined with the PolyMUMPs chips.

## CHAPTER 5: MOULD INTEGRATION

### 5.1. PRE-PLACEMENT STEPS

Before the moulds are placed and adhered to the PolyMUMPs chip the mould quality must be ensured. Slight changes in mould production temperature, or press time can significantly affect the quality of the mould. Two of the greatest negative effects which can occur are: air bubbles trapped in the mould (which reduce quality and optical performance), and incomplete mould formation. In the latter case if the temperature is too low or the press time is too short the mould may not be fully formed. Most times this means that the Kraton material has not sufficiently filled the negative which leads to misshapen mould walls or uneven mould channel depths. Mould quality is judged optically by the user. Both air bubbles and incomplete mould formation are easily identified post-production. Once the mould quality has been verified it is ready for placement onto the PolyMUMPs chip.

### 5.2. PLACEMENT METHOD

In order to accurately place the moulds onto the PolyMUMPs chip a pneumatic placement system was implemented. This system consisted of a 1.27mm suction tip attached to a 3 degree-of-freedom microactuator. The suction tip is then connected via medical tubing to a 3 way valve with a 10 mL BD syringe on one end, and open on the other. This system allowed for both positive and negative pressure to be applied at the

suction tip to adhere and release the mould. Figure 40 shows the system with a mould attached.

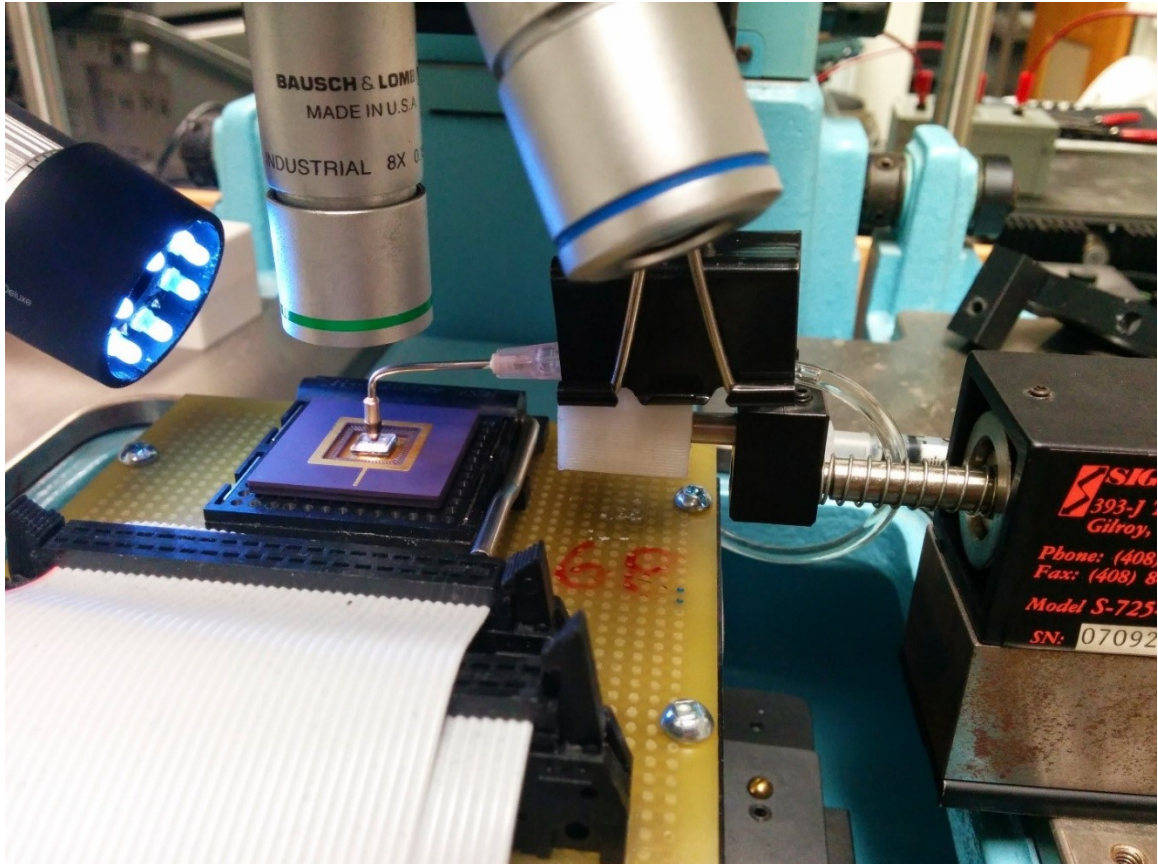


Figure 40: Mould placement system

To use the system the mould is placed on the edge of the PolyMUMPs chip. The suction tip is then moved into place and a small negative pressure of 0.2 bar is applied to adhere the mould. From here the suction tip with mould is moved onto the PolyMUMPs chip and lowered into position. The 3 degrees of freedom provided by the actuator in addition to rotation provided by the base of the PolyMUMPs chip holder allows for accurate placement of the moulds onto the chip.

To aid with accurate placement cross shaped placement markers were implemented into the mould design (see Figure 41).

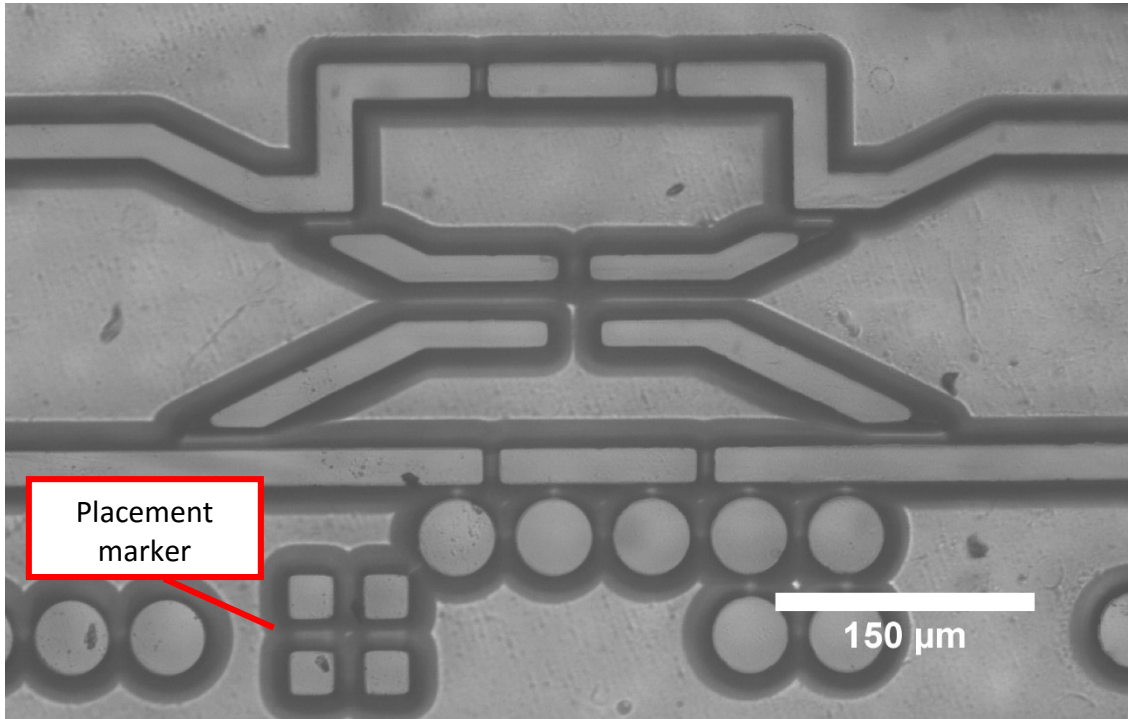


Figure 41: Mould with cruciform placement markers shown

These cross designs match metal crosses designed into the 'MM1' chip design (Figure 42 & Figure 43). Aligning these two markers ensures accurate mould placement. Placement accuracies were tested by measuring the x, y, and angular misalignment of the cross structures over the course of 5 placement trials. The results of the trials are outlined in Table 1.

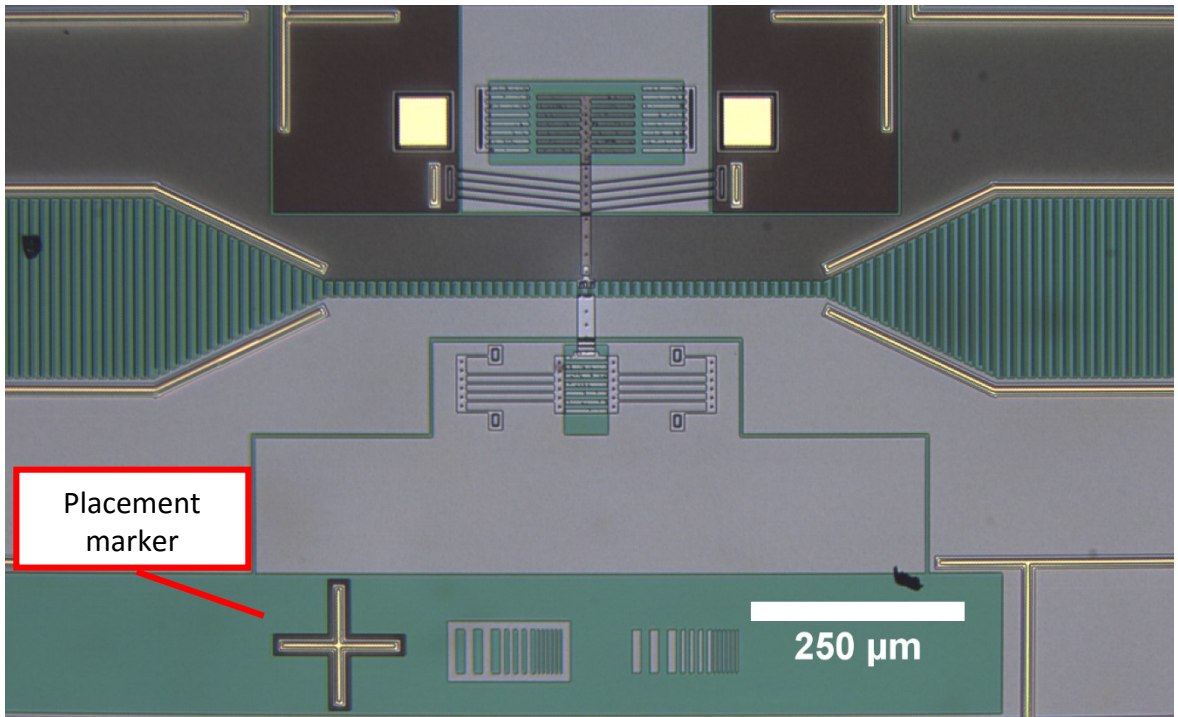


Figure 42: MM1 chip with placement marker labeled

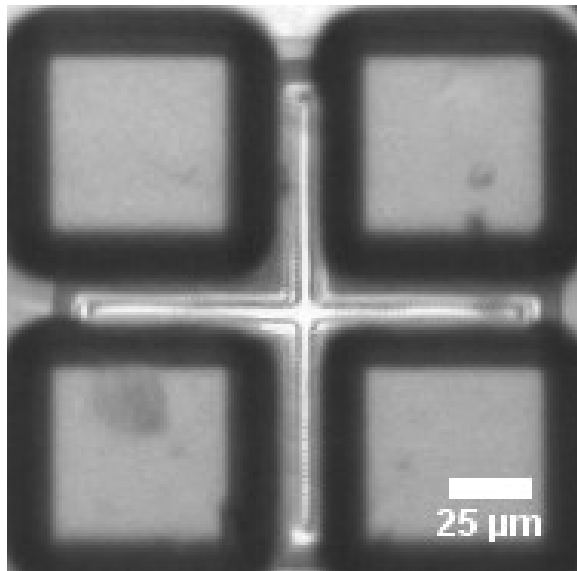


Figure 43: Properly aligned placement markers

Trial #	X-Misalignment	Y-Misalignment	Angular Accuracy
1	7.0 $\mu\text{m}$	0.0 $\mu\text{m}$	0.4°
2	0.0 $\mu\text{m}$	0.0 $\mu\text{m}$	0.0°
3	4.0 $\mu\text{m}$	4.5 $\mu\text{m}$	0.8°
4	2.4 $\mu\text{m}$	10.0 $\mu\text{m}$	0.4°
5	0.1 $\mu\text{m}$	0.6 $\mu\text{m}$	0.0°
<b>Average</b>	<b>2.7 <math>\pm</math> 2.9 <math>\mu\text{m}</math></b>	<b>3.0 <math>\pm</math> 4.3 <math>\mu\text{m}</math></b>	<b>0.3 <math>\pm</math> 0.3°</b>

Table 1: Mould placement accuracy results

This leads to the calculation of the net XY misalignment:

$$XY_{acc} = \sqrt{X_{acc}^2 + Y_{acc}^2} \quad \{28\}$$

$$XY_{acc} = \sqrt{(2.7\mu\text{m})^2 + (3.0\mu\text{m})^2} = 4.0\mu\text{m} \quad \{29\}$$

Once the mould has been placed a SEM stub covered in Teflon is used to adhere the mould to the PolyMUMPs chip. The mould is adhered by simply pressing the SEM stub gently against the mould. Figure 45 shows a placed mould before and after being pressed by the SEM stub. Note the darkened mould edges which show the mould properly adhered to the substrate.



Figure 44: SEM stub covered in Teflon (stub is 13 mm diameter)

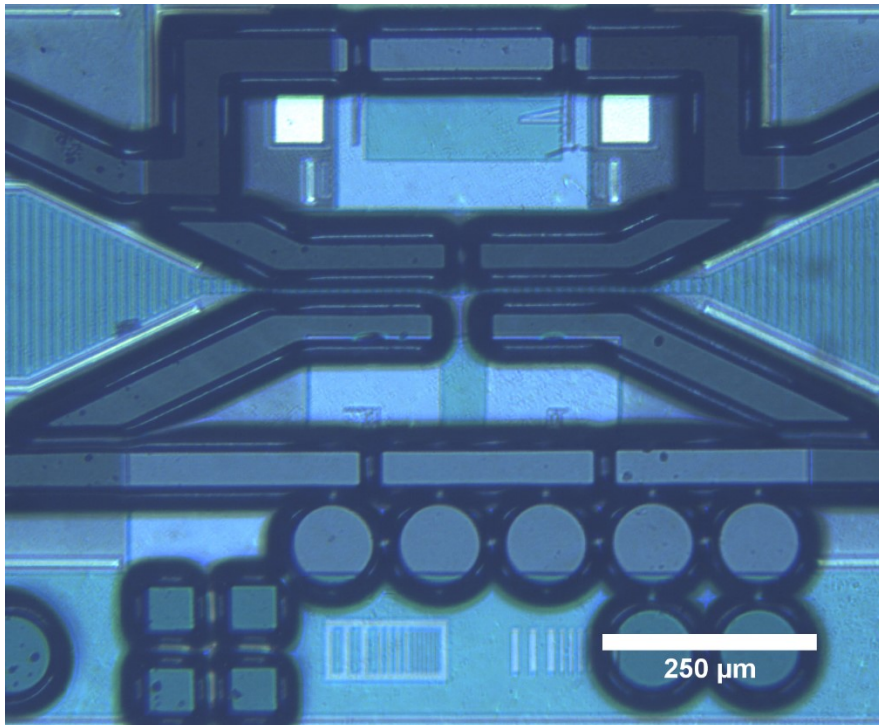
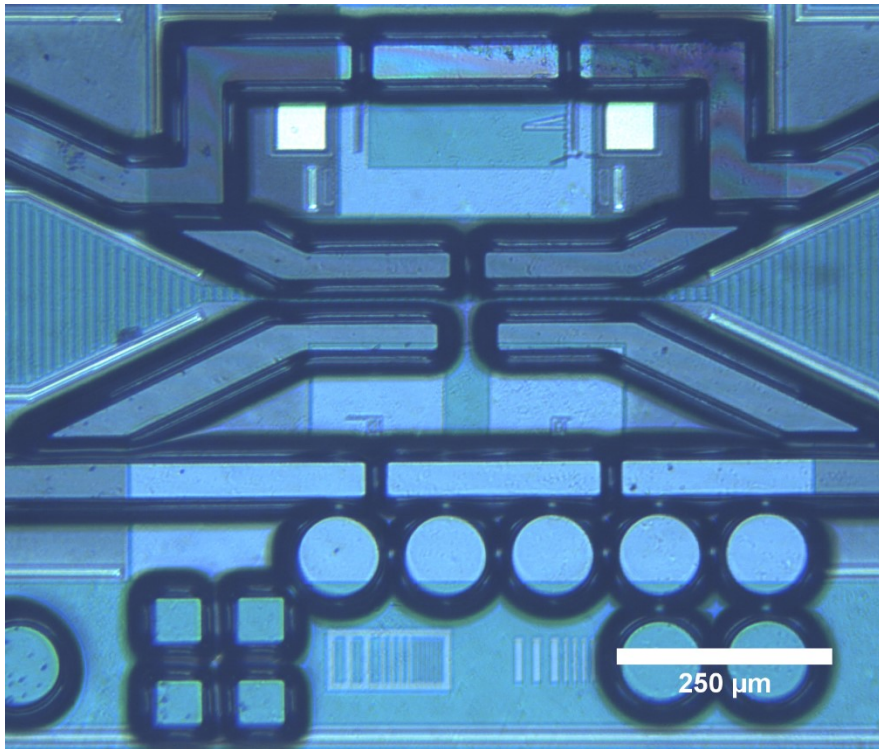


Figure 45: Placed mould top: pre-pressing bottom: post-pressing (Note: actuators and back spring removed)

### 5.3. FILLING AND REMOVAL

Once a new mould has been properly placed and adhered as described above, the microfluidic channel is ready to be filled with the working fluid. To do this a drop of the working fluid is placed onto one of the ports and a negative suction ( $\sim 0.2$  bar) is applied at the other port. This suction pneumatically pulls the working fluid into the microchannel (Figure 46 & Figure 47).

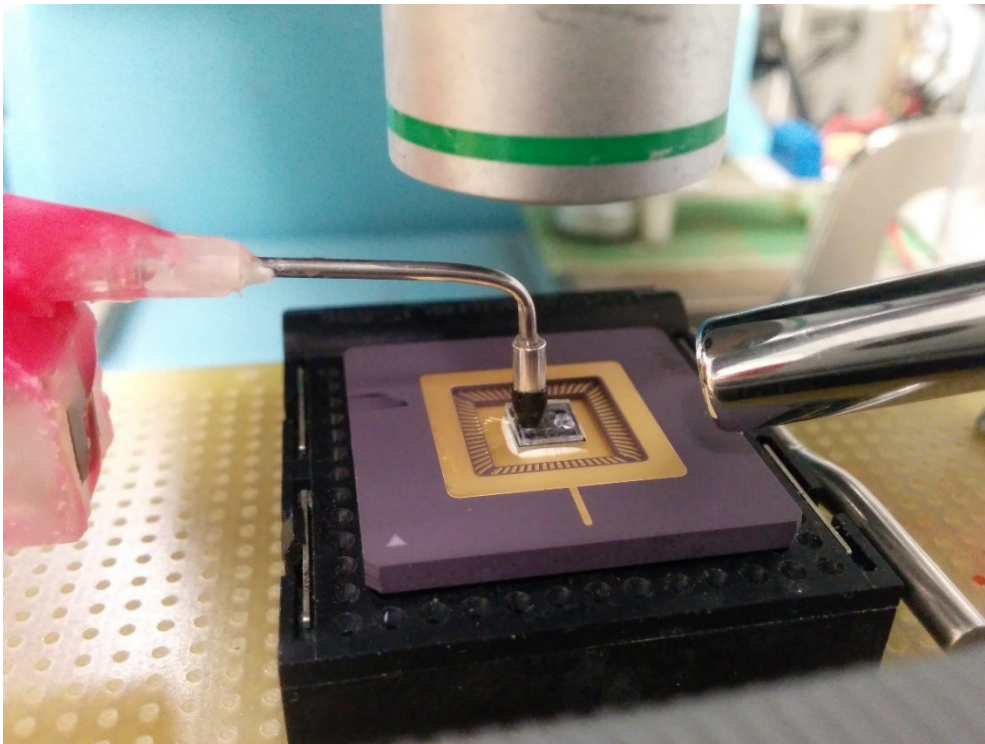


Figure 46: Close up of pumping setup

Figure 48 shows the process of filling of the microfluidic channel from the view of the microscope. On the left is the suction tip, on the right is the incoming fluid. Note the meniscus from 1-2-3-4 filling in.

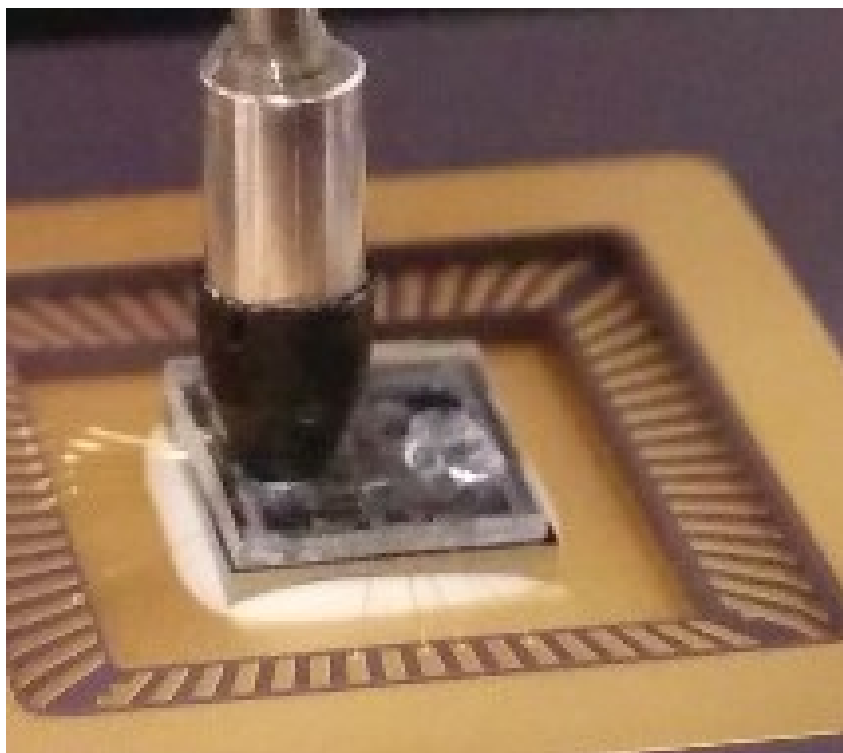


Figure 47: Close up of microfluidic channel filling (5x5 mm die)

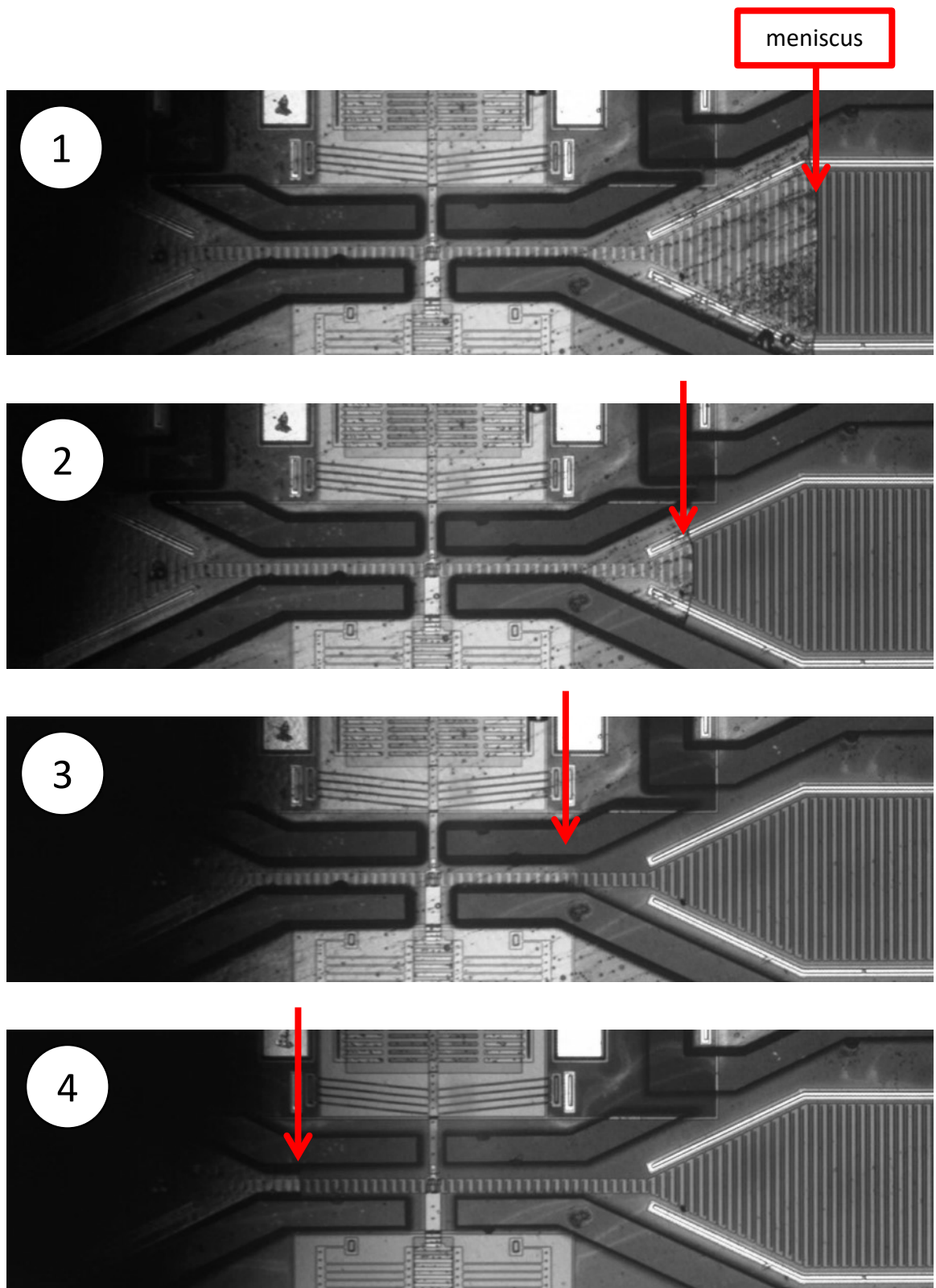


Figure 48: Process of microfluidic channel filling – suction on the left, note the meniscus moving from right to left

Another method used to fill the mould channels was to use a syringe pump. The same suction system outlined previously is connected to a Lucca Technologies GenieTouch™ syringe pump (Figure 49). The GenieTouch™ syringe pump can accept syringe volumes from 0.5  $\mu\text{L}$  to 60 mL, flow rates from 0.0001  $\mu\text{l/hr}$  to 220.82 ml/min, and has a linear step resolution of  $\pm 0.2$  mm. A 60 mL syringe is then used in the syringe pump to apply negative pressure to pull the fluid into the microfluidic channels.



Figure 49: Pneumatic pumping setup with GenieTouch™ syringe pump

Not all fluids however are the same in regards to filling and maintaining a seal within the mould channels. In addition to sorbitol; ethanol, distilled water, filtered sea water, and Phosphate-Buffered-Saline (PBS) were tested as working fluids. The only fluid to leak to the point of being unusable was ethanol (Figure 50 shows fluid leaking from the mould

channels), hence its selection as a tool to remove moulds post-use (in addition to its low evaporation temperature, details of mould removal are outlined following). The other working fluids did not show any signs of leaking under normal circumstances, however if the moulds were cut too large the edges would touch the bond pad wires causing the edges to lift, which would cause leaking on that side. Sorbitol was selected as the working fluid of choice as it is the only fluid which both worked for dielectrophoretic flow in addition to being biocompatible with yeast cells for future work.

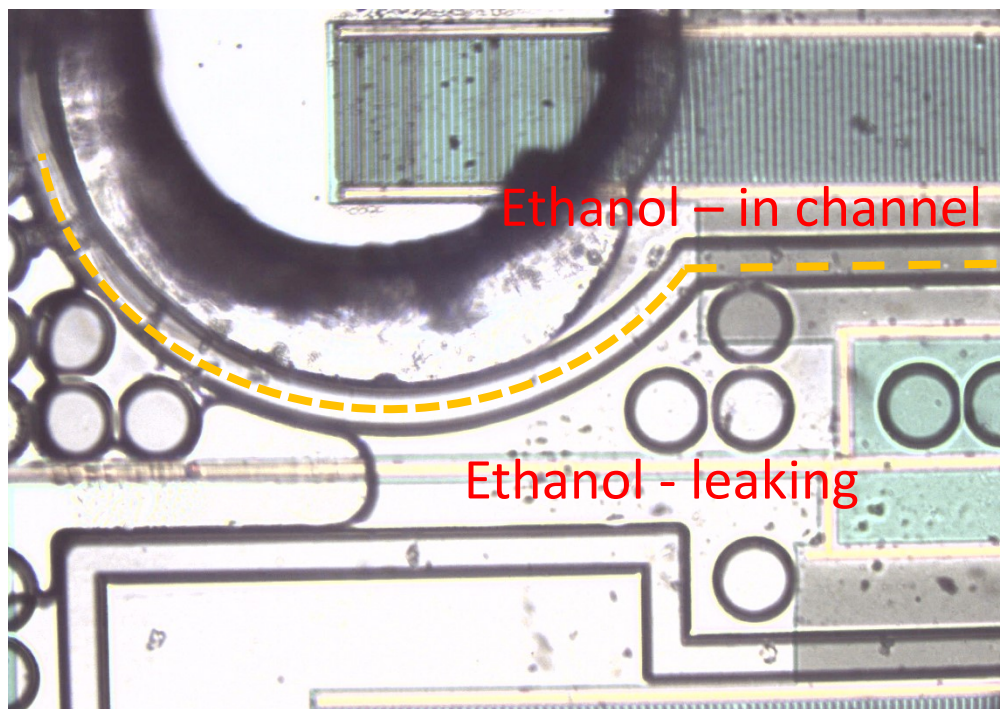


Figure 50: Mould leaking (working fluid ethanol)

Once the mould has been used, it can be removed from the chip in order to remove the chip from a microfluidic environment. In order to do this a similar method to placement is used. First ethanol is placed onto the PolyMUMPs package area. The ethanol seeps between the mould and the chip, which reduces adhesion between the two. After this

the same suction tip system used for placement is moved into place. A small amount of negative pressure ( $\sim 0.2$  bar) is then used again in order to remove the mould from the chip. The PolyMUMPS chip is reusable, but the moulds are not, however they are easy to remake for additional uses. Figure 51 shows the PolyMUMPS package submerged in ethanol for mould removal.

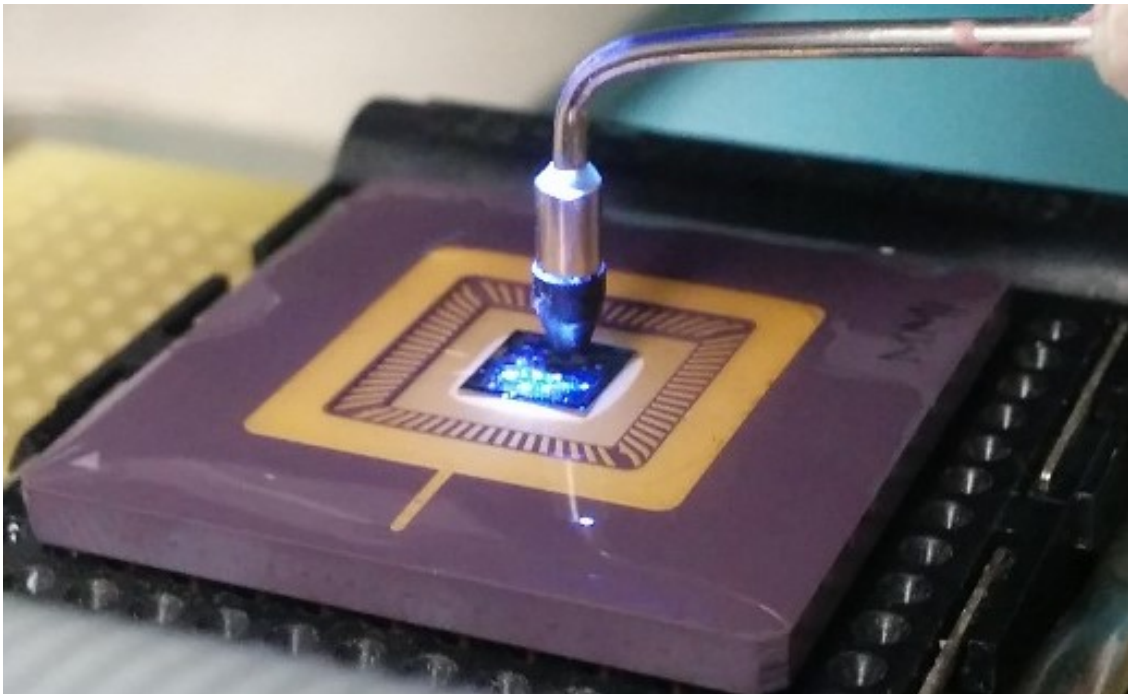


Figure 51: Ethanol flooding the placed mould to remove from the die via suction tip

#### 5.4. MOULD REDESIGN

Initially moulds were designed such that the actuator and back spring were both “dry”: isolated from the working fluid. This would provide a greater maximum actuator displacement as they wouldn’t be in contact with the working fluid. However it was found that the seal gap opening between the working fluid and the actuator allowed

fluid from entering the actuator area over time (Figure 52 - Top). This effect was catastrophic when the actuator was in use. The temperature increase of the chevron thermal actuator caused the working fluid at the fluid-air interface to boil. This caused significant blurring of any images of the actuator due to condensation of the fluid on the mould surface (shown in Figure 52 – labeled 'A'). King et al [34] showed that a FFT optical displacement measurement technique is robust to blurring, however that is only in the case of blurring due to misaligned focal planes, or in plane vibration. The blurring from the condensation was inconsistent and in some cases droplets would completely obstruct view.

Due to this, the mould actuator and back spring areas were redesigned to encourage fluid flow to the actuator and back spring during the filling process (Figure 52 - Bottom). In addition to the bypass channels, ports were also added to the actuator and back spring areas in the moulds (see Figure 53 – '3'). These allow for easier filling of the actuator and back spring areas by allowing air to escape during filling.

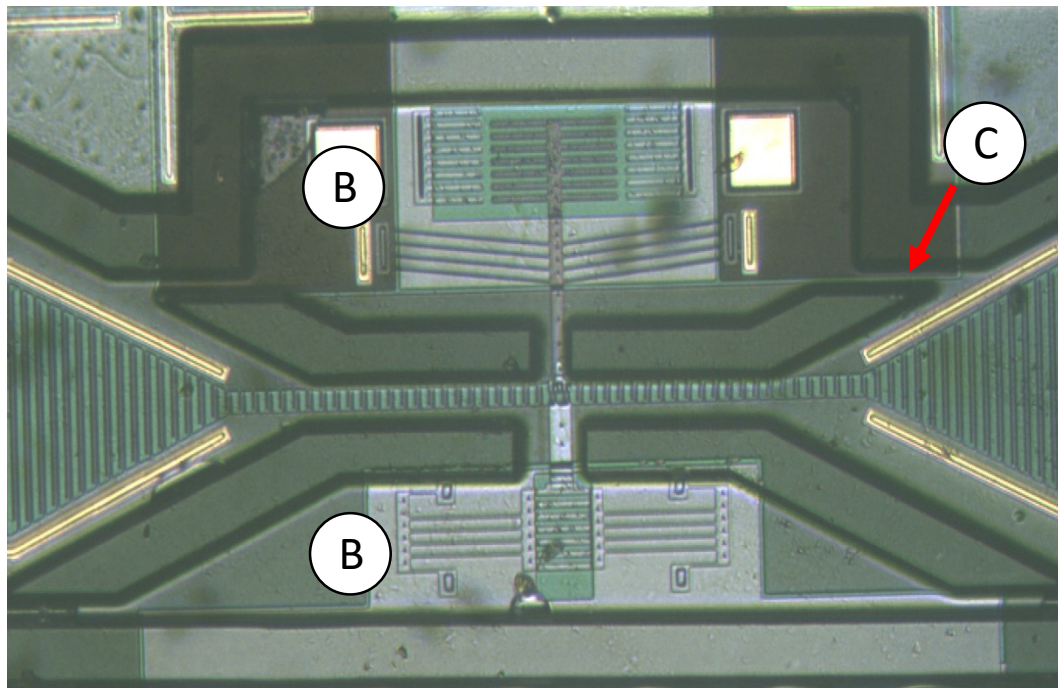
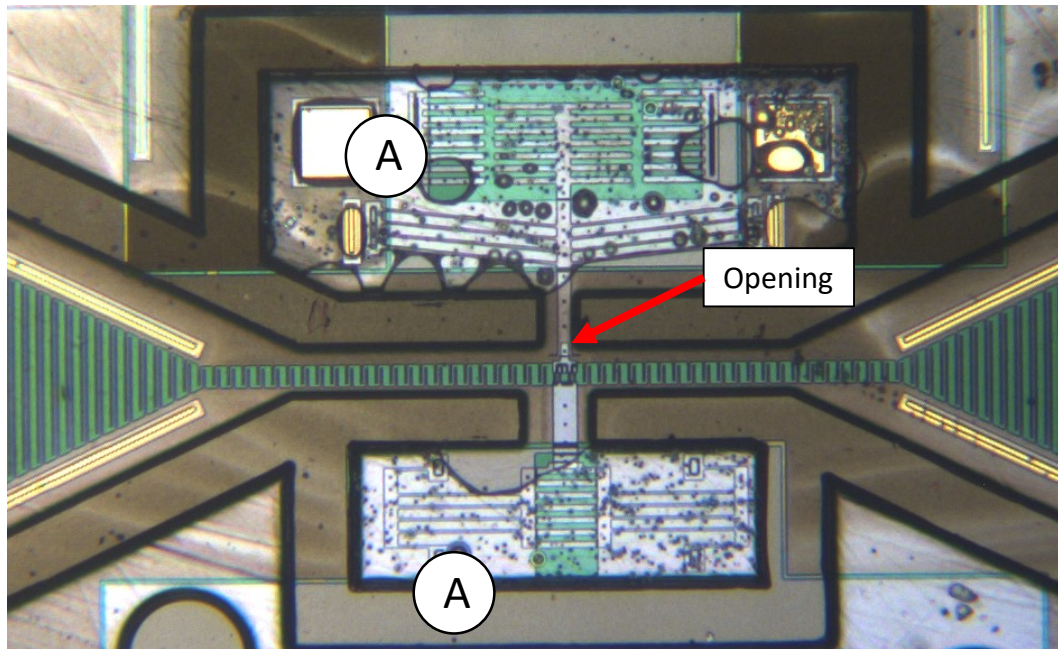


Figure 52: Old Mould Design (Top), New Mould Design (Bottom)

A – Actuator and back spring areas partially filled with water droplets

B – Actuator and back spring fully filled with water due to bypass channels 'C'

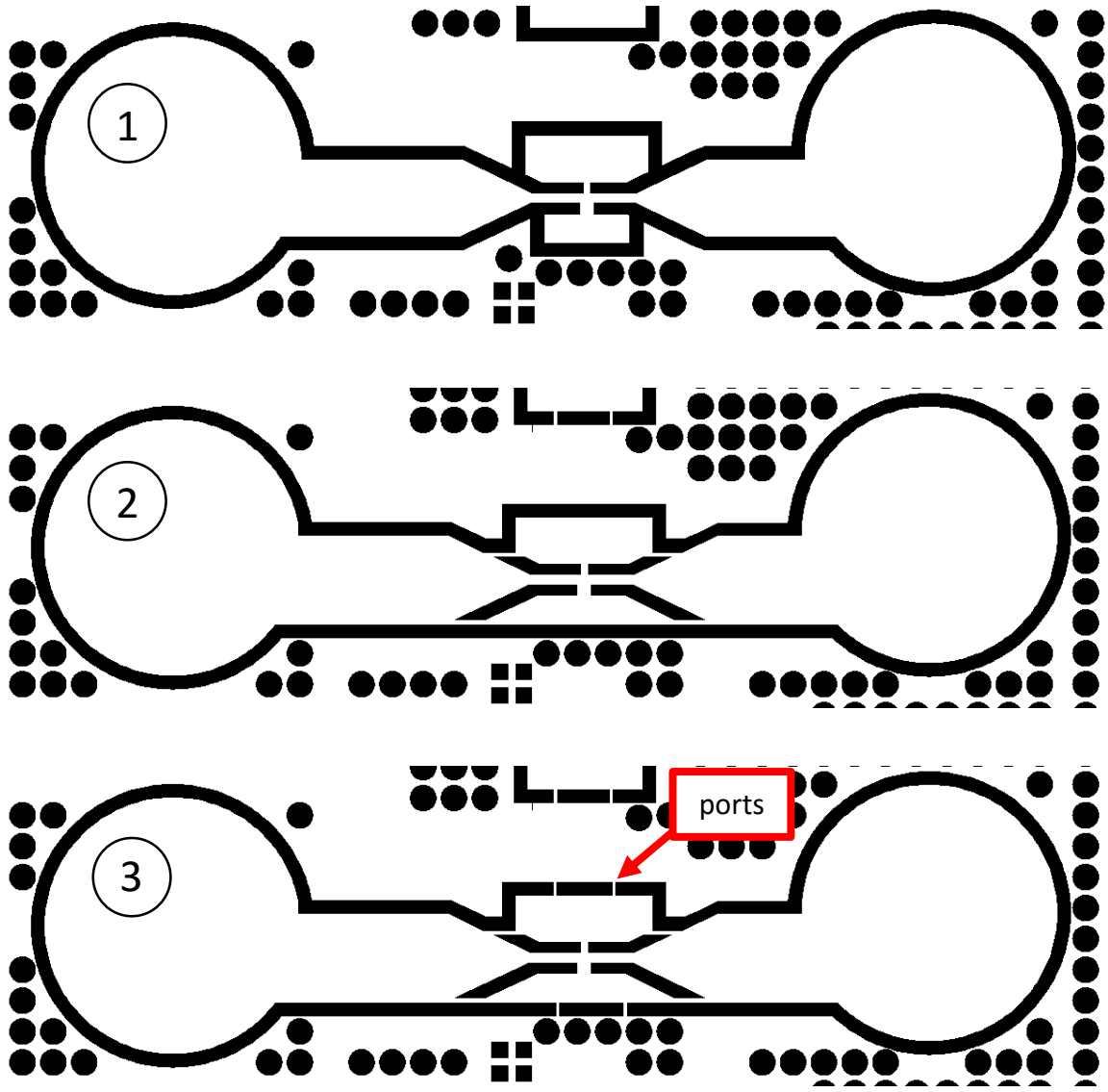


Figure 53: Mould redesign: 1) original design, 2) new design, 3) new design with ports in actuator and back spring area

As shown in Figure 52 'B', the mould redesign successfully fixed the issue of partial actuator and back spring area filling. The complete filling removes the issue of water boiling/condensation while still allowing thermal actuator function. This comes at a cost of actuator performance, as will be shown in the following chapter, the performance of the chevron actuators in water is ~5% of the performance in air.

Now that we have the bypass channels and are able to test underwater the effect of the mould on thermal actuator performance could be tested. In addition to this the use with pneumatic and dielectrophoretic pumping of polystyrene spheres could be tested.

## CHAPTER 6: RESULTS

### 6.1. CHEVRON ACTUATORS IN MOULDS

In order to test the effect of the mould on the actuator the actuators were first tested in both air and water out of the moulds.

#### 6.1.1. OPEN (AIR/WATER)

The chevron thermal actuators were tested first in both air and water without the mould. Their performance is outlined in Figure 54 and Figure 55. Note the different scale of the y-axis in each figure.

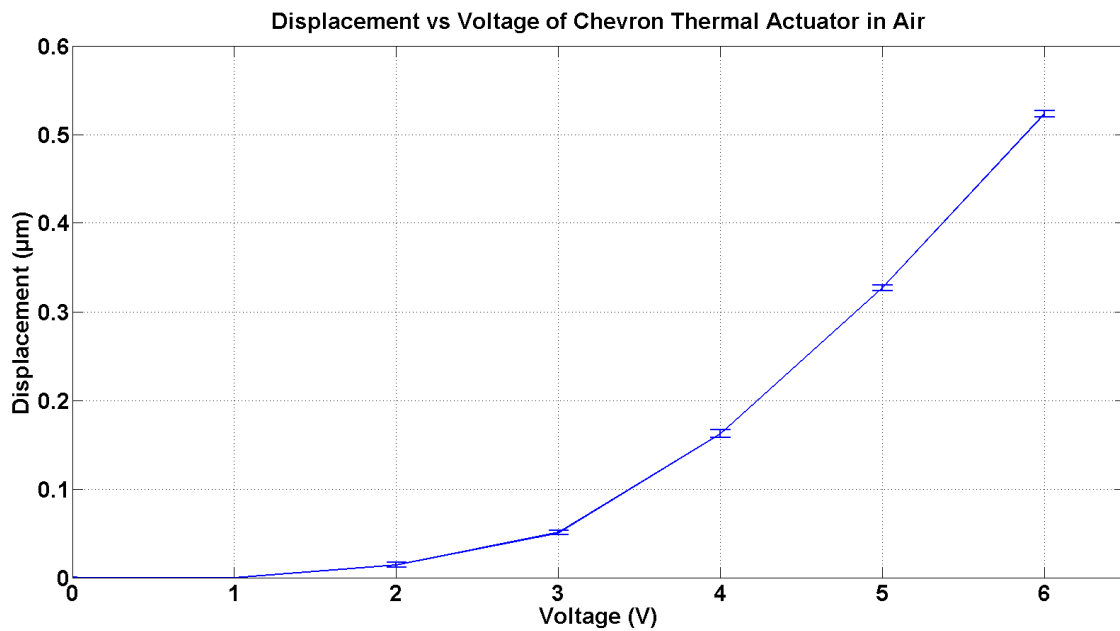


Figure 54: Measured displacement of chevron thermal actuator in air - no mould

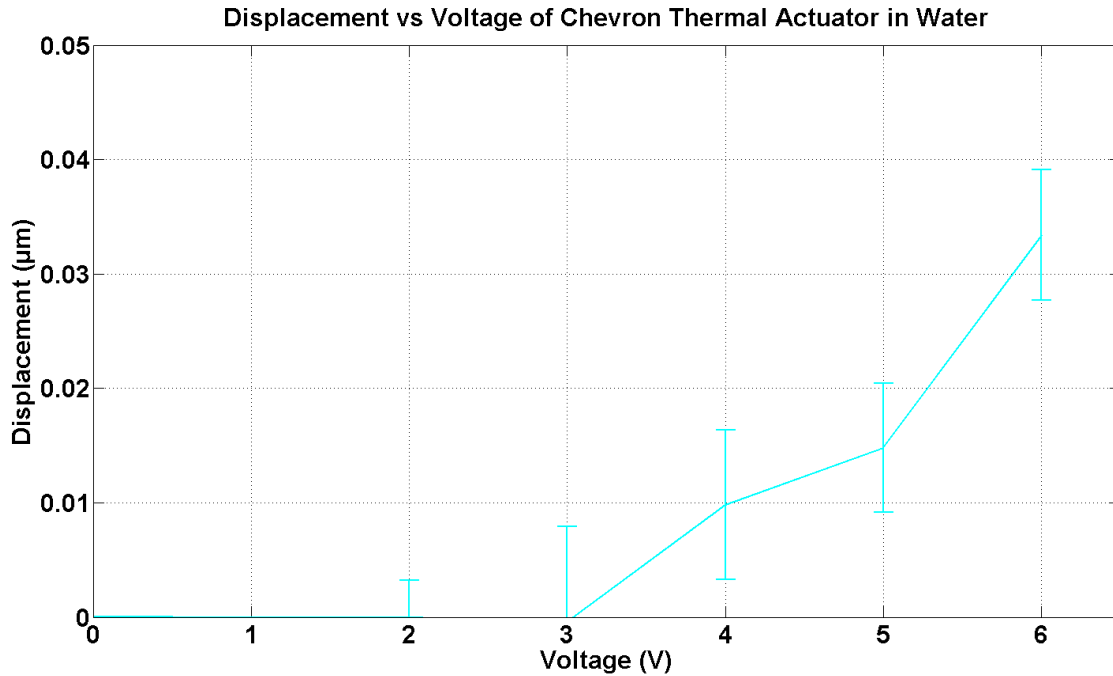


Figure 55: Measured displacement of chevron thermal actuator in water - no mould

Both of these curves closely follow the expected relationship; that displacement is proportional to the square of the applied voltage, and that the performance of the thermal actuator in water is approximately 5% of the performance in air.

### 6.1.2. CLOSED (AIR/WATER)

Next the performance of the chevron thermal actuator was testing in the mould. The actuator was tested using the same parameters as the tests out of the mould: 1MHz signal from 1-6 Vpp in both air as well as in water. The results from these tests are shown below in Figure 56 and Figure 57. Note the different scales for the y-axis for each figure.

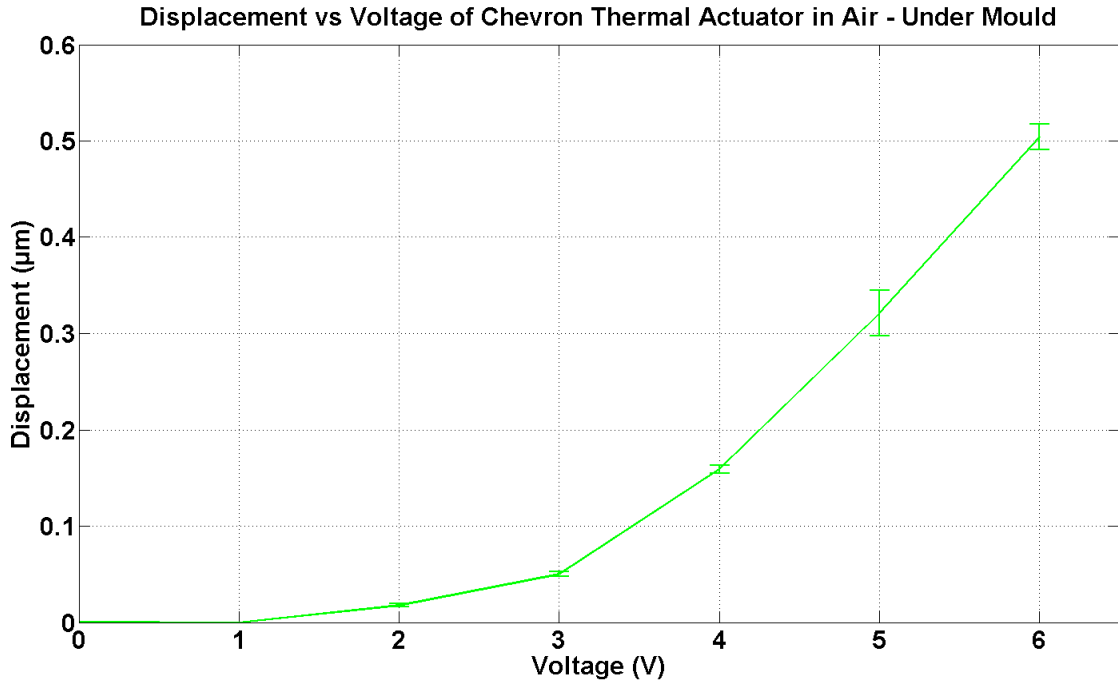


Figure 56: Measured displacement vs Voltage thermal actuator in air – under mould

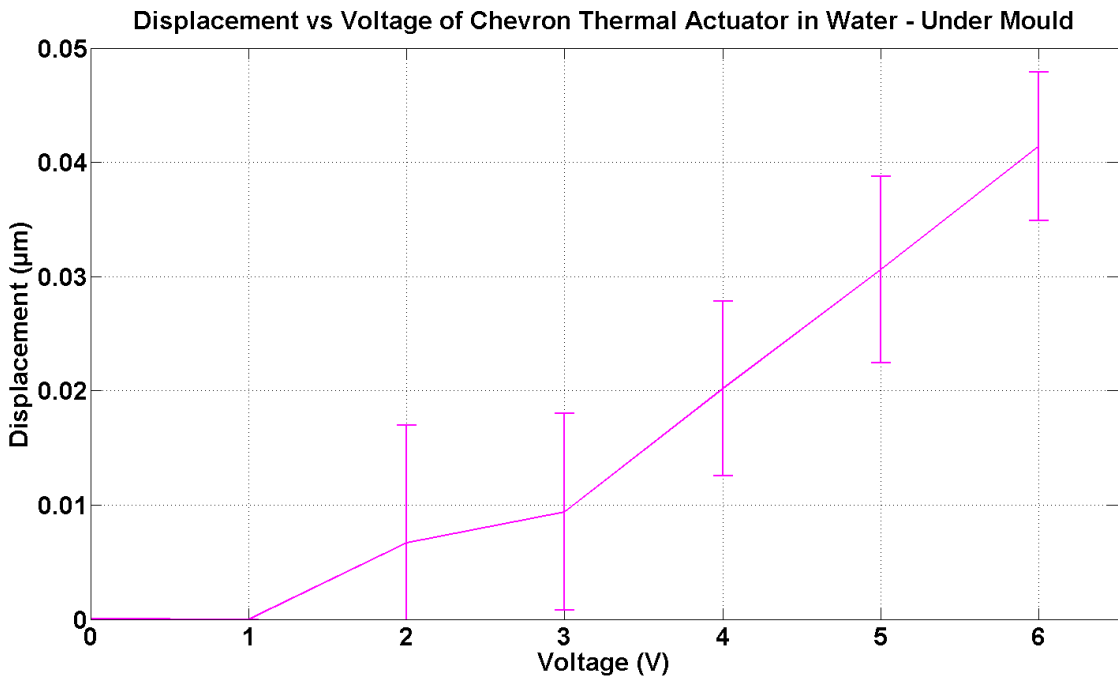


Figure 57: Measured displacement vs Voltage thermal actuator in water – under mould

The plots show a very similar quadratic curve to the results outlined in section 2. Figure 58 directly compares the results of the open tests in air and water to the tests done in the mould both in air and water.

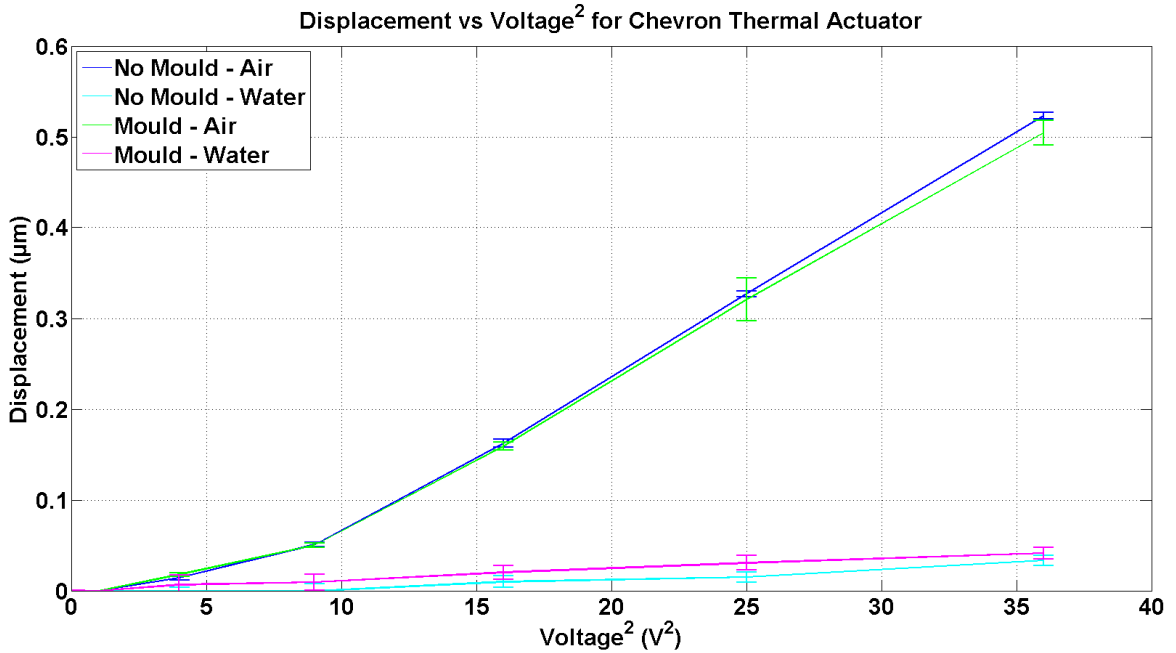


Figure 58: Measured displacement vs Voltage<sup>2</sup> for chevron actuator in air/water open & closed

The displacements for the chevron actuator in the mould are almost identical to the displacements outside the mould. The displacement in open air is slightly higher than that of the displacement in the mould in air. However the reverse is true for the displacement of the actuator when it is submersed in water in the mould.

Although the data for both the air and water compared to the same underwater are not identical, they are both within the margin of error of one another, suggesting that they

are statistically the same. From this it is clear that actuator performance is not significantly affected by the mould.

## 6.2. DEP RESULTS

Next the performance of dielectrophoresis was tested in both the open and closed configuration. Dielectrophoretic flow tests were done using a Keysight Technologies 33512B dual channel waveform generator. Two synchronized AC waveforms were sent directly to the electrode array from the waveform generator. Trials were done at a frequency of 1MHz and voltages ranging from 1-10 Vpp. The Phase shift between the two signals was set at 120°. Velocities were measured using an edge detection technique measuring the movement of the edge of the sphere over the course of a known segment of time with a measurement error of  $\pm 1.3\%$ .

### 6.2.1. OPEN

First trials were done on the open track (without moulds). Only the wide section of track was used for velocity trials as sphere movement stopped as the track width decreased to  $\sim 100\ \mu\text{m}$ . In the wide section of track the experimental velocity of a  $6\ \mu\text{m}$  polystyrene bead vs. the applied voltage is shown in Figure 59. As per the simulation the dielectrophoretic force should scale with the cube of the applied voltage. This means that the velocity of a particle under the effects of dielectrophoresis should scale with the cube voltage as well. However Stokes drag will also increase as particle velocity increases therefore it is not exactly a cubic relationship.

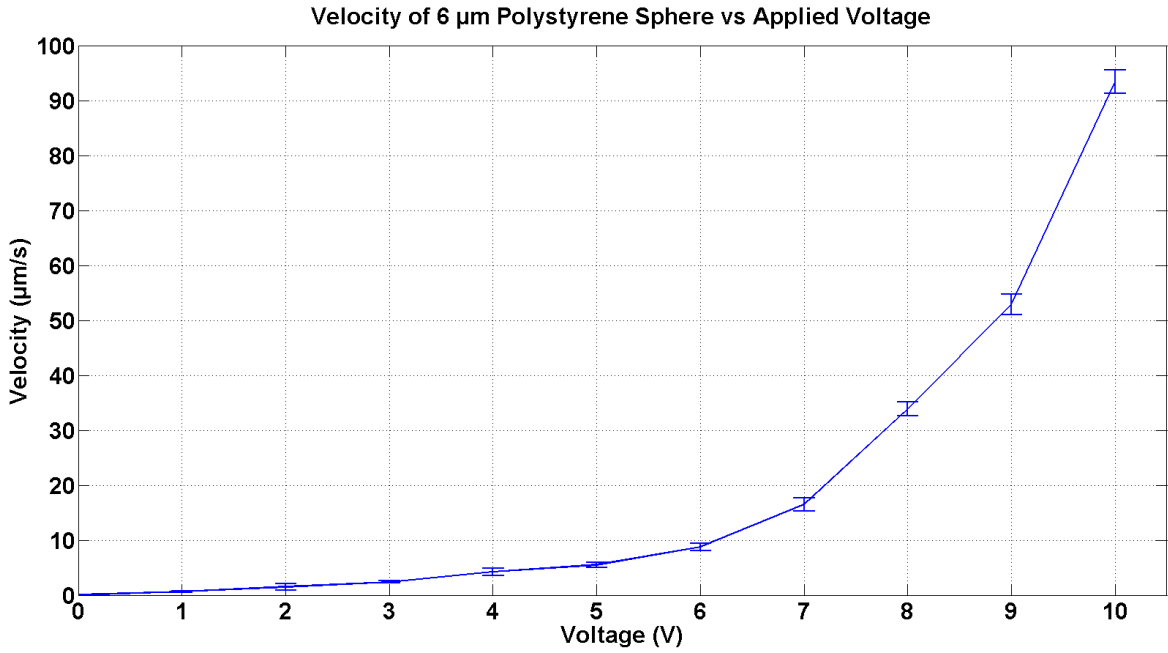


Figure 59: Measured DEP velocity vs voltage for wide section of track on MM1 – no mould

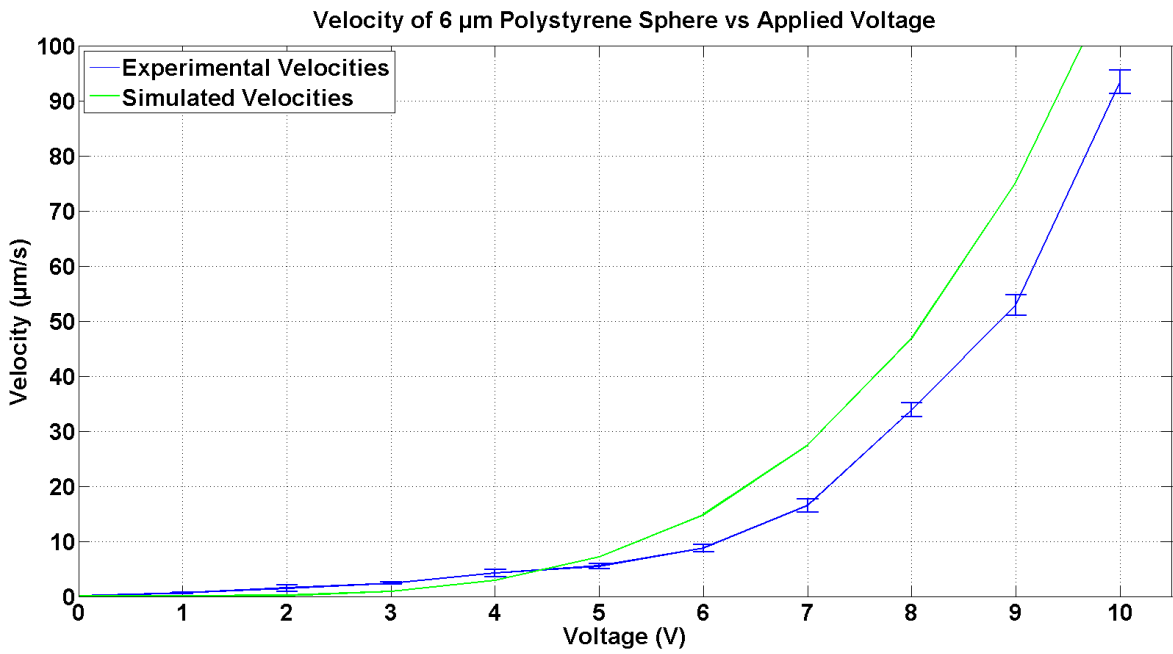


Figure 60: Open DEP velocities - experimental vs simulated

This curve agrees very closely with the simulated values, however it is slightly lower than those simulated. This may indicate that there is another force opposing motion, or that the numerical values for dynamic viscosity or the Clausius –Mosetti factor for the system may be different than the actual values.

### 6.2.2. CLOSED

Next dielectrophoretic flow was tested under the mould. Tests were run using the same parameters as out of the mould. Figure 61 shows the velocity of a 6  $\mu\text{m}$  polystyrene sphere vs applied voltage when enclosed in the mould microfluidic channel.

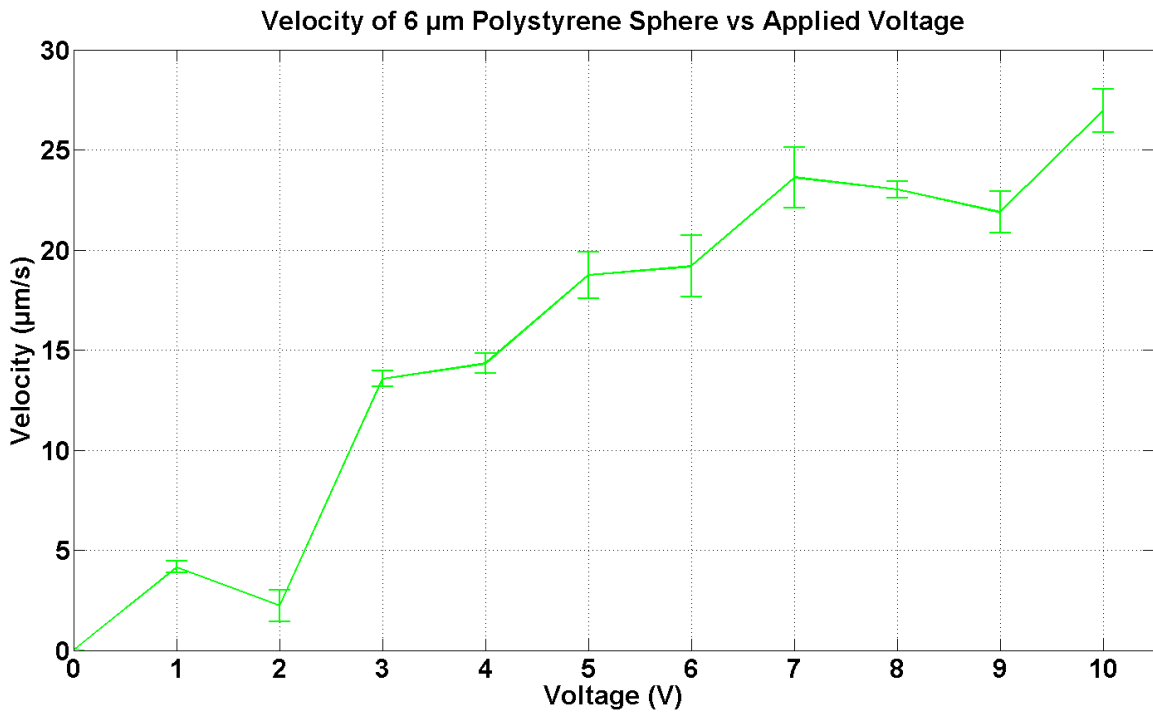


Figure 61: Measured DEP velocity vs voltage for wide section of track on MM1 (closed)

The curve is very noisy due to inconsistent flow in the mould, not due to inaccuracies provided by obtaining optical measurements under the mould surface. It is interesting

to note that while the velocity at the maximum voltage (10 Vpp) is less than 30% of that in the open configuration that there is larger sphere motion at lower voltages than that of the open configuration (compared in Figure 62).

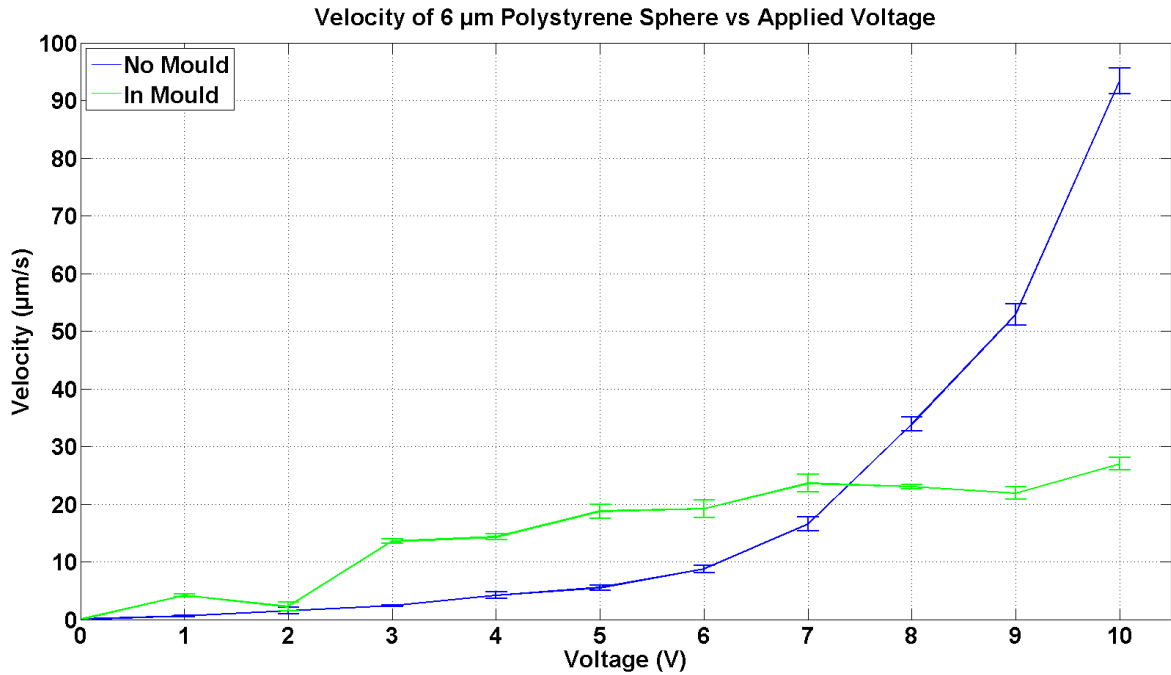


Figure 62: Comparison of 6 µm polystyrene sphere Measured DEP velocities no mould vs mould

From this it is apparent that the mould is changing the electric field which is being produced by the electrode array. In addition to the change in electrical field there could be a change in the drag effect experience by the particle due to the upper boundary of the mould as the sphere is 6 µm and the mould is 44 µm deep, therefore there is only a maximum gap of 38 µm between them.

One issue that occurred in the open configuration and was still apparent in the closed configuration is that the dielectrophoresis does not work in the narrow width DEP

electrode sections. Travelling wave dielectrophoretic flow theory and simulation always use tracks which are reasonably wide. This is due to the theory only being sound for an electrode of relative “infinite” length, that is to say that the width of the track is significantly longer than the size of the individual electrode, however this stops being the case when the track width reduces. In addition it was noted in the open trials that the polystyrene spheres would lift vertically at this portion of the track and continue to move, though significantly out of plane. The spheres would then move towards the track on the opposite side of the cell testing structure when the track width widened again (see Figure 63 for diagram).

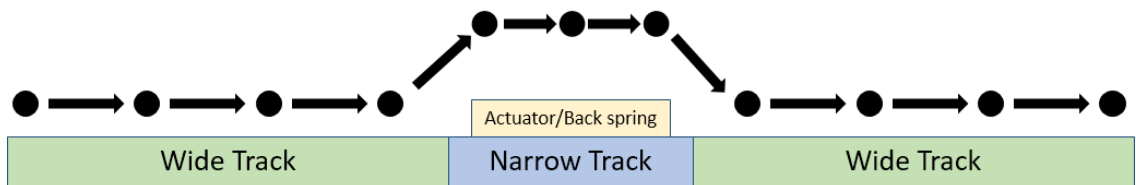


Figure 63: Diagram of sphere motion in open MM1 track

Although not fully known at this point, it is presumed that at this point in the track the repulsive dielectrophoretic force is increased significantly which forces the spheres upwards. From here a force known as AC electroosmosis may be causing the medium to flow, which would move the spheres at greater heights. It was hoped that this may force the spheres to move through the microfluidic channels however this was not the case. As there was a lack of movement in the narrow channel; dielectrophoretic pumping could not be the sole solution for controlled particle manipulation within the mould.

Due to this pneumatic pumping using the same syringe pump used for initially filling the microfluidic channels was selected as the next option. However dielectrophoresis is still useful as part of a system for controlled particle manipulation. Due to the nature of dielectrophoretic flow, microparticles are channeled towards the center of the electrode array. This natural effect allows for the proper alignment of the microparticle prior to pneumatic pumping. Not only does the effect align the particle with the gripper jaws, but it also entraps the sphere at the opening to the narrow channel section.

Figure 64 shows 6  $\mu\text{m}$  particles trapped at the wide/narrow interface.

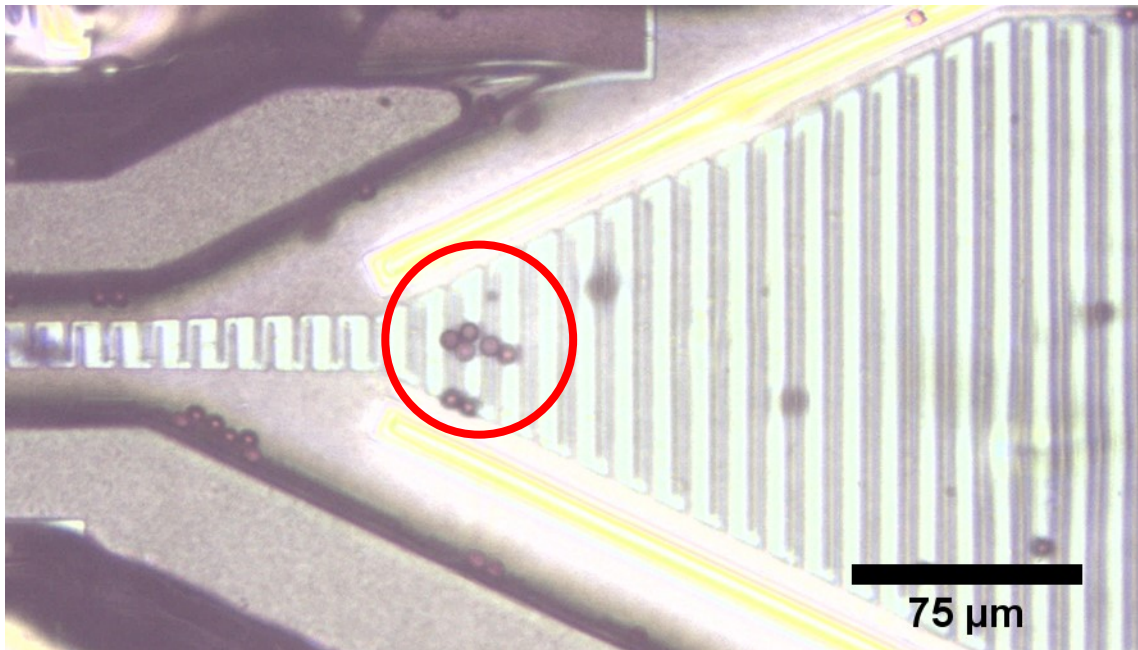


Figure 64: 6  $\mu\text{m}$  particles trapped using DEP

From here the current can be turned off and pneumatic pumping can be used to move the particles directly into position for testing.

### 6.3. PNEUMATIC PUMPING/SPHERE PLACEMENT

Due to the limitations of dielectrophoresis, specifically being unable to manipulate particles in the narrow channels, pneumatic pumping was used. Using the Lucca Technologies GenieTouch™ syringe pump connected in the same way as was used for initially filling the microfluidic channels (as shown in Figure 49). By using this method, controlled microparticle manipulation with velocities up to 30  $\mu\text{m/s}$  was achieved.

With this method the polystyrene spheres were accurately placed into the jaws of the cell gripper with an accuracy of  $\pm 3.6 \mu\text{m}$ . Figure 65 shows an image of the microparticles being moved towards the jaws. The micro-sphere motion is easy to discern when the particles are moving such as in a recorded movie or when ‘flicking’ back and forth between images, but it is less clear when examining static images as shown below.

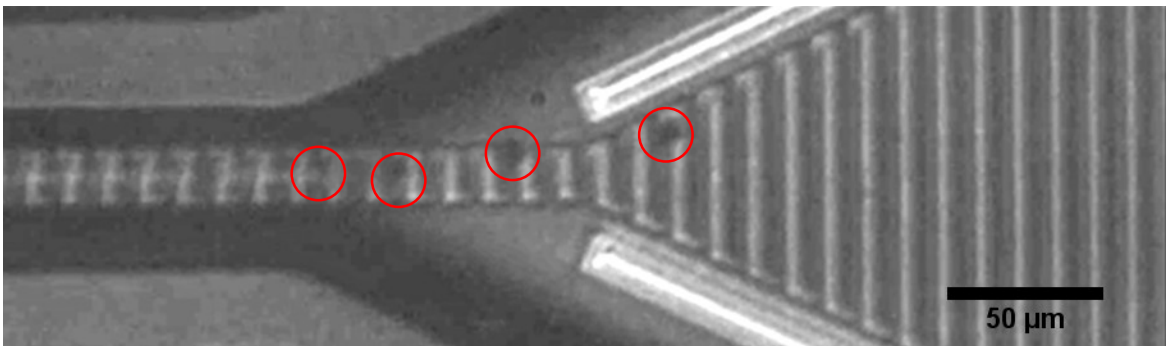
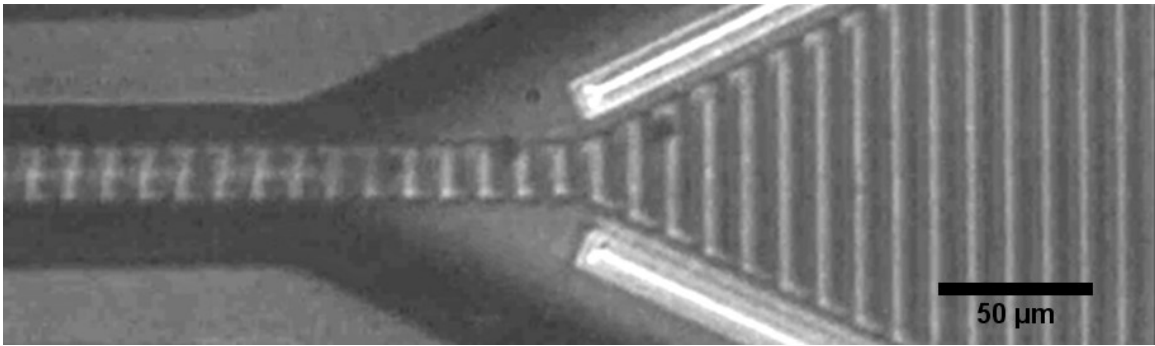


Figure 65: Superimposition of 4 images of 6  $\mu\text{m}$  spheres being moved towards the actuator gripper. Moving from right to left, spheres circled in lower figure for clarity

Figure 66 shows an enhanced image of the microparticles being accurately moved into position in the actuator jaws. Note that image enhancement was required as images near the jaws are very dim and difficult to discern. This is mostly due to an imperfect optical setup necessitated by the suction tip used for pneumatic pumping which interferes with the use of the longer high magnification microscope lenses. Instead a camera lens doubler was used immediately before the camera along with a shorter low magnification microscope lens to obtain a large magnification from a large standoff distance. In addition the suction tip causes shadowing in the images as it impedes a portion of the microscopes light source.

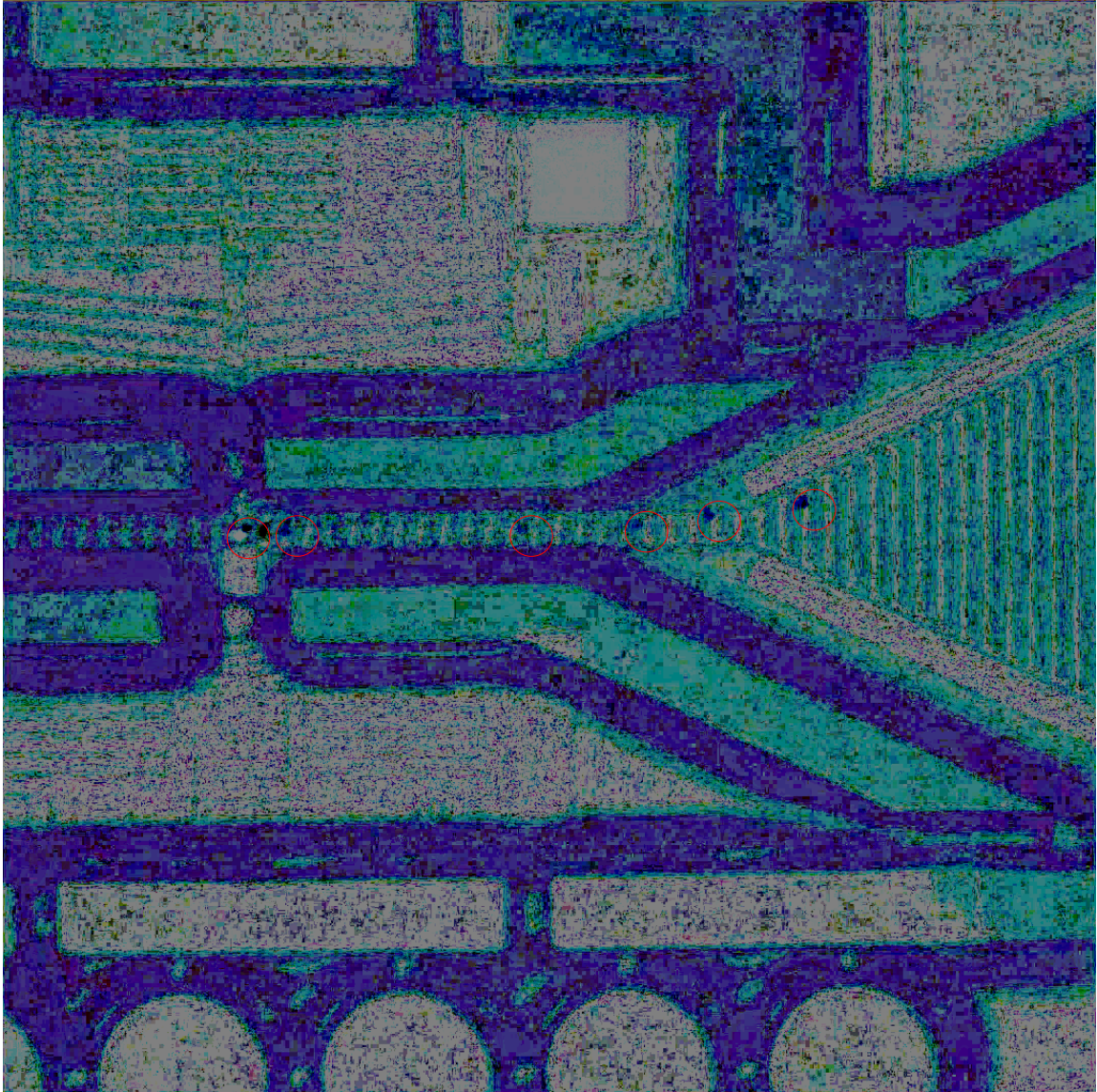


Figure 66: Image enhancement of time steps of 6  $\mu\text{m}$  polystyrene sphere pneumatically placed into actuator jaws. Moving from right to left, spheres circled for clarity.

Figure 67 shows an image enhanced close up of the jaws with the sphere outlined by a circle. The references 'a1' and 'a2' correspond to the distance from the left and right edges of the jaw line to the left and right edges of the polystyrene sphere respectively.

Thus the placement accuracy was 3.6  $\mu\text{m}$ .

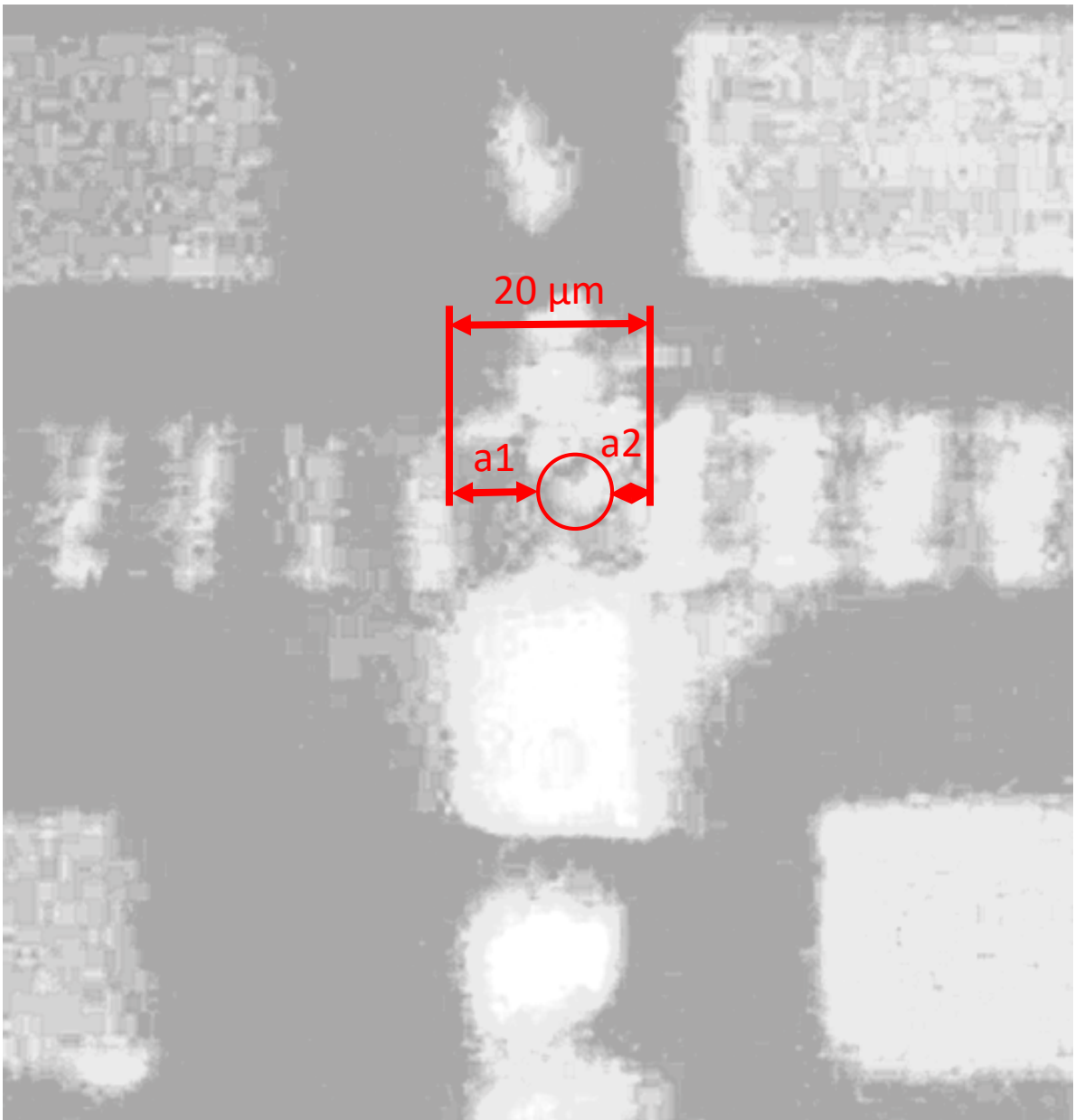


Figure 67: Close up of jaw placed sphere  $a1 = 10.6 \mu\text{m}$ ,  $a2 = 3.4 \mu\text{m}$

## CHAPTER 7: CONCLUSIONS

This paper explored the use of reversibly bonded polymer moulds, dielectrophoresis, and PolyMUMPS based thermal actuators for lab-on-chip MEMS. Moulds were produced with consistent results. Moulds were placed with a lateral accuracy of  $4.0\ \mu\text{m}$  and an angular accuracy of  $0.3^\circ$ . Dielectrophoretic flow as a method of controlled microparticle manipulation was explored with results quantified for both the open (no-mould) and closed (within the mould microfluidic channels) configurations. The open configuration results were compared to results produced via MATLAB simulation, and shown to closely agree. Due to the limitations of dielectrophoretic not working in the narrow lengths of the electrode array pneumatic pumping was utilized instead for microparticle placement into the jaws of the cell squeezing device. Finally the polystyrene microspheres were accurately placed in the jaws of the cell squeezing device with an accuracy of  $\pm 3.6\ \mu\text{m}$ , while the mould was placed.

### 7.1. CONTRIBUTION

This work shows a novel approach for future work in the area of MEMS lab-on-chip cell testing. Kraton polymer reversibly bonded gecko inspired moulds have not previously been used as a method for producing microfluidic channels on MEMS devices. The combination of dielectrophoretic pumping, pneumatic pumping, polymer moulds, and PolyMUMPS based cell testing devices have not previously been combined in order to form a full lab-on-chip system.

## 7.2. FUTURE WORK

Future work would involve a redesign of the electrode array used on the chip used in the reported research. The narrow section of the DEP electrode array prevented dielectrophoretic flow near the cell squeezing device. If the electrode array were redesigned, it should not taper fully down to the narrow 20  $\mu\text{m}$  section, but be left with a wider narrow section (100  $\mu\text{m}$  works, a bit smaller may work as well). Also, the narrow section should be shorter. This would hopefully allow for travelling wave dielectrophoresis to be used to move the particles directly into the cell squeezing device instead of relying on an external pneumatic pumping system. Although this method would still require a system to initially fill the mould channels, a simple syringe with a suction tip would be suitable.

In addition to a redesign of the electrode array, future work would involve the testing of biological cells within the microfluidic channels. Though the work was intended for future use with biological samples, polystyrene beads were selected as they are much easier to work with, and this work is intended as a prototype.

Since the start of this work and the design of the chip the cell squeezing devices' jaws have had a redesign to allow for cells of different sizes to be tested without requiring a different squeezing device with a different jaw width. This design has a stepped jaw to accommodate cells of different sizes. Future work would potentially involve integrating this jaw design to the device.

## REFERENCES

- [1] G. Y. Lee and C. T. Kim, "Biomechanics approaches to studying human diseases," *TRENDS in Biotechnology*, vol. 25, no. 3, pp. 111-118, 2007.
- [2] W. A. Lam, M. J. Rosenbluth and D. A. Fletcher, "Chemotherapy exposure increases leukemia cell stiffness," *Blood*, vol. 109, no. 8, pp. 3505-3508, 2007.
- [3] S. Suresh, J. Spatz, J. Mills, A. Micoulet, M. Dao, C. Lim, M. Beil and T. Seufferlein, "Connections between single-cell biomechanics and human disease states: gastrointestinal cancer and malaria," *Acta Biomaterialia*, vol. 1, pp. 15-30, 2005.
- [4] R. Schwatz, S. Warnat, T. Hubbard and M. Kujath, "MEMS DEVICE FOR THE DETERMINATION OF CELL STIFFNESS," in *Cancam*, Saskatoon, 2013.
- [5] R. Bogue, "MEMS sensors: past, present and future," *Sensor Review*, vol. 27, no. 1, pp. 7-13, 2007.
- [6] S. Łuczak, W. Oleksiuk and M. Bodnicki, "Sensing Tilt With MEMS Accelerometers," *IEEE Sensors Journal*, vol. 6, no. 6, pp. 1669-1675, 2006.
- [7] H. Xie and G. K. Fedder, "Fabrication, Characterization, and Analysis of a DRIE CMOS-MEMS Gyroscope," *IEEE Sensors Journal*, vol. 3, no. 5, pp. 622-631, 2003.

- [8] W. P. Eaton and J. H. Smith, "Micromachined pressure sensors: review and recent developments," *Smart Materials and Structures*, vol. 6, pp. 530-539, 1997.
- [9] H. Yu, L. Ai, M. Rouhanizadeh, D. Patel, E. S. Kim and T. K. Hsiai, "Flexible Polymer Sensors for In Vivo Intravascular Shear Stress Analysis," *Journal of Microelectromechanical Systems*, vol. 17, no. 5, pp. 1178-1186, 2008.
- [10] H. Fatemi, M. J. Modarres-Zadeh and R. Abdolvad, "Passive Wireless Temperature Sensing with Piezoelectric MEMS Resonators," *Proceedings of the IEEE*, vol. 92, no. 1, pp. 909-912, 2004.
- [11] M. J. Sinclair, "A High Force Low Area MEMS Thermal Actuator," in *The Seventh Intersociety Conference on Thermal and Thermomechanical Phenomena in Electronic Systems*, Las Vegas, NV, 2000.
- [12] J. W. Judy, "Microelectromechanical systems (MEMS): fabrication, design and applications," *Smart Materials and Structures*, vol. 10, pp. 1115-1134, 2001.
- [13] P. R. C. Gascoyne and X.-B. Wang, "Dielectrophoretic Separation of Cancer Cells from Blood," *IEEE Transaction on Industry Applications*, vol. 33, no. 3, pp. 670-678, 1997.
- [14] X.-B. Wang, Y. Huang, P. R. C. Gascoyne and F. F. Becker, "Dielectrophoretic Manipulation of Particles," *IEEE Transactions on Industry Applications*, vol. 33, no. 3, pp. 660-669, 1997.

- [15] A. Wasay and D. Sameoto, "Gecko gaskets for self-sealing and high-strength reversible bonding of microfluidics," *Lab on a Chip*, vol. 15, pp. 2749-2753, 2015.
- [16] A. Ramos, H. Morgan, N. G. Green and A. Castellanos, "AC Electric-Field-Induced Fluid Flow in Microelectrodes," *Journal of Colloid and Interface Science*, vol. 217, no. 2, pp. 420-422, 1999.
- [17] Y. Kato, Y. Hirai, K. Kamei, T. Tsuchiya and O. Tabata, "Microfluidic Device to Interconnect Multiple Organs via Fluidic Circulation: Towards Body-On-A-Chip," in *18th International Conference on Solid-State Sensors, Actuators and Microsystems*, Anchorage, 2015.
- [18] T. Matusos, A. Wisitsora-AT, T. Lomas, K. Jaruwongrungee, A. Sappat and A. Tuantranont, "Fabrication and characterization of Traveling wave dielectrophoretic (twDEP) microfluidic devices," in *2nd IEEE International Nanoelectronics Conference*, Shanghai, 2008.
- [19] G. K. Fedder, "MEMS Fabrication," in *IEEE International Test Conference*, 2003.
- [20] A. Cowen, B. Hardy, R. Mahadevan and S. Wilcenski, "PolyMUMPs Design Handbook, Rev. 13.0," MEMSCAP, 2011.
- [21] D. Sameoto, T. Hubbard and M. Kujath, "Operation of electrothermal and electrostatic MUMPs microactuators underwater," *Journal of Micromechanics and Microengineering*, vol. 14, no. 10, pp. 1359-1366, 2004.

- [22] B. Barazani, S. Warnat and T. Hubbard, "Simulation and Optical Measurement of MEMS Thermal Actuator Sub-micron Displacements in Air and Water," in *IEEE Canadian Conference on Electrical and Computer Engineering*, Halifax, 2015.
- [23] C.-Y. Yao and W.-L. Fu, "Biosensors for hepatitis B virus detection," *World Journal of Gastroenterology*, vol. 20, no. 35, pp. 12485-12492, 2014.
- [24] Q. Xue, C. Bian, J. Tong, J. Sun, H. Zhang and S. Xia, "A micro potentiometric immunosensor for hemoglobin-A1c level detection based on mixed SAMs wrapped nano-spheres array," *Biosensors and Bioelectronics*, vol. 26, no. 5, pp. 2689-2693, 2011.
- [25] A. Moglia, A. Menciassi, M. O. Schurr and P. Dario, "Wireless capsule endoscopy: from diagnostic devices to multipurpose robotic systems," *Biomed Microdevices*, vol. 9, no. 2, pp. 235-243, 2007.
- [26] D. S. Ferreira, T. S. Monteiro and G. Minas, "Spectroscopy microsystem for the detection of early cancer," in *2012 IEEE 2nd Portuguese Meeting in Bioengineering*, Coimbra, 2012.
- [27] P. Cong, N. Chaimanonart, W. H. Ko and D. J. Young, "A Wireless and Batteryless 10-Bit Implantable Blood Pressure Sensing Microsystem With Adaptive RF Powering for Real-Time Laboratory Mice Monitoring," *IEEE Journal of Solid-State Circuits*, vol. 44, no. 12, pp. 3631-3644, 2009.

- [28] H.-K. A. Tsai, E. A. Moschou, S. Daunert, M. Madou and L. Kulinsky, "Integrating Biosensors and Drug Delivery: A Step Closer Toward Scalable Responsive Drug-Delivery Systems," *Advanced Materials*, vol. 21, no. 6, pp. 656-660, 2009.
- [29] K. C. Cheung and P. Renaug, "BioMEMS for medicine: On-chip cell characterization and implantable microelectrodes," *Solid-State Electronics*, vol. 50, no. 4, pp. 551-557, 2006.
- [30] K. Menon, R. A. Joy, N. Sood and R. K. Mittal, "The Applications of BioMEMS in Diagnosis, Cell Biology, and Therapy: A Review," *BioNanoScience*, vol. 3, no. 4, pp. 356-366, 2013.
- [31] S. Zhang, Q. Tan, F. Li and X. Zhang, "Hybridization biosensor using diaquabis[N-(2-pyridinylmethyl)benzamide-k2N,O]-cadmium(II) diinirate as a new electroactive indicator for detection of human hepatitis B virus DNA," *Sensors and Actuators B: Chemical*, vol. 124, no. 2, pp. 290-296, 2007.
- [32] S. Warnat, H. King, C. Forbrigger and T. Hubbard, "PolyMUMPs MEMS device to measure mechanical stiffness of single cells in aqueous media," *Journal of Micromechanics and Microengineering*, vol. 25, p. 16, 2015.
- [33] S. Warnat, H. King, R. Schwartz, M. Kujath and T. Hubbard, "Submicron displacement measurements of MEMS using optical microphotographs in aqueous media: Enhancement using color image processing," in *2013 Materials Research*

*Society Fall Meeting, Boston, 2013.*

- [34] H. King, S. Warnat and T. Hubbard, "Effect of image degradation on nm-scale MEMS FFT optical displacement measurements," in *Canadian Conference on Electrical and Computer Engineering*, Halifax, 2015.
- [35] C. Yamahata, E. Sarajlic, G. J. M. Krijnen and M. A. M. Gijs, "Subnanometer Translation of Microelectromechanical Systems Measured by Discrete Fourier Analysis of CCD Images," *Journal of Microelectromechanical Systems*, vol. 19, no. 5, pp. 1273-1275, 2010.
- [36] P. R. C. Gascoyne and J. Vykoukal, "Particle separation by dielectrophoresis," *Electrophoresis*, vol. 23, no. 13, pp. 1973-1983, 2002.
- [37] S. Fiedler, S. G. Shirley, T. Schnelle and G. Fuhr, "Dielectrophoretic Sorting of Particles and Cells in a Microsystem," *Analytical Chemistry*, vol. 70, no. 9, pp. 1909-1915, 1998.
- [38] M. Bligh, K. G. Stanley, T. Hubbard and M. Kujath, "Sorting microparticles into lateral streams using a two-phase rectangular electrokinetic array," *Journal of Micromechanics and Microengineering*, vol. 18, 2008.
- [39] Y. Huang, R. Hölzel, R. Pethig and X.-B. Wang, "Differences in the AC electrodynamics of viable and non-viable yeast cells determined through combined dielectrophoresis and electrorotation studies," *Physics in Medicine and Biology*, vol.

37, no. 7, pp. 1499-1517, 1992.

- [40] H. Morgan, N. G. Green, M. P. Hughes, W. Monaghan and T. Tan, "Large-area travelling-wave dielectrophoresis particle separator," *Journal of Micromechanics and Microengineering*, vol. 7, no. 2, pp. 65-70, 1997.
- [41] M. P. Hughes and H. Morgan, "Dielectrophoretic trapping of single sub-micrometre scale bioparticles," *Journal of Physics D: Applied Physics*, vol. 31, pp. 2205-2210, 1998.
- [42] M. P. Hughes, H. Morgan and M. F. Flynn, "The Dielectrophoretic Behavior of Submicron Latex Spheres: Influence of Surface Conductance," *Journal of Colloid and Interface Science*, vol. 220, no. 2, pp. 454-457, 1999.
- [43] M. Bligh, *Micro-particle sorting using two-phase interdigitated electrokinetic arrays*, Halifax, Nova Scotia, 2008.
- [44] N. G. Green, A. Ramos and H. Morgan, "Numerical solution of the dielectrophoretic and travelling wave forces for interdigitated electrode arrays using the finite element method," *Journal of Electrostatics*, vol. 56, no. 2, pp. 235-254, 2002.
- [45] M. A. Schmidt, "Wafer-to-Wafer Bonding for Microstructure Formation," *Proceedings of the IEEE*, vol. 86, no. 8, pp. 1575-1585, 1998.
- [46] A. Hanneborg, "Silicon Wafer Bonding Techniques for Assembly of Micromechanical Elements," in *IEEE Micro Electro Mechanical Systems*, Nara, 1991.

- [47] K. Petersen, P. Barth and J. Poydock, "Silicon Fusion Bonding for Pressure Sensors," in *IEEE Solid-State Sensor and Actuator Workshop*, Hilton Head Island, 1988.
- [48] J. Kim, B. Jeong, M. Chiao and L. Lin, "Ultrasonic Bonding for MEMS Sealing and Packaging," *IEEE Transactions on Advanced Packaging*, vol. 32, no. 2, pp. 461-467, 2009.
- [49] Y. Temiz, R. D. Lovchik, G. V. Kaigala and E. Delamarche, "Lab-on-a-chip devices: How to close and plug the lab?," *Microelectronic Engineering*, vol. 132, pp. 156-175, 2015.
- [50] R. Ghodssi and P. Lin, *MEMS Materials and Processes Handbook*, New York: Springer, 2011.
- [51] S. Suresh, "Biomechanics and biophysics of cancer cells," *Acta Biomaterialia*, vol. 3, pp. 413-438, 2007.
- [52] A. Desai, S.-W. Lee and Y.-C. Tai, "A MEMS Electrostatic Particle Transportation System," *Sensors and Actuators A: Physical*, p. 33, 1999.
- [53] K. Tsukada, E. Sekizuka, C. Oshio and H. Minamitani, "Direct Measurement of Erythrocyte Deformability in Diabetes Mellitus with a Transparent Microchannel Capillary Model and High-Speed Video Camera System," *Microvascular Research*, vol. 61, pp. 231-239, 2001.
- [54] D. Liu and S. V. Garimella, "Microfluidic Pumping Based on Travelling-Wave

Dielectrophoresis," *Nanoscale and Microscale Thermophysical Engineering*, vol. 13, no. 2, pp. 109-133, 2009.

[55] J. Carter, A. Cowen, B. Hardy, R. Mahadevan, M. Stonefield and S. Wilcenski, *PolyMUMPs Design Handbook*, MEMSCAP Inc., 2005.

[56] A. C. Richards Grayson, R. S. Shawgo, A. M. Johnson, N. T. Flynn, Y. Li, M. J. Cima and R. Langer, "A BioMEMS Review: MEMS Technology for Physiologically Integrated Devices," *Proceedings of the IEEE*, vol. 92, no. 1, pp. 6-21, 2004.

[57] F. Koohyar, A. A. Rostami, M. J. Chaichi and F. Kiani, "Study on Thermodynamic properties for Binary Systems of Water + L-Cysteine Hydrochloride Monohydrate, Glycerol, and D-Sorbitol at Various Temperatures," *Journal of Chemistry*, vol. 2013, 2013.

# APPENDIX

## 1. MATLAB SIMULATION

```
clc;
clear;
close all;
path = uigetdir;
cd(path);
NN = 1000;
NNtwDEP = 10;
V = 10; %peak to peak voltage in volts
resolution = 0.1;
x = 0:resolution:12;
y = 0:resolution:12;
z = 0:resolution:2;
xy_matrix_r = zeros(size(y,2),size(x,2));
xy_matrix_i = zeros(size(y,2),size(x,2));
xy_matrix_rtemp = zeros(size(y,2),size(x,2));
xy_matrix_itype = zeros(size(y,2),size(x,2));
f_xr = zeros(1,size(x,2));
f_xi = zeros(1,size(x,2));
x_cur = 0;
for i = 1:1:size(x,2);
    if x_cur <=1;
        f_xr(i) = V;
        f_xi(i) = 0;
    elseif x_cur <=3;
        f_xr(i) = 0;
        f_xi(i) = 0;
    elseif x_cur <=5;
        f_xr(i) = -0.5*V;
        f_xi(i) = sqrt(3)*V/2;
    elseif x_cur <= 11;
        f_xr(i) = 0;
        f_xi(i) = 0;
    else
        f_xr(i) = V;
        f_xi(i) = 0;
    end
    x_cur = resolution*i;
end
C_nr = 0;
C_ni = 0;
for iteration = 1:1:NN;
    xy_matrix_rtemp = zeros(size(y,2),size(x,2));
    xy_matrix_itype = zeros(size(y,2),size(x,2));
    lambda = iteration*pi/12;
    real_int = f_xr.*cos(lambda*x);
    imag_int = f_xi.*cos(lambda*x);
    C_nr = (1/6)*trapz(x,real_int);
    C_ni = (1/6)*trapz(x,imag_int);
end
```

```

    for i = 1:1:size(y,2)
        for j=1:1:size(x,2)
            ip = i*resolution;
            jp = j*resolution;
            xy_matrix_rtemp(i,j) = C_nr*exp(-lambda*ip)*cos(lambda*jp);
            xy_matrix_itype(i,j) = C_ni*exp(-lambda*ip)*cos(lambda*jp);
        end
    end
    xy_matrix_r = xy_matrix_r + xy_matrix_rtemp;
    xy_matrix_i = xy_matrix_i + xy_matrix_itype;
end

figure1 = figure;
axes5 = axes('Parent',figure1,'Layer','top');
cl = -9:0.5:9;
contourf(x,y,xy_matrix_r,cl,'Parent',axes5);
colorbar('peer',axes5);
title('\phi_{R}(x,y)');
xlabel('x-distance (μm)');
ylabel('y-distance (μm)');

figure2 = figure;
axes6 = axes('Parent',figure2,'Layer','top');
contourf(x,y,xy_matrix_i,cl,'Parent',axes6);
colorbar('peer',axes6);
title('\phi_{I}(x,y)');
xlabel('x-distance (μm)');
ylabel('y-distance (μm)');

%calculating the gradient now
[gradRex, gradRey] = gradient(xy_matrix_r,resolution);
[gradImx, gradImy] = gradient(xy_matrix_i,resolution);

%calculating magnitude of gradients
gradReMag = sqrt((gradRex.*gradRex)+(gradRey.*gradRey));
gradImMag = sqrt((gradImx.*gradImx)+(gradImy.*gradImy));

gradReMag = gradReMag.^2;
gradImMag = gradImMag.^2;

Fdep = gradReMag + gradImMag;
[Fdep_x, Fdep_y] = gradient(Fdep,resolution);

figure;
quiver(x,y,Fdep_x,Fdep_y);
title('F_{DEP}');
xlabel('x-position (μm)');
ylabel('y-position (μm)');

% %trial section for FtwDEP
% gradRez = zeros(size(gradRex));
% gradImz = zeros(size(gradImx));
% gradT = zeros(size(gradRex,1),size(gradRex,2),3);
% gradT(:, :, 1) = gradRex;
% gradT(:, :, 2) = gradRey;

```

```

% gradT(:, :, 3) = gradRez;
% gradT2 = zeros(size(gradImx,1), size(gradImx,2), 3);
% gradT2(:, :, 1) = gradImx;
% gradT2(:, :, 2) = gradImy;
% gradT2(:, :, 3) = gradImz;
% cross_grads = cross(gradT, gradT2);
% [curl_cross_gradx, curl_cross_grady, curl_cross_gradz, cav2] =
curl(zeros(size(cross_grads)), zeros(size(cross_grads)), cross_grads);
% Ftwdep_x = curl_cross_gradx(:, :, 3);
% Ftwdep_y = curl_cross_grady(:, :, 3);
% figure;
% % cross_prod = gradRex.*gradImy - gradImx.*gradRey;
% % [Ftwdep_x, Ftwdep_y] = gradient(cross_prod, resolution);
%
quiver(x(1:10:end), y(1:10:end), Ftwdep_x(1:10:end, 1:10:end), Ftwdep_y(1:10:
end, 1:10:end), 'AutoScaleFactor', 5);
% title('F_{twDEP}');
% xlabel('x-position ( $\mu\text{m}$ )');
% ylabel('y-position ( $\mu\text{m}$ )');

C_nr = 0;
C_ni = 0;
xy_twdep_x = zeros(size(y,2), size(x,2));
xy_twdep_y = zeros(size(y,2), size(x,2));
syms sx sy;
%initializing functions for analytical calculation of FtwDEP
func1(sx, sy) = 0*sx + 0*sy; %func1 corresponds to dPhiR/dx
func2(sx, sy) = 0*sx + 0*sy; %func2 corresponds to dPhiI/dx
func3(sx, sy) = 0*sx + 0*sy; %func3 corresponds to dPhiR/dy
func4(sx, sy) = 0*sx + 0*sy; %func4 corresponds to dPhiI/dy
func5(sx, sy) = 0*sx + 0*sy; %func5 corresponds to d^2PhiR/dx^2
func6(sx, sy) = 0*sx + 0*sy; %func6 corresponds to d^2PhiI/dx^2
func7(sx, sy) = 0*sx + 0*sy; %func7 corresponds to d^2PhiR/dy^2
func8(sx, sy) = 0*sx + 0*sy; %func8 corresponds to d^2PhiI/dy^2
func9(sx, sy) = 0*sx + 0*sy; %func9 corresponds to d^2PhiR/dxdy
func10(sx, sy) = 0*sx + 0*sy; %func10 corresponds to d^2PhiI/dxdy
display('Currently on iteration number...');
for iteration = 1:1:NNtwDEP;
    display('Percent complete:...');
    (double(iteration)/double(NNtwDEP))*100
    lambda = iteration*pi/12;
    real_int = f_xr.*cos(lambda*x);
    imag_int = f_xi.*cos(lambda*x);
    C_nr = (1/6)*trapz(x, real_int);
    C_ni = (1/6)*trapz(x, imag_int);
    func1 = func1 - lambda*C_nr*exp(-lambda*sy)*sin(lambda*sx);
    func2 = func2 - lambda*C_ni*exp(-lambda*sy)*sin(lambda*sx);
    func3 = func3 - lambda*C_nr*exp(-lambda*sy)*cos(lambda*sx);
    func4 = func4 - lambda*C_ni*exp(-lambda*sy)*cos(lambda*sx);
    func5 = func5 - lambda^2*C_nr*exp(-lambda*sy)*cos(lambda*sx);
    func6 = func6 - lambda^2*C_ni*exp(-lambda*sy)*cos(lambda*sx);
    func7 = func7 + lambda^2*C_nr*exp(-lambda*sy)*cos(lambda*sx);
    func8 = func8 + lambda^2*C_ni*exp(-lambda*sy)*cos(lambda*sx);
    func9 = func9 + lambda^2*C_nr*exp(-lambda*sy)*sin(lambda*sx);
    func10 = func10 + lambda^2*C_ni*exp(-lambda*sy)*sin(lambda*sx);
end
display('Finished iterations');

```

```

depfuncX = func9*func4 + func1*func8 - func10*func3 - func2*func7;
depfuncY = -(func5*func4 + func1*func10 - func6*func3 - func2*func9);
display('Finished combining functions');
iterations = 0;
display('Currently on iteration...');
for i=1:1:size(y,2);
    for j=1:1:size(x,2);
        xy_twdep_x(i,j) = double(depfuncX(y(i), x(j)));
        xy_twdep_y(i,j) = double(depfuncY(y(i), x(j)));
        iterations = iterations + 1;
        display('Percent complete:...');
        (double(iterations)/(double(size(y,2))*double(size(x,2))))*100
    end
end
figure;
xy_twdep_x2 = xy_twdep_x(:,2:end);
xy_twdep_y2 = xy_twdep_y(:,2:end);
quiver(x(2:end),y,xy_twdep_x2,xy_twdep_y2);
title('Analytical F_{twDEP}');
xlabel('x-position (μm)');
ylabel('y-position (μm)');

norm_matrix = zeros(size(xy_twdep_x2));
norm_matrix = sqrt(xy_twdep_x2.^2+xy_twdep_y2.^2);
xy_twdep_x_norm = xy_twdep_x2./norm_matrix;
xy_twdep_y_norm = xy_twdep_y2./norm_matrix;
figure;
quiver(x(2:end),y,xy_twdep_x_norm,xy_twdep_y_norm);
title('Normalized Analytical F_{twDEP}');
xlabel('x-position (μm)');
ylabel('y-position (μm)');

%calculating the Clausius-Mossotti factor for use in calculating total
%forces (non-normalized)

Ks = 1*10^-9;
R1 = 6*10^-6;

freq = logspace(0,7);

perm_eth = 24.3*8.854*10^-12*ones(size(freq));
cond_eth = 0.2*10^-3*ones(size(freq));
%equation describing permittivity of sorbitol vs weight fraction?
%y = -0.0049*x^2-0.1735*x+76.663 (R^2 = 0.9079 - MEH), where solution
is
%1.8088 percent Sorbitol
%therefore for 0.1M, perm = ~76.33
perm_sorb = 76.663*8.854*10^-12*ones(size(freq)); %permittivity of 0.1M
sorbitol solution
cond_sorb = 3.0; %conductivity of 0.1M sorbitol solution
perm_latex = 2.6*8.854*10^-12*ones(size(freq));
cond_latex1 = (2*Ks/R1)*ones(size(freq)); %surface conductivity of 6μm
latex sphere

cperm_latex1 = complex(perm_latex, -cond_latex1./freq);
cperm_eth = complex(perm_eth, -cond_eth./freq);

```

```

cperm_sorb = complex(perm_sorb, -cond_sorb./freq); %complex
permittivity
%of 0.1M sorbitol
CM1 = ((cperm_latex1 - cperm_eth)./(cperm_latex1 + 2*cperm_eth));
CM_sorb = ((cperm_latex1 - cperm_sorb)./(cperm_latex1 + 2*cperm_sorb));

%calculating the value of Clausius-Mossotti factor at ~1MHz (maximum
%absolute value of CM factor for these particles)
F_6 = min(imag(CM_sorb));
%calculating volume in m^3 of the 6µm and 15µm spheres
vol_6 = (4/3)*(pi*(6*10^-6)^3);
%calculating force on particles (non-normalized) for given applied peak
to
%peak voltage (V)
Force_6micron = -0.5*vol_6*F_6*(V^2/((6*10^-
6)^3))*mean(mean(xy_twdep_x)); %force on particle based on Green et al.
display('The force on a 6µm particle is: (N)....');
display(double(Force_6micron));
%from here the velocity of the particle is calculated by using the
equation
%of force vs velocity for a spherical particle experiencing drag:
%Fd = 6*pi*R*n*U where R is particle radius, n is viscosity and U is
%velocity, therefore, U = F/(6*pi*R*n)
%in the case for 0.1M sorbitol the viscosity is 0.011 Pa-s
Velocity_6micron = Force_6micron/(6*pi*6*10^-6*(0.011));
display('The velocity of a 6µm particle is: (µm/s?)....');
display(double(Velocity_6micron*10^6));

```